Modelling crack nucleation in composite materials: a semi-analytical two-scale approach

Felger, Julian

(2020)

Modelling crack nucleation in composite materials: a semi-analytical two-scale approach

Vom Fachbereich Maschinenbau
der Technischen Universität Darmstadt
zur Erlangung des akademischen Grades
eines Doktor-Ingenieurs (Dr.-Ing.) eingereichte

Dissertation

von

Julian Felger, M.Sc.

aus Wiesbaden

Referent:	Prof. Dr.-Ing. Wilfried Becker
Korreferent:	Prof. Dr.-Ing. Michael Vormwald
Korreferent:	Prof. Dr. Dominique Leguillon

Darmstadt 2020
D17

Julian Felger
Modelling crack nucleation in composite materials: a semi-analytical two-scale approach

Darmstadt, Technische Universität Darmstadt
Published online on TUprints in 2020
Date of oral exam: May 19, 2020

Please cite this thesis as:
URN: urn:nbn:de:tuda-tuprints-118983
URL: https://tuprints.ulb.tu-darmstadt.de/id/eprint/11898

Preface

This dissertation is the result of my work as a doctoral student at the Institute of Structural Mechanics at Technische Universität Darmstadt. At this point I would like to thank all those who have contributed to the success of this work.

I would like to thank Prof. Dr.-Ing. Wilfried Becker for the excellent supervision and support of my scientific work and the freedom he has given me. I would like to thank Prof. Dr. Dominique Leguillon for the pleasant cooperation and the stimulating discussions. I would like to thank Prof. Dr.-Ing. Michael Vormwald for his interest in my work and for the careful review of this thesis.

Thanks to all colleagues for creating a great working culture and for the good times outside working hours. I would also like to thank Carolin and my parents for supporting me throughout my academic career.

Kurzfassung

Vor dem Hintergrund eines steigenden Bewusstseins für Ressourcen- und Energieeffizienz finden Leichtbaustrukturen aus Verbundwerkstoffen sowie Klebverbindungen zunehmend Verwendung in der Ingenieurpraxis. An konstruktiv bedingten Kerben oder Materialübergängen bilden sich jedoch starke Spannungskonzentrationen, welche den Ausgangspunkt für eine potenzielle Rissbildung darstellen. Weiterhin führt die Heterogenität solcher Verbundstrukturen zu komplexen Bruchphänomenen über verschiedene Längenskalen hinweg. Um einen optimalen Strukturentwurf hinsichtlich Festigkeit zu generieren und eine zuverlässige Konstruktion zu gewährleisten, sind effiziente und gleichzeitig präzise Methoden zur Beurteilung der Strukturintegrität von entscheidender Bedeutung.

Ziel dieser Arbeit ist es, ein effizientes semi-analytisches Verfahren zur Vorhersage von Rissentstehung an scharfen Kerben, Materialübergängen und Löchern in ebenen Laminaten bereitzustellen. Dies wird einerseits durch die Verwendung der Methode komplexer Potentiale erreicht, welche eine präzise Erfassung von Spannungskonzentrationen ermöglicht und die Grundlage für eine effiziente Berechnung verallgemeinerter Spannungsintensitätsfaktoren bildetet. Andererseits wird das Entstehen von kleinen Rissen mittels eines störungstheoretischen Ansatzes modelliert. Dies führt auf ein singulär gestörtes Problem, welches mit der Methode der Matched Asymptotic Expansions (MAE) behandelt wird. Aus numerischer Sicht folgt hieraus eine Entkopplung der makroskopischen Struktur-Längenskala und der rissbeschreibenden Längenskala. Das asymptotische Vorgehen ermöglicht weiterhin das Aufstellen semi-analytischer Ausdrücke für die Energiedissipation durch Rissbildung. Die asymptotische Darstellung von Spannungs- und Energiegrößen bildet schließlich die Grundlage für eine effiziente Auswertung des gekoppelten Spannungs- und Energiekriteriums im Rahmen der finiten Bruchmechanik.

Dieses asymptotische Zweiskalen-Modell wird anschließend verwendet, um die effektive Festigkeit von drei Mixed-Mode-Kerbsituationen vorherzusagen: eine Bi-Material-Stoßfügung, eine T-förmige Struktur mit einspringender Ecke und eine Bi-Material-Schäftung. Die Genauigkeit der asymptotischen Reihendarstellungen der Spannungen sowie der inkrementellen Energiefreisetzungsrate wird auf Basis numerischer Referenzdaten detailliert untersucht. Im Falle der Stoßfügung kann ein einfaches Skalierungsgesetz abgeleitet werden, welches die Festigkeit der Verbindung in Bezug auf die Klebschichtdicke charakterisiert. Darüber hinaus wird der Einfluss des elastischen Kontrastes zwischen Klebstoff und Fügeteil auf die Versagenslast der Fügung diskutiert. Im Falle der T-Struktur und der Schäftung werden zusätzlich Terme höherer Ordnung in den asymptotischen Entwicklungen berücksichtigt. Weiterhin müssen verschiedene konkurrierende Rissmuster in der Analyse betrachtet werden. Die Versagensvorhersagen auf Basis des asymptotischen Ansatzes werden mittels eines Kohäsivzonenmodells

und experimenteller Daten aus der Literatur validiert. Anschließend wird das asymptotische Verfahren geeignet erweitert, um die Untersuchung von Rissentstehung in gelochten Laminaten endlicher Breite zu ermöglichen. Basierend auf der Methode komplexer Potentiale und einem Korrekturfaktor bezüglich der finiten Breite wird eine präzise analytische Darstellung des Kerbnahfeldes am Lochrand erhalten. Um die inkrementelle Energiefreisetzungsrate adäquat zu erfassen werden in den asymptotischen Reihendarstellungen Terme höherer Ordnung verwendet. Die Potenzreihe wird anschließend in eine Padé-Reihe überführt, wodurch die Approximationsgüte erheblich verbessert werden kann. Die Genauigkeit des asymptotischen Ansatzes wird hinsichtlich des Einflusses der Lochgröße und -geometrie, der endlichen Breite des Laminates sowie bezüglich des Laminataufbaus untersucht. Abschließend werden Versagenslastvorhersagen mit experimentellen Ergebnissen aus der Literatur verglichen und validiert.

Abstract

Lightweight design concepts employing composite materials and adhesively bonded joints are increasingly used in modern engineering structures. However, the presence of material or geometrical discontinuities leads to stress concentrations triggering the nucleation of cracks. Furthermore, the heterogeneous nature of such composite structures is associated with complex fracture phenomena across different length scales. For engineers to provide an optimal structural design, efficient and reliable methods in order to assess the structural integrity are of crucial importance.

The objective of this work is to provide an efficient semi-analytical approach for predicting crack onset at sharp notches, bi-material junctions and openings in fibre-reinforced laminates. On the one hand, this is achieved employing a complex potential approach, that accurately captures stress concentrations (singularities) and enables a precise calculation of generalised stress intensity factors. On the other hand, the method of matched asymptotic expansions (MAE) is applied interpreting a newly nucleated crack as a small perturbation parameter within a singular perturbation problem. From a numerical point of view, this yields a decoupling of scales and semi-analytical expressions for the energy release due to crack nucleation. The asymptotic representations of stress and energy quantities serve as a basis for an efficient evaluation of the coupled stress and energy criterion forming a necessary and sufficient condition for fracture.

This two-scale methodology is employed to predict the effective strength of three mixed-mode specimens: a bi-material butt joint under uniaxial loading, a T-shaped structure under uniaxial loading and a bi-material scarf joint under four-point bending loading. The accuracy of the asymptotic expansions of stresses and incremental energy release rate is thoroughly investigated using numerical reference data. In case of the butt joint configuration, a simple scaling law is derived characterizing the joint strength in terms of the adhesive thickness. Moreover, the effect of the elastic mismatch between adhesive and adherend on the failure load is discussed. In case of the T-structure and the scarf-joint specimen, higher-order terms in the asymptotic expansions are used and different competing crack patterns must be considered. Predictions relying on the asymptotic approach are validated against cohesive zone data as well as experimental findings from literature. The asymptotic approach is then transferred to the situation of open-hole composite plates of finite width. Based on the method of complex potentials and a finite-width correction factor, a precise description of the notch-stress field is obtained. In order to accurately render the incremental energy release rate, higher-order terms within the series expansions are employed and the idea of Padé approximation is applied. The effect of the hole size and geometry, the plate's finite width as well as of the material's anisotropy on the accuracy of the asymptotic approach is examined. Finally, failure load predictions are compared against experimental results from literature.

Contents

Nomenclature

Abbreviations

BVP	Boundary Value Problem
CC	Coupled Criterion
CIM	Contour Integral Method
CZM	Cohesive Zone Model
GSIFs	Generalised Stress Intensity Factors
ERR	Energy Release Rate
FE	Finite Element
FEA	Finite Element Analysis, Finite Element Analyses
FFM	Finite Fracture Mechanics
IERR	Incremental Energy Release Rate
LEFM	Linear Elastic Fracture Mechanics
LM	Line Method
MAE	Method of Matched Asymptotic Expansions
MAPE	Mean Absolute Percentage Error
PM	Point Method
SBFEM	Scaled Boundary Finite Element Method
TCD	Theory of Critical Distances

Notation

$(\cdot)_{\mathrm{c}}$	critical value
$(\cdot)_{\mathrm{f}}$	value at failure
$(\cdot)^{\mathrm{I}}, (\cdot)^{\mathrm{II}}, (\cdot)^{\mathrm{III}}$	crack opening modes
$(\cdot)_{ij}$	index notation $i, j = 1, \ldots, 3$
$(\cdot)_{ijkl}$	index notation $i, j, k, l = 1, \ldots, 3$
$\hat{(\cdot)}$	dimensionless quantity
$(\cdot)'$	derivative with respect to complex variable
$\dot{(\cdot)}$	material derivative
$(\cdot)^T$	transpose
$[\![(\cdot)]\!]$	jump of a quantity
∇	nabla operator
∇_y	nabla operator with respect to inner variables
$\underline{(\cdot)} \cdot (\cdot), (\cdot) : (\cdot)$	scalar product
$\overline{(\cdot)}$	complex conjugate
$o(\cdot), \mathcal{O}(\cdot)$	Landau symbols
$(\cdot) \sim (\cdot)$	asymptotically equal to (in some given limit)

Latin symbols

a	semi-major axis of an ellipse
a, A	crack length/area

$\Delta a, \Delta A$	finite crack length/area
a_{ij}	laminate extensional stiffness
A_{ij}, B_{ij}	complex coefficients
b	semi-minor axis of an ellipse
$\underline{b}$	vector of body forces
$\mathbb{C}, \quad C_{ijkl}$	fourth-order stiffness tensor, components
C_{ij}	components of the two-subscript material stiffness tensor
d	out-of plane thickness
$\mathbf{D}$	coefficient matrix
$\underline{e}_i$	unit basis vector
E_{ij}	components of the Green–Lagrange strain tensor
$E, \quad E_i$	Young's modulus
F	free energy
F	load
f	specific free energy
g	arbitrary function
G	shear modulus
$\mathcal{G}$	differential energy release rate
$\bar{\mathcal{G}}$	incremental energy release rate
$\mathcal{G}_\mathrm{c}$	fracture toughness
h	thickness of a laminate
h_i	x_3 coordinate of individual ply within a laminate
H_i	special generalised stress intensity factors
i	imaginary unit
K	kinetic energy
K_i	generalised stress intensity factors
K_c	fracture toughness
l	length
N_{ij}	force resultants per length
$\underline{n}$	normal vector
P	power of external forces
p_i	complex parameters
Q_{ij}	reduced stiffness
q_i	complex parameters
R_{ij}	components of rotation matrix
R	radial dimension
r	radial coordinate
$\mathbb{S}, \quad S_{ijkl}$	fourth-order compliance tensor, components
t	adhesive thickness
$\underline{t}$	stress vector
$\underline{u}, \quad u_i$	displacement vector, displacement components
$\underline{u}^\mathrm{FE}$	finite element solution of displacement vector
$\underline{u}_i, \quad \underline{u}_{-i}$	primal and dual displacement eigenfunctions
U	strain energy density
$\underline{U}^0$	solution of unperturbed problem
$\underline{U}^{\Delta a}$	solution of perturbed problem

$\underline{U}^i$	higher-order correction terms in outer asymptotic expansion
$\underline{V}^i$	functions within inner asymptotic expansion
$\underline{\hat{V}}_i$	alternative functions within inner asymptotic expansion
$\mathrm{d}V$	infinitesimal volume element
w	width
x_i	spatial coordinates
$\underline{x}_{\mathrm{ct}}$	crack-tip coordinate
y_i	scaled spatial coordinates in inner domain
z, z_i	complex coordinate, generalised complex coordinate

Latin symbols

α	fibre orientation
γ_{ij}	engineering shear strains
γ	path, contour
Γ	surface
δ_{ij}	KRONECKER-symbol
$\Delta\Pi$	Difference or change in potential energy
θ	crack initiation angle
$\boldsymbol{\varepsilon}$, ε_{ij}	infinitesimal strain tensor, components
$\boldsymbol{\varepsilon}_y$	infinitesimal strain tensor with respect to the scaled inner domain
κ	auxiliary quantity
λ, λ_i	eigenvalue, singularity exponent
Λ	dimensionless parameter
μ_i	complex roots of characteristic equation
ν, ν_{ij}	Poisson's ratio
$\underline{\xi}$	location of crack onset
Π_{int}	elastic potential
Π_{ext}	external potential
ρ	density
ρ	scaled radial coordinate in inner domain
$\boldsymbol{\sigma}$, σ_{ij}	stress tensor, components
$\boldsymbol{\sigma}_i$, $\boldsymbol{\sigma}_{-i}$	primal and dual stress eigenfunctions
$\boldsymbol{\sigma}_y$	stress tensor with respect to the scaled inner domain
σ_{f}	failure stress
σ_∞	far-field stress
τ_{ij}	shear stresses
φ	circumferential coordinate
Φ	dissipation
Φ_i	complex potentials
χ	mixed-mode angle
χ_{reg}	viscous regularisation parameter
ψ	interface angle
$\Psi(\cdot,\cdot)$	Ψ-integral
Ω	domain
Ω^0	outer domain
Ω^∞	semi-infinite inner domain

$\Omega^{\Delta a}$	perturbed domain
$\partial\Omega$	boundary of domain
$\partial\Omega_\sigma$	portion of boundary with prescribed stresses
$\partial\Omega_u$	portion of boundary with prescribed displacements
$\partial\Omega_{\mathrm{N}}$	notch faces
$\partial\Omega_{\mathrm{C}}$	crack faces
$\partial\Omega_{\mathrm{I}}$	material interface

Chapter 1

Introduction

1.1 Motivation

In modern engineering practice, lightweight structures or components featuring favourable material properties such as high specific stiffness and strength are frequently used, in particular due to their superiority in terms of resource efficiency. This has been demonstrated for instance by Airbus launching the new generation of the family A350 XWB with fuselage and wing structures made primarily of composite material which leads to a significant reduction of fuel consumption (Marsh, 2010). Lightweight concepts typically employ a combination of materials with different mechanical properties, e.g. sandwich structures, fibre-reinforced plastics or adhesively bonded joints. The resulting material mismatch or cut-outs induce high stress concentrations ultimately limiting the structural integrity. Consequently, a detailed analysis of such stress raisers combined with a physically sound failure model is of crucial importance to ensure component safety.

Due to the heterogeneity of composite materials, fracture processes are complex in nature and are associated with different length scales ranging from a mesoscopic scale such as the fibre-diameter to the macroscopic dimensions of a laminate. This increases the demand for novel numerical and analytical methods in order to efficiently model and predict structural failure. In most cases, numerical methods are needed to compute the state of stress and strain at any given point of the mechanical system serving as a basis for a subsequent failure assessment. Employing the established finite element method (FEM) requires a very fine spatial discretisation (mesh) to accurately capture stress concentrations and their associated gradients. In the presence of cracks or sharp notches, stresses even turn out to be mathematically singular, which has a negative impact on the accuracy and convergence of the numerical solution. Assuming brittle fracture, newly formed cracks are typically small compared to a macroscopic characteristic length scale making a purely numerical approach ineffective. However, the FEM represents the most widespread numerical method in engineering practice and it seems to be expedient in terms of practical use to keep a new methodology as compatible as possible with the FEM.

This can be achieved on the one hand by combining FEM with the complex potential method and by embedding the process of crack formation in a matched asymptotic expansions (MAE) framework on the other hand. The complex potential method provides an analytical description of the stress and displacement distribution in the vicinity of a notch and serves as a basis to efficiently calculate the generalised stress

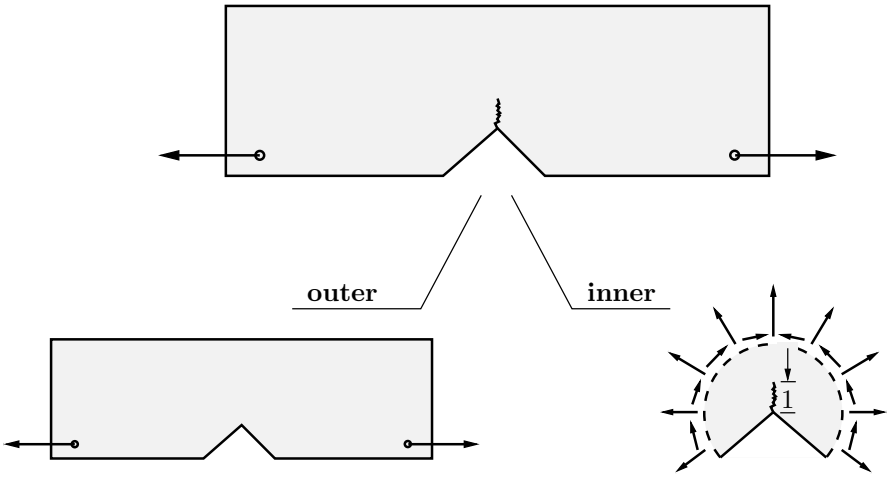

Figure 1.1: The perturbed problem is divided into a macroscopic (outer) problem and a mesoscopic (inner) problem, which can be solved numerically in a decoupled form.

intensity factors (GSIFs). Interpreting newly formed cracks as a small perturbation parameter within a singular perturbed problem allows for separating the mesoscopic scale defined by the crack itself from the global macroscopic scale. From a computational point of view, this means that macroscopic and mesoscopic scales do not have to be resolved simultaneously in one numerical model but instead can be treated independently employing different numerical models, see Fig. 1.1. It is important to note that the mesoscopic problem[1] does not depend on the specific global geometry and loading of the structure but is of universal character. Only on the local notch geometry enters the inner mesoscopic problem. Therefore, the inner problem can be solved once for all and applies to various structural situations. The connection between mesoscopic and macroscopic scales is established by adequately prescribing boundary conditions on the mesoscopic model according to the matching conditions within the MAE framework. Furthermore, the use of MAE leads to semi-analytical relations for the dissipated energy due to crack formation. Having an accurate representation of stresses and energy dissipation at hand, the coupled stress and energy criterion can be evaluated to obtain a failure prediction. This ultimately enables an efficient methodology to model crack nucleation processes and to assess the structural integrity while at the same retaining the finite element method as an established numerical tool.

1.2 Current state of research

Since stress concentrations trigger the initiation of cracks and hence failure, their analysis has been an important part of research during the last 80 years. Therefore, this section attempts to provide a short overview of the analysis of singular and non-singular stress raisers within the framework of linear elasticity with no claim to completeness. In the following a brief overview of existing failure criteria for brittle elastic materials and the use of MAE in fracture mechanics problems is given.

[1] also denoted as inner problem in the context of MAE

Analytical methods for the analysis of stress concentrations and singularities

Starting with non-singular stress raisers, Neuber (1934) in his pioneering work obtained closed-form analytical expressions for the two-dimensional stress field in the vicinity of a rounded notch under bending and shear loading. Based on this work, the formalism also referred to as three-function-approach has been developed and its capability to solve two-dimensional as well as three-dimensional notch problems is demonstrated in Neuber (1958). In case of two-dimensional problems, a very efficient method emerged formulating the field equations of linear elasticity in terms of the complex variable $z = x_1 + \mathrm{i}x_2$ and transferring the problem's domain in the complex plane. This approach is referred to as complex variable method or the method of complex potentials and has its origins in the work by Muskhelishvili (1963) and Kolosov (1909). Employing the complex variable approach enables problems to be solved that would be intractable by other solution strategies since many powerful mathematical techniques available from complex variable theory can be used. Savin (1961) employed the technique of conformal mapping to determine the stress distribution in the presence of circular, elliptical, triangular, and polygonal holes under uniaxial, biaxial and bending loading. Based on this work, conformal mapping has been used extensively in literature to determine the stress distribution at rounded or blunted notches under in-plane loading (Lazzarin et al., 2011, Lazzarin and Tovo, 1996, Filippi et al., 2002), V-notches with end holes (Zappalorto and Lazzarin, 2011) as well as hyperbolic and parabolic notches in round shafts under torsion (Zappalorto et al., 2008). Alternatively to conformal mapping, Leguillon (1999) used the method of matched asymptotic expansion to obtain the behaviour of stresses at a blunt crack which can be readily extended to blunt notches. In terms of anisotropic material behaviour, an extended version of the complex potential method can be derived. It is commonly distinguished between the so-called Lekhnitskii-formalism (Lekhnitskii, 1963) as a stress-based approach and the displacement-based Stroh-formalism (Stroh, 1958) relying on the work by Eshelby et al. (1953). Using either of these approaches, the stress distribution in an anisotropic infinite plate containing a circular or an elliptical hole can be obtained (Lekhnitskii, 1963, Ting, 1996). An extension to unsymmetric laminates possessing bending-extension coupling has been proposed by Becker (1993). The stress distribution at a rounded V-notches for quasi-orthotropic materials can be found in Kazberuk et al. (2016). A further extension to piezoelectric media using a Lekhnitskii-type approach has been proposed by Sosa (1991) studying stress concentrations at defects.

As already recognised by Neuber (1934), singular stresses arise in case of sharp corners where the local notch curvature tends to infinity. Typically, stress singularities occur due to geometric and material discontinuities such as re-entrant corners or multi-material junctions. During the last decades, a tremendous number of publications addressing singularities have been published. A collection of situations in which singularities arise within linear elasticity is provided by Sinclair (2004a) and a review of available methods for their analysis is given in Sinclair (2004b). Historically, the work by Williams (1952) is among the earliest contributions studying the singular behaviour of stresses at angular corners of plates in extension. Based on Airy stress function and using a separation of variables approach, Williams showed that the stress field can be expanded in form of a coordinate expansion with respect to the radial distance from the notch-tip. The

method is also referred to as eigenfunction expansion method and the corresponding infinite series is also denoted as Williams expansion. Moreover, Williams investigated the influence of different boundary conditions along the notch faces on the singularity exponent λ. As a continuation of his work, Williams (1959) examined singularities at a bi-material crack configuration and observed the occurrence of complex singularity exponents leading to oscillating fields close to the crack-tip. Using the method of complex potentials, Rice and Sih (1965) further investigated the case of a bi-material crack. The order of singularities at multi-wedge corners has been addressed by Theocaris (1974). The occurrence of logarithmic singularities has been observed by Dempsey and Sinclair (1981) in special bi-material wedge situations. A thorough investigation of stress singularities at multi-material junctions can be found in Sator (2010). The eigenfunction expansion method by Williams has been extended by Burton and Sinclair (1986) to study singularities at sharp V-notches in Reissner-Mindlin plates. A complex potential method allowing for an asymptotic description of the local notch stress field in Reissner-Mindlin plates has been derived by Felger and Becker (2017b) studying bi-material notch problems.

Calculation of generalised stress intensity factors (GSIFs)

The aforementioned publications focused on an analytical computation of stress singularities and eigenfunctions based on asymptotic considerations. However, to finally assess the structural integrity and perform a fracture mechanics analysis not only the eigenvalues and eigenfunctions but also the associated generalised stress intensity factors (GSIFs) are needed. Numerous methods exist in literature to calculate stress intensity factors. Having the stress and displacement eigenfunctions at hand, an intuitive approach is a collocation procedure matching the eigenfunctions to finite element results (Carpenter, 1984b, Sinclair and Mullan, 1982, Sih, 1973) and solve for the unknown intensity factors. However, this requires an accurate computation of higher eigensolutions, a very fine meshing close to the singularity and results depend to a large degree on what information was chosen within the collocation procedure.

Alternatively, special purpose hybrid finite elements were developed to account for notch-tip singularities. Employing the method of complex potentials, Tong et al. (1973) embedded an analytical solution into a finite element formulation to determine stress intensity factors of cracks. Based on this work, extensions to more complex bi-material notch problems have been proposed (Lin and Tong, 1980, Wang, 2017, Zhang et al., 2018). In practice, however, a special element formulation is required which is not readily available in commercial finite element software. Moreover, the element shape and dimension must be chosen adequately and one can expect that elongated notch elements will degrade the accuracy of the solution.

A very efficient approach in terms of compatibility and numerical effort is the use of contour integrals or conservative line integrals as originally proposed by Stern et al. (1976) to determine crack intensity factors for mixed-mode loading. The contour integral method (CIM) relies on Betti's reciprocal work theorem and requires the dual eigenfunctions associated with the specific notch situation. This approach has been proven to be extremely attractive since it involves the evaluation of a path

independent contour integral avoiding any special treatment of the region surrounding the notch tip. Furthermore, the computation of the integral is readily incorporated into existing commercial finite element programs. The contour integral method has been applied to two-dimensional homogeneous notch problems (Carpenter, 1984a) and bi-material configurations (Akisanya and Fleck, 1997, Banks-Sills and Sherer, 2002). An application in three-dimensional problems has been demonstrated by Leguillon (2014) and Luangarpa and Koguchi (2016) and an extension to electro-mechanical notch problems has been given by Hrstka et al. (2019). An overview of applications of the CIM can be found in Yosibash (2011).

As an alternative to conventional FE formulations, the scaled boundary finite element method (SBFEM) is particularly favourable for fracture mechanics problems. The SBFEM is a semi-analytical approach in which only the actual boundary of the body is spatially discretised with finite elements. Placing the scaling centre right at the notch tip, the behaviour of stresses and displacements in radial direction follows from an analytical solution without any a-priori assumptions. The SBFEM has been used to determine the intensity factors of cracks in homogeneous media (Song and Wolf, 2002) as well as in bi-material configurations (Müller et al., 2005). The SBFEM also allows for efficiently analysing stress singularities in three-dimensional problems such as the free-edge effect in composite laminates (Mittelstedt and Becker, 2005, 2006) or two meeting inter-fibre cracks in a composite laminate (Hell and Becker, 2015).

Assessment of brittle fracture in the presence of notches

Having precise solutions for stresses and displacement at hand, a reliable failure criterion is needed to ultimately assess the structural integrity. In terms of brittle materials, notches are of particular importance since they trigger crack formation and eventually cause catastrophic failure.

Employing linear elasticity theory, already Neuber (1934) observed that unphysically high (singular) stresses occur at the notch-tip in case of very small (vanishing) notch-root radii. Neuber concluded that stresses can no longer be evaluated in a point-wise manner right at the notch-tip but must be averaged over a certain distance L_{LM} instead. This approach is denoted as line method (LM) in modern literature. Alternatively, evaluating a stress criterion in a point-wise manner at a distance L_{PM} is denoted as point method (PM). The idea of LM has been adopted by Novozhilov (1969) and Seweryn (1994) for the assessment of sharp V-notches. Whitney and Nuismer (1974) employed the LM to predict the effective strength of fibre-reinforced plates weakened by a circular hole. In particular, the averaged stress criterion was capable to capture the hole size effect, that is, a decreasing effective strength of the plate with an increasing hole diameter. Tan (1994) compared strength predictions based on LM and PM for open-hole composite plates under uniaxial tensile loading. Since the process of failure is essentially a formation of cracks, it seems natural to use a fracture mechanics based approach instead of stress based criteria. In terms of notches where no initial crack is present, Waddoups et al. (1971) introduced an "imaginary" crack of length a_0 in order to apply the concept of LEFM. All the aforementioned approaches share a common feature, that is, the use of a critical length. Therefore, these criteria are summarised as

theory of critical distances (TCD) by Taylor (2007). In their simplest form, the length parameters $L_{\mathrm{LM}}, L_{\mathrm{PM}}$ and a_0 are given by:

$$L_{\mathrm{PM}} = \frac{1}{\pi}\left(\frac{K_{\mathrm{Ic}}}{\sigma_0}\right)^2, \quad L_{\mathrm{LM}} = \frac{2}{\pi}\left(\frac{K_{\mathrm{Ic}}}{\sigma_0}\right)^2, \quad a_0 = \frac{1}{\pi}\left(\frac{K_{\mathrm{Ic}}}{\hat{K}_1\sigma_0}\right)^2. \tag{1.1}$$

Here, K_{Ic} is the fracture toughness, $\hat{K}_1$ represents the dimensionless stress intensity factor corresponding to the imaginary crack and σ_0 is the inherent material strength which corresponds to the tensile strength σ_{c} in the case of plane specimens. Further applications of TCD to a variety of notch problems can be found in Taylor (2007). Although TCD approaches are very convenient in terms of implementation, the value of the required critical distance often depends on geometrical quantities of the structure, such as the hole diameter (Tan, 1994). Therefore, the critical length does not represent a material parameter and must be specifically adapted based on experimental studies.

In case of sharp notches, a GSIF-based criterion has been proposed relating the apparent GSIF of the leading-order term to a critical value (Dunn et al., 1997c, Reedy , 1993). Although GSIF-based criteria display good correlation to experimental data, their generalisation to mixed-mode problems is difficult and the critical value of the GSIF depends on geometric parameters such as the notch opening angle (Seweryn, 1994).

Based on the intuitive idea that failure initiation is correlated in some sense to the elastic strain energy density in the vicinity of the notch-tip, averaged strain energy density (SED) approaches emerged. The SED criterion states that failure occurs if the strain energy density averaged over a certain control volume exceeds a critical value. Applications of this criterion to rounded and sharp V-notches can be found in Lazzarin and Zambardi (2001), Lazzarin and Berto (2005), Ayatollahi et al. (2016), Yosibash (2011) and Gómez et al. (2009).

A model that essentially combines a strength based failure criterion and an energy based fracture criterion is the cohesive zone model (CZM), see Elices et al. (2002) for a review. According to CZM, the debonding process is localised in a narrow band, the cohesive zone and the failure behaviour is governed by a traction separation law describing the process from the initial undamaged state to the cracked state. Since the pioneering work by Barenblatt (1959), CZMs are widely established mainly for two reasons: first, although originally proposed for brittle fracture, they allow for a description of many fracture phenomena characterised by a strip-shaped process zone such as metals, fibre-reinforced materials, ceramics, concrete and fracture processes along material interfaces. Second, CZMs are very suitable in terms of a numerical treatment employing FEA. Applications of CZMs to notches and to bonded joint can be found in Gómez and Elices (2003a,b) and in Gustafson and Waas (2009), Martin et al. (2016), Campilho et al. (2012), Stein et al. (2015). However, numerical calculations employing CZM are expensive in terms of computational effort since a non-linear problem has to be solved. Furthermore, additional non-physical parameters (e.g. the viscous regularisation) are involved using CZM numerically which must be carefully accounted for, cf. Section 4.

Based on a variational approach to brittle fracture as proposed by Francfort and Marigo (1998), a regularised method emerged with the so-called phase-field models of fracture. In this approach cracks are modelled using a smeared representation of the crack topology and a new field variable, also referred to as damage variable, enters the underlying mathematical formulation of the problem. Crack evolution and propagation is based solely on energetic arguments and no a-priori assumptions on the potential crack path must be made (as it is the case for CZM). This enables to model complex phenomena such as the branching of one crack into multiple cracks (Hofacker and Miehe, 2012, Li et al., 2016), multi-physics problems such as hydraulic fracturing of fluid-saturated porous media (Miehe and Mauthe, 2016) or fatigue problems (Alessi et al., 2018). The problem of crack initiation at notches has been tackled very recently by Tanné et al. (2018) and Bleyer and Alessi (2018). Although phase-field models are very flexible in terms of their range of applicability, especially the phenomenon of crack nucleation still poses challenges and a stable numerical implementation is not straightforward.

In the present work, the concept of finite fracture mechanics (FFM) as originally proposed by Hashin (1996) is employed assuming an instantaneous formation of cracks of finite size. This introduces the finite crack length as a new unknown compared to classical linear elastic fracture mechanics (LEFM). In light of FFM, Leguillon (2002) proposed a coupled criterion (CC) requiring a stress and energy criterion to be fulfilled simultaneously. The coupled criterion has been applied successfully for strength predictions of various structural situations. Crack onset at sharp V-notches has been addressed by Leguillon (2002), Yosibash et al. (2006), Sapora et al. (2013), Carpinteri et al. (2008) and a very good agreement with experimental data is observed. In particular, the effect of the opening angle on the failure load is captured correctly. The case of rounded notches has been studied by Leguillon et al. (2003) and Carpinteri et al. (2011). Crack onset at open hole plates under uniaxial tensile loading has been investigated numerically by Weißgraeber et al. (2016a), Martin et al. (2012), Rosendahl et al. (2017) and a semi-analytical approach was proposed by Felger et al. (2017a,b). The coupled criterion renders the effect of hole size on the effective structural strength in agreement with experimental data, which is also referred to as hole-size effect. The failure of adhesively bonded joints has been examined by Carrère et al. (2015), Cornetti et al. (2012), Stein et al. (2015), Hell et al. (2014), Weißgraeber and Becker (2011), Weißgraeber et al. (2014) and Felger et al. (2019b). The experimentally observed adhesive thickness effect, that is, a decreasing effective joint strength for an increasing adhesive thickness has been captured correctly. The situation of bolted joints has been investigated by Catalanotti and Camanho (2013). The coupled criterion has also been employed to study the crack onset at free edges of laminates also denoted as the free-edge effect (Hebel et al., 2010, Martin et al., 2010, Dölling et al., 2018). Rosendahl et al. (2019d) extended the coupled criterion to hyperelastic material behaviour and crack nucleation in structural glazing silicone sealants under mixed-mode conditions has been predicted in a very good agreement with experimental data. An extension of the coupled criterion to three-dimensional problems is presented by Leguillon (2014) and Doitrand and Leguillon (2018). A review on applications of the CC can be found in Weißgraeber et al. (2016b).

Matched asymptotic expansions (MAE) applied to crack formation

If the length of an initiating crack, the advancement of an existing crack or the size of a cavity triggering crack formation can be considered as small compared to a characteristic global length scale, the method of matched asymptotic expansion can be applied advantageously. Addressing the computation of singularities in elasticity problems, Leguillon and Sanchez-Palencia (1987) investigated the effect of a slightly perturbed corner on the field variables close to the perturbation. This situation has been modelled as a singular perturbation problem and a MAE framework has been established employing inner and outer asymptotic solutions. Leguillon (1993) studied the formation of a small kink emanating from a pre-existing crack in a 2D anisotropic material. The small kink segment is used as perturbation parameter providing solutions for the final stress intensity factor of the crack. The phenomena of penetration or deflection of a crack impinging on an interface has been tackled by Leguillon et al. (2000b,a) considering the small extension of the primary crack as perturbation of the initial state. This allows for deriving an energetic criterion for crack deflection generalising the criterion of Ming-Yuan and Hutchinson (1989). Effects of residual stresses and higher-order terms are discussed in Leguillon et al. (2001). The onset of a crack emanating from a sharp V-notch has been studied by Leguillon (2002) using the length of an initiating crack as perturbation parameter. Furthermore, the coupled criterion (CC) as a criterion for crack onset has been proposed. Crack initiation at a rounded V-notch and the effect of the notch-tip radius on the failure load have been addressed by Leguillon and Yosibash (2003). Using asymptotics reveals how the energy dissipation due to crack onset scales with the notch-tip radius. Mixed-mode fracture at a V-notch has been studied by Yosibash et al. (2006) and García and Leguillon (2012) employing asymptotics. The close similarity between the coupled criterion and a Dugdale-type cohesive model can be found in Henninger et al. (2007) using asymptotics. Quesada et al. (2009) investigated multiple failures in or around a stiff inclusion embedded in a soft matrix under a compressive loading. Using the inclusion as small perturbation parameter, MAE shows that the IERR scales linearly with the inclusion diameter. Based on an intermediate asymptotic concept, Le et al. (2010) embedded a small bi-material crack in the singular stress field of a bi-material corner corresponding to the strongest stress singularity and obtained a leading-order asymptotic solution of the energy release rate (ERR). Leguillon (2014) extended the coupled criterion to the three-dimensional case employing MAE with the crack depth of a simplified crack geometry as perturbation parameter. The effect of a small V-notch playing the role of a surface flaw on the effective strength of ceramic and polystyrene specimens has been examined by Leguillon et al. (2018) and Cornetti et al. (2010), respectively. Using the notch depth as perturbation parameter shows that the ERR scales linearly with the notch size at the leading-order.

1.3 Objectives and outline of the thesis

The present work aims to provide an efficient methodology to study and assess mixed-mode crack initiation at sharp notches, bi-material joints and at open holes in composite

plates using a complex potential approach combined with the method of matched asymptotic expansions. To this end, the validity range and accuracy of an asymptotic description of crack onset phenomena in the framework of FFM must be critically investigated and quantified based on fully numerical reference solutions and experimental findings. Using adequate case studies, the geometrical and material parameters affecting the length scale of initiating cracks are to be identified. Furthermore, the impact and necessity of techniques potentially increasing the validity range of the asymptotic approximation are to be examined. Finally, this work aims contributing to understand the asymptotic methodology as a two-scale modelling approach that enables an efficient application of finite fracture mechanics even in complicated situations, e.g. the existence of multiple stress raisers and competing crack patterns, as typically faced in real world problems.

The theoretical basis of this work is established in Section 2 including a brief introduction into the theory of linear elasticity, associated energy principles and the method of complex potentials for isotropic and anisotropic materials. Subsequently, the relevant aspects of fracture mechanics are outlined and the computation of generalised stress intensity factors is described. Section 2 ends with a description of finite fracture mechanics and the coupled stress and energy criterion.

In Section 3, the general form of stresses and displacements at a bi-material notch is provided using the method of complex potentials. Subsequently, the employed MAE framework to derive an asymptotic expansion of the change in potential energy due to crack onset is introduced. At the outset, the leading-order term representation is derived and the process of matching inner and outer expansions is demonstrated systematically following the matching principle of Van Dyke (1964) and the work by Leguillon (1993). Subsequently, higher-order terms of the unperturbed solution are considered including the general situation of eigenfunctions with complex exponents λ_i. Corresponding higher-order terms in the inner expansion and of the incremental energy release rate (IERR) are given. In this context, a very valuable symmetry property concerning higher-order scaling coefficients is rigorously proven for which only numerical evidence existed in literature before. The effect and insights gained of considering additional higher-order interaction terms is discussed by means of a model problem.

Having the MAE framework at hand, Section 4 deals with its application to the three mixed-mode problems depicted on the left-hand side of Fig. 1.2. Here, the focus is on a thorough investigation of the asymptotics' range of validity. Starting with the butt joint configuration, the GSIF-computation and the numerical calculation of the inner asymptotic solution are exemplarily demonstrated. The validity and accuracy of the asymptotic expansions as well as of the corresponding failure load predictions are checked based on numerical reference solutions. Moreover, the effect of the adhesive thickness and the material mismatch on the accuracy of the asymptotic approach is discussed. The predicted joints strengths are compared against CZM results and experimental findings from literature. Whereas a leading-order terms analysis suffices in case of the butt joint, higher-order terms must be considered to accurately predict the failure behaviour of a T-shaped structure, cf. Fig. 1.2 on the left-hand side. In addition, a more general form of the optimization problem following from the coupled

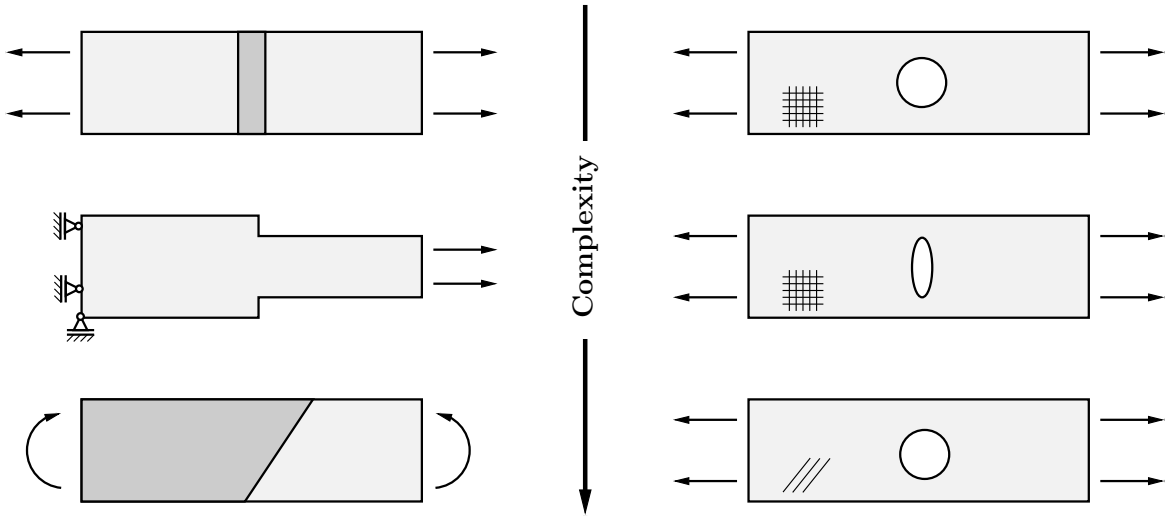

Figure 1.2: Overview of structural situations tackled in the present work.

criterion must be solved considering the angle of crack initiation as a new unknown parameter. Further increasing complexity, the scarf-joint specimen depicted in Fig. 1.2 is investigated at the end of Section 4. Here, multiple competing fracture scenarios must be distinguished and complex higher-order terms must be taken into account in order to accurately predict failure using asymptotics.

In Section 5, the idea of MAE is transferred for the first time to the situation of finite-width composite plates under uniaxial loading containing circular and elliptical holes as sketched on the right-hand side of Fig. 1.2. In order to accurately render the IERR, higher-order terms in the asymptotic expansion must be considered. Since the IERR appears as a MacLaurin series with respect to the crack length the asymptotic region of validity can be increased significantly employing the idea of Padé approximation. Based on numerical reference solution, it is shown that the concept of Padé approximation must be used to enable an accurate approximation of the IERR. Combining the method of complex potentials with the idea of finite-width correction factor and the Padé approximation for the IERR provides a very efficient methodology to study the effect of the plate's finite width, the hole geometry and the impact of material parameters on the structure's effective strength with a minimum of computational effort. The study shows that failure of open-hole plates can be accurately predicted and even the onset of inclined cracks can be rendered in close agreement with experimental data.

A brief summary regarding the most important findings of this work is provided in Section 6.

Chapter 2

Theoretical background

This section briefly introduces the theoretical frameworks and concepts used throughout this work. At the outset, the governing field equations and energy principles of linear elasticity theory are summarised and the method of complex potentials for solving two-dimensional boundary-value-problems is presented. Based on linear elastic fracture mechanics, the concept of finite fracture mechanics is introduced and the coupled stress and energy criterion is given in its general form. A standard notation is used denoting scalar quantities by italic letters, underlining is used to indicate vectors, bold symbols are employed for second-order tensors and fourth-order tensors are represented by blackboard symbols.

2.1 Linear elasticity theory

The theory of linear elasticity describes the mechanics of deformable solids and structures supposing linear-elastic material behaviour and small deformation. The basic equations and important energy principles are summarised the following. A more detailed discussion can be found in text books by e.g. Becker and Gross (2002), Sadd (2009), Gross and Seelig (2017) and Muskhelishvili (1963).

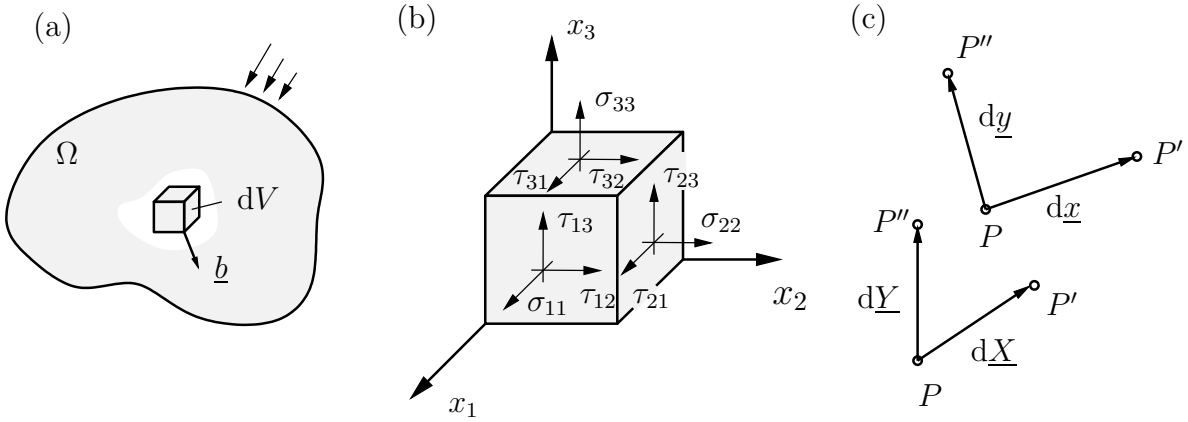

Figure 2.1: (a) An elastic body Ω and an infinitesimal volume element $\mathrm{d}V$. (b) Three-dimensional stress state. (c) Transformation of two material line elements.

2.1.1 State of stress and small displacements

Let us consider the body sketched in Fig. 2.1(a). As a result of external loading, internal forces acting between volume elements $\mathrm{d}V$ of the body Ω are present. Relating these internal forces to an infinitesimal surface element leads to the stress vector $\underline{t}$ that is defined at any material point of the body. The state of stress at a material point is defined by the Cauchy stress tensor $\boldsymbol{\sigma} = \sigma_{ij}\underline{e}_i \otimes \underline{e}_j$, that is a second-order tensor. It is convenient to write the components σ_{ij} with respect to a Cartesian coordinate system in form of a matrix:

$$[\sigma_{ij}] = \begin{bmatrix} \sigma_{11} & \sigma_{12} & \sigma_{13} \\ \sigma_{12} & \sigma_{22} & \sigma_{23} \\ \sigma_{13} & \sigma_{23} & \sigma_{33} \end{bmatrix} = \begin{bmatrix} \sigma_{11} & \tau_{12} & \tau_{13} \\ \tau_{12} & \sigma_{22} & \tau_{23} \\ \tau_{13} & \sigma_{23} & \sigma_{33} \end{bmatrix}. \tag{2.1}$$

The stress components are visualised in Fig. 2.1(b) and $\sigma_{11}, \sigma_{22}, \sigma_{33}$ are denoted as normal stresses whereas $\tau_{12}, \tau_{23}, \tau_{13}$ are referred to as shear stresses. Based on the theorem of angular momentum, the stress tensor is symmetric, that is, $\tau_{ij} = \tau_{ji}$. The stresses acting on a surface element depend not only on the position but also on the orientation of the element defined by its normal vector $\underline{n}$. This is expressed by the Cauchy theorem:

$$\underline{t} = \boldsymbol{\sigma} \cdot \underline{n}. \tag{2.2}$$

Let the components of the stress tensor σ_{ij} be given with respect to a Cartesian coordinate system defined by the basis vectors $\underline{e}_1, \underline{e}_2, \underline{e}_3$. A rotation of this coordinate system yields the rotated basis vectors $\tilde{\underline{e}}_1, \tilde{\underline{e}}_2, \tilde{\underline{e}}_3$ with

$$\tilde{\underline{e}}_i = (\tilde{\underline{e}}_i \cdot \underline{e}_j)\,\underline{e}_j = R_{ij}\underline{e}_j, \qquad R_{ij} = \cos(\tilde{\underline{e}}_i, \underline{e}_j). \tag{2.3}$$

The components $\tilde{\sigma}_{ij}$ with respect to the rotated system are then given by

$$\tilde{\sigma}_{ij} = R_{ik}\sigma_{kl}R_{jl}. \tag{2.4}$$

In case of an elastic body, the applied external loading leads not only to stresses within the continuum but also to a deformation. The transformation from the initially undeformed state to the deformed state is described by the displacement vector $\underline{u}$. In order to establish a quantitative measure of deformation, let us consider the points P, P' and P'', which are in an infinitesimal distance to each other and define the vectors $\mathrm{d}\underline{X}$ and $\mathrm{d}\underline{Y}$ before deformation takes place, cf. Fig. 2.1(c). After deformation, these vectors or line-elements are given by $\mathrm{d}\underline{x}$ and $\mathrm{d}\underline{y}$, respectively. One way of quantitatively characterising deformation is to consider the difference of the scalar product between these vectors before and after deformation:

$$\mathrm{d}x_i\mathrm{d}y_i - \mathrm{d}X_i\mathrm{d}Y_i = \left(\frac{\partial u_i}{\partial X_j} + \frac{\partial u_j}{\partial X_i} + \frac{\partial u_k}{\partial X_i}\frac{\partial u_k}{\partial X_j}\right)\mathrm{d}X_i\mathrm{d}Y_j = 2E_{ij}\mathrm{d}X_i\mathrm{d}Y_j. \tag{2.5}$$

This leads to the Green–Lagrange strain tensor $\boldsymbol{E}$ with components E_{ij} representing a local quantity defined at any material point and vanishing in case of a rigid body

motion. In many engineering applications and in particular within elasticity theory, the gradient of displacements is small compared to one, $|\partial u_i/\partial X_j| \ll 1$. Consequently, the quadratic terms in Eq. (2.5) can be neglected and $\mathrm{d}x_i = (\partial u_i/\partial X_j + \delta_{ij})\mathrm{d}X_j \approx \mathrm{d}X_i$ holds in a first-order approximation[2]. Based on Eq. (2.5) these simplifications lead to the linearised strain tensor $\boldsymbol{\varepsilon}$ which is used throughout this work as a measure for deformation. Its components ε_{ij} are given by

$$\varepsilon_{ij} = \frac{1}{2}\left(\frac{\partial u_i}{\partial x_j} + \frac{\partial u_j}{\partial x_i}\right). \tag{2.6}$$

The strain tensor $\boldsymbol{\varepsilon}$ is symmetric and its components are typically written as

$$[\varepsilon_{ij}] = \begin{bmatrix} \varepsilon_{11} & \varepsilon_{12} & \varepsilon_{13} \\ \varepsilon_{12} & \varepsilon_{22} & \varepsilon_{23} \\ \varepsilon_{13} & \varepsilon_{23} & \varepsilon_{33} \end{bmatrix} = \begin{bmatrix} \varepsilon_{11} & \frac{1}{2}\gamma_{12} & \frac{1}{2}\gamma_{13} \\ \frac{1}{2}\gamma_{12} & \varepsilon_{22} & \frac{1}{2}\gamma_{23} \\ \frac{1}{2}\gamma_{13} & \frac{1}{2}\gamma_{23} & \varepsilon_{33} \end{bmatrix}, \tag{2.7}$$

employing the engineering shear strain γ_{ij}. Under a change of basis, the components of the infinitesimal strain tensor transform in the same manner as the stress components in Eq. (2.4).

Having stresses and displacements at hand, the theorem of linear momentum applied to the volume element $\mathrm{d}V$ reads

$$\rho\,\mathrm{d}V\frac{\mathrm{D}\underline{u}}{\mathrm{D}t} = \rho\,\mathrm{d}V\underline{\dot{u}} = \nabla\cdot\boldsymbol{\sigma}\,\mathrm{d}V + \rho\underline{b}\,\mathrm{d}V, \tag{2.8}$$

or in terms of components with respect to a Cartesian coordinate system

$$\rho\,\mathrm{d}V\dot{u}_i = \sigma_{ij,j}\,\mathrm{d}V + \rho b_i\,\mathrm{d}V. \tag{2.9}$$

Here, ρ is the material's density and $\underline{b}$ is the vector of body force. If the body is at rest, the derivative with respect to time vanishes which leads to the so-called equilibrium equations:

$$\nabla\cdot\boldsymbol{\sigma} + \rho\underline{b} = 0. \tag{2.10}$$

From now on, body forces are not considered and set equal to zero ($\underline{b} = 0$).

2.1.2 Linear elastic material behaviour

Linear elastic material behaviour is characterised by a linear relationship between the stress tensor and the infinitesimal strain tensor represented by Hooke's law:

$$\boldsymbol{\sigma} = \mathbb{C} : \boldsymbol{\varepsilon}. \tag{2.11}$$

[2]The KRONECKER-symbol δ_{ij} is defined as: $\delta_{ij} = \begin{cases} 1 & i = j \\ 0 & i \neq j \end{cases}$.

The quantity $\mathbb{C}$ is the forth-order stiffness tensor. Inverting Eq. (2.11) yields

$$\boldsymbol{\varepsilon} = \mathbb{S} : \boldsymbol{\sigma} \tag{2.12}$$

with the compliance tensor $\mathbb{S}$. Based on energetic arguments and using Eq. (2.11) or Eq. (2.12), respectively, the following symmetry properties can be derived:

$$C_{ijkl} = C_{klij} = C_{jikl} = C_{jilk}, \qquad S_{ijkl} = S_{klij} = S_{jikl} = S_{jilk}. \tag{2.13}$$

Consequently, only 21 out of the total 81 components of the stiffness (compliance) tensor are independent of each other. This allows for writing Hooke's law in a very convenient form also referred to as Voigt notation:

$$\begin{pmatrix} \sigma_{11} \\ \sigma_{22} \\ \sigma_{33} \\ \tau_{23} \\ \tau_{13} \\ \tau_{12} \end{pmatrix} = \begin{pmatrix} C_{11} & C_{12} & C_{13} & C_{14} & C_{15} & C_{16} \\ C_{12} & C_{22} & C_{23} & C_{24} & C_{25} & C_{26} \\ C_{13} & C_{23} & C_{33} & C_{34} & C_{35} & C_{36} \\ C_{14} & C_{24} & C_{34} & C_{44} & C_{45} & C_{46} \\ C_{15} & C_{25} & C_{35} & C_{45} & C_{55} & C_{56} \\ C_{16} & C_{26} & C_{36} & C_{46} & C_{56} & C_{66} \end{pmatrix} \begin{pmatrix} \varepsilon_{11} \\ \varepsilon_{22} \\ \varepsilon_{33} \\ \gamma_{23} \\ \gamma_{13} \\ \gamma_{12} \end{pmatrix}. \tag{2.14}$$

The material stiffness coefficients are now denoted by means of the two-subscript components C_{ij}. In engineering practice, the employed materials typically possess some sort of symmetry, or more precisely material planes of symmetry. This leads to a further reduction of independent quantities C_{ij}. When three mutually orthogonal planes of symmetry exist, the material is denoted as orthotropic. Employing the inverse form of Hooke's law (2.12) and using the so-called engineering constants instead of the abstract compliance coefficients S_{ij}, it follows:

$$\begin{pmatrix} \varepsilon_{11} \\ \varepsilon_{22} \\ \varepsilon_{33} \\ \gamma_{23} \\ \gamma_{13} \\ \gamma_{12} \end{pmatrix} = \begin{pmatrix} 1/E_1 & -\nu_{21}/E_2 & -\nu_{31}/E_3 & 0 & 0 & 0 \\ -\nu_{12}/E_1 & 1/E_2 & -\nu_{32}/E_3 & 0 & 0 & 0 \\ -\nu_{13}/E_1 & -\nu_{23}/E_2 & 1/E_3 & 0 & 0 & 0 \\ 0 & 0 & 0 & 1/G_{23} & 0 & 0 \\ 0 & 0 & 0 & 0 & 1/G_{13} & 0 \\ 0 & 0 & 0 & 0 & 0 & 1/G_{12} \end{pmatrix} \begin{pmatrix} \sigma_{11} \\ \sigma_{22} \\ \sigma_{33} \\ \tau_{23} \\ \tau_{13} \\ \tau_{12} \end{pmatrix}. \tag{2.15}$$

Here, E_1, E_2 and E_3 are Young's moduli and ν_{ij} are Poisson's ratios[3]. Due to symmetry properties, there exist 9 independent engineering constants for orthotropic materials. In case of isotropic behaviour the two independent quantities E and ν remain.

State of plane stress

A state of plane stress is defined by:

$$\sigma_{11} = \sigma_{11}(x_1, x_2),\ \sigma_{22} = \sigma_{22}(x_1, x_2),\ \tau_{12} = \tau_{12}(x_1, x_2),\ \sigma_{33} = \tau_{13} = \tau_{23} = 0. \tag{2.16}$$

[3]Poisson's ratio is defined by the ratio of transverse strain in the jth direction to the axial strain in the ith direction, e.g. $\nu_{12} = -\varepsilon_{22}/\varepsilon_{11}$ when uniaxial stress σ_{11} is applied.

The plane stress assumption represents an adequate approximation for plates, which are only loaded by in-plane forces and for which the thickness in out-of-plane direction is small compared to any other characteristic structural length. Employing the plane stress approximation leads to a two-dimensional problem with respect to the in-plane coordinates. Using Voigt notation Hooke's law for isotropic materials reads

$$\begin{pmatrix}\sigma_{11}\\ \sigma_{22}\\ \tau_{12}\end{pmatrix} = \frac{E}{1-\nu^2}\begin{pmatrix}1 & \nu & 0\\ \nu & 1 & 0\\ 0 & 0 & \frac{1-\nu}{2}\end{pmatrix}\begin{pmatrix}\varepsilon_{11}\\ \varepsilon_{22}\\ \gamma_{12}\end{pmatrix}. \tag{2.17}$$

The material constant $G = E/(2(1+\nu))$ relating the shear stress and the engineering shear strain is denoted as shear modulus. In the case of fibre-reinforced composite materials, plates are typically made of unidirectional fibre-reinforced layers. Considering such a layer, the constitutive equations with respect to the $\tilde{x}_1$-$\tilde{x}_2$-$\tilde{x}_3$ material coordinate system read:

$$\begin{pmatrix}\tilde{\sigma}_{11}\\ \tilde{\sigma}_{22}\\ \tilde{\tau}_{12}\end{pmatrix} = \begin{pmatrix}Q_{11} & Q_{12} & 0\\ Q_{12} & Q_{22} & 0\\ 0 & 0 & Q_{66}\end{pmatrix}\begin{pmatrix}\tilde{\varepsilon}_{11}\\ \tilde{\varepsilon}_{22}\\ \tilde{\gamma}_{12}\end{pmatrix}. \tag{2.18}$$

The quantities Q_{ij} are the components of the so-called plane-stress reduced stiffness matrix and are given by:

$$\begin{aligned} Q_{11} &= \frac{E_1}{1-\nu_{12}\nu_{21}}, \quad Q_{12} = \frac{\nu_{12}E_2}{1-\nu_{12}\nu_{21}},\\ Q_{22} &= \frac{E_2}{1-\nu_{12}\nu_{21}}, \quad Q_{66} = G_{12}. \end{aligned} \tag{2.19}$$

In order to describe the material behaviour of the whole laminated plate, Eq. (2.18) is transformed to the global laminate coordinate system x_1-x_2-x_3 by tensor transformation, cf. Eq. (2.4):

$$\begin{pmatrix}\sigma_{11}\\ \sigma_{22}\\ \tau_{12}\end{pmatrix}_k = \begin{pmatrix}\overline{Q}_{11} & \overline{Q}_{12} & \overline{Q}_{16}\\ \overline{Q}_{12} & \overline{Q}_{22} & \overline{Q}_{26}\\ \overline{Q}_{16} & \overline{Q}_{26} & \overline{Q}_{66}\end{pmatrix}_k \begin{pmatrix}\varepsilon_{11}\\ \varepsilon_{22}\\ \gamma_{12}\end{pmatrix}. \tag{2.20}$$

The ply-index k is introduced to distinguish between the elements of the transformed reduced stiffness matrix associated with different plies. In this study, only laminated plates with a symmetric stacking with respect to the plate's mid-surface under in-plane loading conditions are considered. Hence, the strains ε_{ij} in Eq. (2.20) correspond to the strains ε^0_{ij} of the plate's mid-surface. Integrating the stresses with respect to the out-of-plane direction through the total thickness h yields:

$$\begin{pmatrix}N_{11}\\ N_{22}\\ N_{12}\end{pmatrix} = \int_{-h/2}^{h/2}\begin{pmatrix}\sigma_{11}\\ \sigma_{22}\\ \tau_{12}\end{pmatrix}\mathrm{d}x_3 = \sum_{k=1}^{n}\int_{h_{k-1}}^{h_k}\begin{pmatrix}\sigma_{11}\\ \sigma_{22}\\ \tau_{12}\end{pmatrix}_k \mathrm{d}x_3. \tag{2.21}$$

Here, h_k indicates the value of the x_3-coordinate corresponding to the material interfaces between the individual layers. This finally leads to the constitutive equation of the laminated composite plate:

$$\begin{pmatrix} N_{11} \\ N_{22} \\ N_{12} \end{pmatrix} = \begin{pmatrix} A_{11} & A_{12} & A_{16} \\ A_{12} & A_{22} & A_{26} \\ A_{16} & A_{26} & A_{66} \end{pmatrix} \begin{pmatrix} \varepsilon_{11}^0 \\ \varepsilon_{22}^0 \\ \gamma_{12}^0 \end{pmatrix}. \tag{2.22}$$

The quantities A_{ij} are denoted as extensional stiffnesses and are given by

$$A_{ij} = \sum_{k=1}^{n} \overline{Q}_{ij}^{(k)} \left(h_k - h_{k-1}\right). \tag{2.23}$$

In case of bending deformation or an anti-symmetric layup of the laminate, additional bending stiffnesses as well as bending-extension coupling stiffness components must be considered (Becker and Gross, 2002, Reddy, 2004, Mittelstedt and Becker, 2016).

State of plane strain

In contrast to a state of plane stress, a state of plane strain is defined by:

$$\varepsilon_{11} = \varepsilon_{11}(x_1, x_2),\ \varepsilon_{22} = \varepsilon_{22}(x_1, x_2),\ \gamma_{12} = \gamma_{12}(x_1, x_2),\ \varepsilon_{33} = \gamma_{13} = \gamma_{23} = 0. \tag{2.24}$$

For isotropic materials, the corresponding stress-strain relations read:

$$\begin{pmatrix} \varepsilon_{11} \\ \varepsilon_{22} \\ \gamma_{12} \end{pmatrix} = \frac{1-\nu^2}{E} \begin{pmatrix} 1 & -\frac{\nu}{1-\nu} & 0 \\ -\frac{\nu}{1-\nu} & 1 & 0 \\ 0 & 0 & \frac{2}{1-\nu} \end{pmatrix} \begin{pmatrix} \sigma_{11} \\ \sigma_{22} \\ \tau_{12} \end{pmatrix}. \tag{2.25}$$

2.1.3 Field equations and boundary conditions

The equilibrium equations in Eq. (2.10) together with the constitutive equations and the strain-displacement relations form 15 equations for the 15 unknowns, that is, $\sigma_{ij}, \varepsilon_{ij}$ and u_i. Consider a domain Ω as sketched in Fig. 2.2 the field equations can be written in the following compact form that is used throughout this work:

$$\left\{ \begin{array}{rcll} \nabla \cdot \boldsymbol{\sigma} & = & 0 & \text{in } \Omega \\ \boldsymbol{\sigma} & = & \mathbb{C} : \nabla \underline{u} & \text{in } \Omega \end{array} \right. \tag{2.26}$$

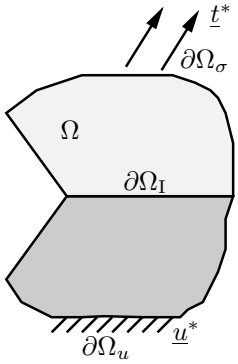

Figure 2.2: Sketch of an inhomogeneous elastic body occupying the domain Ω with associated portions $\partial\Omega_u$ and $\partial\Omega_\sigma$ of the boundary $\partial\Omega$.

In order to uniquely define a solution of the system (2.26) proper boundary conditions must be specified:

$$\left\{\begin{array}{rcll} \boldsymbol{\sigma}\cdot\underline{n} & = & \underline{t}^* & \text{along } \partial\Omega_\sigma \\ \underline{u} & = & \underline{u}^* & \text{along } \partial\Omega_u \\ [\![\underline{u}]\!] & = & 0 & \text{along } \partial\Omega_\mathrm{I} \\ [\![\boldsymbol{\sigma}]\!]\cdot\underline{n} & = & 0 & \text{along } \partial\Omega_\mathrm{I} \end{array}\right. \tag{2.27}$$

The boundary $\partial\Omega$ of the domain Ω is divided into the part $\partial\Omega_\sigma$ where the stress vector $\underline{t}^*$ is prescribed and the part $\partial\Omega_u$ where displacements $\underline{u}^*$ are specified. If multiple materials with different elastic properties are present and the constituents are perfectly bonded along the interface $\partial\Omega_\mathrm{I}$, the jump of displacements as well as of the stress vector must vanish forming the so-called transmission or continuity conditions.

2.1.4 Energy principles

In the following some energy principles that are used throughout this work are discussed. From now on, body forces are set equal to zero. In addition, it is assumed that the temperature of the body remains constant, that is, only isothermal processes are considered. In this case it is suitable to use the Helmholtz free energy F as governing thermodynamic potential. Consider a body occupying the volume Ω bounded by the surface $\partial\Omega$. Combining the first and second law of thermodynamics yields (Ziegler, 1983):

$$\begin{gathered} \dot{K} + \dot{F} = P - \dot{\Phi}, \\ K = \frac{1}{2}\int_\Omega \rho\dot{\underline{u}}\cdot\dot{\underline{u}}\,\mathrm{d}V, \quad F = \int_\Omega \rho f\,\mathrm{d}V, \quad P = \int_{\partial\Omega}\underline{t}\cdot\dot{\underline{u}}\,\mathrm{d}S, \quad \dot{\Phi}\geq 0. \end{gathered} \tag{2.28}$$

These relations state that the power of external forces P diminished by the rate of dissipation $\dot{\Phi}$ during irreversible processes, such as crack growth, is balanced by the change of kinetic energy $\dot{K}$ and the change of reversibly stored energy $\dot{F}$ in the system. In the present case the specific free energy $f = f(\varepsilon_{ij})$ depends only on the strain tensor. Based on Eq. (2.28) the energy balance for an infinitesimal elastic volume element $\mathrm{d}V$ where no dissipation occurs ($\dot{\Phi} = 0$) reads:

$$\rho \, \mathrm{d}V \frac{\mathrm{D}}{\mathrm{D}t} \left(\frac{\dot{u}_i \, \dot{u}_i}{2} + f \right) = (\sigma_{ij} \dot{u}_{i,j} + \sigma_{ij,j} \dot{u}_i) \, \mathrm{d}V. \tag{2.29}$$

The right-hand side of Eq. (2.29) represents the rate of work done by the stresses acting on the surface of the deformable volume element. Another energy statement can be obtained by multiplying the momentum balance (2.9) scalar with the velocity vector $\underline{\dot{u}}$:

$$\rho \, \mathrm{d}V \frac{\mathrm{D}}{\mathrm{D}t} \left(\frac{\dot{u}_i \, \dot{u}_i}{2} \right) = \sigma_{ij,j} \dot{u}_i \, \mathrm{d}V. \tag{2.30}$$

Comparing Eq. (2.29) and Eq. (2.30) shows that one part of the total rate of work done by the stresses is associated with a change in kinetic energy of the volume element whereas the other part is stored in form of free energy (or dissipated in the case of irreversibility). Combining Eq. (2.29) and Eq. (2.30) yields[4]:

$$\left(\rho \frac{\partial f}{\partial \varepsilon_{ij}} - \sigma_{ij} \right) \dot{\varepsilon}_{ij} = 0. \tag{2.31}$$

Since Eq. (2.31) must hold for arbitrary $\dot{\varepsilon}_{ij}$, the stresses can be derived by differentiation of the potential f with respect to the strains. It is common to introduce the so-called strain energy density $U = \rho f$ and Eq. (2.31) takes the form[5]:

$$\sigma_{ij} = \frac{\partial U}{\partial \varepsilon_{ij}}. \tag{2.32}$$

For linear elastic material behaviour an integration of Eq. (2.32) between the undeformed and the deformed state yields:

$$U\left(\varepsilon_{ij}\right) = \int_0^{\varepsilon_{ij}} \sigma_{ij} \mathrm{d}\tilde{\varepsilon}_{ij} = \frac{1}{2} C_{ijkl} \varepsilon_{kl} \varepsilon_{ij} = \frac{1}{2} \sigma_{ij} \varepsilon_{ij} = \frac{1}{2} \boldsymbol{\sigma} : \boldsymbol{\varepsilon}. \tag{2.33}$$

The strain energy stored in the entire elastic body is obtained integrating the volume specific strain energy density U over the entire volume. This defines the elastic potential Π_{int}:

$$\Pi_{\mathrm{int}} = \frac{1}{2} \int_\Omega \boldsymbol{\sigma} : \boldsymbol{\varepsilon} \mathrm{d}V. \tag{2.34}$$

[4]Note that $\sigma_{ij} u_{i,j} = \sigma_{ij} \varepsilon_{ij} + \sigma_{ij} \omega_{ij} = \sigma_{ij} \varepsilon_{ij}$ where ω_{ij} is the skew symmetric infinitesimal rotation tensor.

[5]As outlined in Ziegler (1983), $f \frac{\partial \rho}{\partial \varepsilon}$ is of higher-order in ε and can be neglected compared to $\rho \frac{\partial f}{\partial \varepsilon}$ within linear elasticity theory.

A useful and concise statement of the equations of equilibrium and the strain-displacement relations is given by the principle of virtual work (Rice, 1968, Kanninen and Popelar, 1985). Let $\boldsymbol{\sigma}^{(1)}$ be an arbitrary stress field, which satisfies the equilibrium equations and is in equilibrium with prescribed surface forces $\underline{t}^*$ on $\partial\Omega_\sigma$. Furthermore, let $\underline{u}^{(2)}$ be any continuous and differentiable displacement field with an associated strain field $\boldsymbol{\varepsilon}^{(2)}$ and prescribed values $\underline{u}^*$ on $\partial\Omega_u$. Note that there need not be any connection between the stress field $\boldsymbol{\sigma}^{(1)}$ and the strain field $\boldsymbol{\varepsilon}^{(2)}$. Balancing the internal and external work done by the strains and displacements associated with system (2) on the stresses and prescribed tractions of system (1) yields:

$$\int_\Omega \boldsymbol{\sigma}^{(1)} : \boldsymbol{\varepsilon}^{(2)} \mathrm{d}V = \int_{\partial\Omega_\sigma} \underline{t}^* \cdot \underline{u}^{(2)} \mathrm{d}S + \int_{\partial\Omega_u} \underline{t}^{(1)} \cdot \underline{u}^* \mathrm{d}S. \tag{2.35}$$

Equation (2.35) expresses the principle of virtual work, also referred to as general work theorem (Gross and Seelig, 2017). Given the strain-displacement equations, the virtual work statement implies equilibrium employing the Green-Gauß theorem. Conversely, given a stress field satisfying the equilibrium equation, Eq. (2.35) implies the strain-displacement equations. The principle of virtual work according to Eq. (2.35) proofs very suitable in order to derive further theorems. Consider a linear elastic material and let $\boldsymbol{\sigma}^{(1)}$ and $\boldsymbol{\varepsilon}^{(2)}$ the actual, true quantities of a deformed body. In this case, the left-hand side of Eq. (2.35) can be identified as $2\Pi_{\mathrm{int}}$, cf. Eq. (2.34). Furthermore, supposing that all external forces are dead loads[6] the right-hand side of Eq. (2.35) represents the external work $\int P \mathrm{d}t = W = -\Pi_{\mathrm{ext}}$ done by the external forces during the deformation process. Consequently, Eq. (2.35) can be rewritten as

$$2\Pi_{\mathrm{int}} + \Pi_{\mathrm{ext}} = 0, \tag{2.36}$$

which is referred to as Clapeyron's theorem. According to Clapeyron's theorem, only half of the external potential is saved in a reversible form as strain energy. The remaining part is either converted into kinetic energy or dissipated, cf. Eq. (2.28).

The principle of virtual work is now applied to derive a path independent integral in order to determine the difference in total potential energy $\Delta\Pi = \Delta\Pi_{\mathrm{int}} + \Delta\Pi_{\mathrm{ext}}$ between the two configurations sketched in Fig. 2.3. This serves as a basis for calculating the energy release rate, which is a key property in fracture mechanics. The configuration on the left-hand side occupies the domain $\Omega^{(1)}$ and tractions $\underline{t}^*$ are applied on the portion $\partial\Omega_\sigma$ of the boundary $\partial\Omega^{(1)}$. Inserting a crack leads to the configuration depicted on the right-hand side defining the domain $\Omega^{(2)}$ while the applied traction remains unaltered. In order to use the stress and strain fields associated with the configurations (1) and (2), respectively, as admissible fields within the principle of virtual work, an additional contour Γ is introduced in both configurations in such a way that the crack is fully enclosed. This leads to a domain $\tilde{\Omega} = \Omega^{(1)} \setminus \Omega_\Gamma^{(1)} = \Omega^{(2)} \setminus \Omega_\Gamma^{(2)}$ which both configurations have in common and enables the application of the principle of virtual work. Coupling the stress fields of state (1) with the strain fields of state (2) and vice

[6] External loads are constant and do not change during loading process from the undeformed to the deformed state.

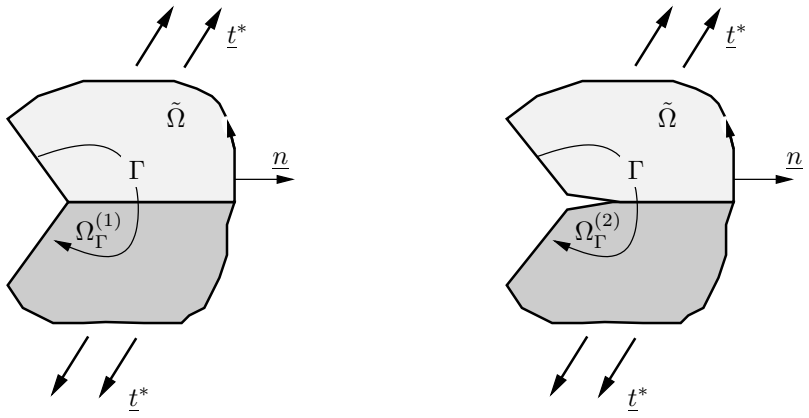

configuration (1) configuration (2)

Figure 2.3: An elastic body in state (1) associated with the domain $\Omega^{(1)}$ before crack formation and in state (2) associated with the domain $\Omega^{(2)}$ after crack formation. The path Γ completely encloses the crack.

versa yields:

$$\int_{\tilde{\Omega}} \boldsymbol{\sigma}^{(1)} : \boldsymbol{\varepsilon}^{(2)} \mathrm{d}V = \int_{\partial\Omega_\sigma} \underline{t}^* \cdot \underline{u}^{(2)} \mathrm{d}S + \int_{\Gamma} \underline{t}^{(1)} \cdot \underline{u}^{(2)} \mathrm{d}S, \tag{2.37}$$

$$\int_{\tilde{\Omega}} \boldsymbol{\sigma}^{(2)} : \boldsymbol{\varepsilon}^{(1)} \mathrm{d}V = \int_{\partial\Omega_\sigma} \underline{t}^* \cdot \underline{u}^{(1)} \mathrm{d}S + \int_{\Gamma} \underline{t}^{(2)} \cdot \underline{u}^{(1)} \mathrm{d}S. \tag{2.38}$$

Employing Hooke's law and using the symmetry properties of the elasticity tensor in Eq. (2.13) leads to the following reciprocity relation, also referred to as Betti's theorem:

$$\int_{\tilde{\Omega}} \boldsymbol{\sigma}^{(1)} : \boldsymbol{\varepsilon}^{(2)} \mathrm{d}V = \int_{\tilde{\Omega}} \boldsymbol{\sigma}^{(2)} : \boldsymbol{\varepsilon}^{(1)} \mathrm{d}V. \tag{2.39}$$

Thus, equating Eq. (2.37) and Eq. (2.38) yields:

$$\int_{\Gamma} \left(\underline{t}^{(2)} \cdot \underline{u}^{(1)} - \underline{t}^{(1)} \cdot \underline{u}^{(2)} \right) \mathrm{d}S = \int_{\partial\Omega_\sigma} \underline{t}^* \cdot \left(\underline{u}^{(2)} - \underline{u}^{(1)} \right) \mathrm{d}S. \tag{2.40}$$

Since the external load $\underline{t}^*$ is assumed to be unchanged, the right-hand side of (2.40) is nothing else but the difference in external potential between state (1) and (2):

$$-\Delta\Pi_{\mathrm{ext}} = -\left(\Pi_{\mathrm{ext}}^{(2)} - \Pi_{\mathrm{ext}}^{(1)} \right) = \int_{\partial\Omega_\sigma} \underline{t}^* \cdot \left(\underline{u}^{(2)} - \underline{u}^{(1)} \right) \mathrm{d}S. \tag{2.41}$$

Following Clapeyron's theorem (2.36), the change in total potential energy is related to the change of external potential by $\Pi^{(2)} - \Pi^{(1)} = \Delta\Pi = 1/2\,\Delta\Pi_{\mathrm{ext}}$. Ultimately, the difference in total potential energy writes:

$$\Pi^{(2)} - \Pi^{(1)} = -\frac{1}{2} \int_{\Gamma} \left(\underline{t}^{(2)} \cdot \underline{u}^{(1)} - \underline{t}^{(1)} \cdot \underline{u}^{(2)} \right) \mathrm{d}S. \tag{2.42}$$

Eq. (2.42) is now rewritten for a two-dimensional modelling with the out-of-plane

thickness d and all involved quantities are expressed in terms of displacements. Furthermore, it is common to evaluate the Ψ-integral in a counterclockwise sense. Thus, changing the direction of integration from clockwise, cf. Fig 2.3, to counterclockwise yields:

$$\Pi^{(2)} - \Pi^{(1)} = \frac{d}{2} \int_{\gamma} \left(\boldsymbol{\sigma} \left(\underline{u}^{(2)} \right) \cdot \underline{n} \cdot \underline{u}^{(1)} - \boldsymbol{\sigma} \left(\underline{u}^{(1)} \right) \cdot \underline{n} \cdot \underline{u}^{(2)} \right) \mathrm{d}s. \tag{2.43}$$

Within a two-dimensional approach, the path of integration is γ and $\mathrm{d}S = d\,\mathrm{d}s$. The integral on the right-hand side of Eq. (2.43) will play an essential role throughout the present work and is denoted as Ψ-integral:

$$\Psi \left(\underline{u}^{(2)}, \underline{u}^{(1)} \right) = \frac{1}{2} \int_{\gamma} \left(\boldsymbol{\sigma} \left(\underline{u}^{(2)} \right) \cdot \underline{n} \cdot \underline{u}^{(1)} - \boldsymbol{\sigma} \left(\underline{u}^{(1)} \right) \cdot \underline{n} \cdot \underline{u}^{(2)} \right) \mathrm{d}s. \tag{2.44}$$

The Ψ-integral yields the difference in total potential energy per unit width between the two states (2) and (1). A very advantageous property of the Ψ-integral is its path independence which is why this integral is also of importance for further applications such as the extraction of generalised stress intensity factors. From a physical point of view, the path independence of the Ψ-integral is quite intuitive since there was no assumption made on a specific contour γ in the derivation above. Thus, evaluating the integral along a different contour γ^* which also fully encloses the crack yields exactly the same difference in total potential energy implying path independence of the integral. A more technical proof of the path independence property can be found in Yosibash (2011).

2.2 Complex potential method

The method of complex potentials provides a very efficient approach to solve two-dimensional problems of linear elasticity. Instead of tackling the problem in the physical space defined by the coordinates x_1 and x_2, stresses and strains are considered as functions of the complex variable $z = x_1 + \mathrm{i}x_2$. This leads to the very suitable feature that the governing field equations of linear elasticity in Eq. (2.26) are satisfied introducing two arbitrary complex potentials $\Phi_1(z)$ and $\Phi_2(z)$. As outlined in classical textbooks by Muskhelishvili (1963) and Savin (1961) stresses and strains are given by the so-called Kolosov-Muskhelishvili formulas

$$\begin{aligned} u_r + \mathrm{i}u_\varphi &= \frac{1}{2G} \left(\kappa \Phi_1(z) - z\overline{\Phi_1'(z)} - \overline{\Phi_2(z)} \right) e^{-\mathrm{i}\varphi}, \\ \sigma_{rr} + \sigma_{\varphi\varphi} &= 2 \left(\Phi_1'(z) + \overline{\Phi_1'(z)} \right), \\ \sigma_{\varphi\varphi} - \sigma_{rr} + 2\mathrm{i}\tau_{r\varphi} &= 2 \left(z\Phi_1''(z) + \Phi_2'(z)\frac{z}{\overline{z}} \right), \end{aligned} \tag{2.45}$$

with

$$\kappa = \begin{cases} \dfrac{3-\nu}{1+\nu} & \text{for plane stress,} \\ 3-4\nu & \text{for plane strain.} \end{cases} \tag{2.46}$$

The complex potential method has been extended by Lekhnitskii (1963) to anisotropic materials introducing the generalised complex variables $z_i = x_1 + \mu_i x_2$. Stresses and displacements are then related to the complex potentials $\Phi_1(z_1)$ and $\Phi_2(z_2)$ by:

$$\begin{aligned}
\sigma_{rr} &= 2\mathrm{Re}\left[\sum_{i=1}^{2} \left(\sin(\varphi) - \mu_i \cos(\varphi)\right)^2 \Phi_i'(z_i)\right], \\
\sigma_{\varphi\varphi} &= 2\mathrm{Re}\left[\sum_{i=1}^{2} \left(\cos(\varphi) + \mu_i \sin(\varphi)\right)^2 \Phi_i'(z_i)\right], \\
\tau_{r\varphi} &= 2\mathrm{Re}\left[\sum_{i=1}^{2} \left(\sin(\varphi) - \mu_i \cos(\varphi)\right)\left(\cos(\varphi) + \mu_i \sin(\varphi)\right) \Phi_i'(z_i)\right], \\
u_r &= 2\mathrm{Re}\left[\sum_{i=1}^{2} \left(p_i \cos(\varphi) + q_i \sin(\varphi)\right) \Phi_i(z_i)\right], \\
u_\varphi &= 2\mathrm{Re}\left[\sum_{i=1}^{2} \left(q_i \cos(\varphi) - p_i \sin(\varphi)\right) \Phi_i(z_i)\right].
\end{aligned} \tag{2.47}$$

The complex quantities μ_i are the roots of the characteristic equation

$$S_{11}\mu^4 - 2S_{16}\mu^3 + (2S_{12} + S_{66})\mu^2 - 2S_{26} + S_{22} = 0, \tag{2.48}$$

with the compliance components S_{ij} as introduced in Eq. (2.15). The quantities p_i and q_i are given by

$$\begin{aligned}
p_1 &= S_{11}\mu_1^2 + S_{12} - S_{16}\mu_1, & p_2 &= S_{11}\mu_2^2 + S_{12} - S_{16}\mu_2, \\
q_1 &= S_{12}\mu_1 + \tfrac{S_{22}}{\mu_1} - S_{26}, & q_2 &= S_{12}\mu_2 + \tfrac{S_{22}}{\mu_2} - S_{26}.
\end{aligned} \tag{2.49}$$

The challenging part employing the complex potential method is to choose the potentials in such a way that the prescribed boundary conditions are fulfilled. One way which is followed in this work is to assume a series expansion for the complex potentials and adequately determine the involved coefficients. More sophisticated approaches and methods, such as conformal mapping, are discussed in detail by Muskhelishvili (1963).

2.3 Introduction to fracture mechanics

The general field of fracture mechanics provides a quantitative description to characterize and assess the resistance of materials to crack initiation and growth. From a historical point of view, the work of Griffith (1921) is commonly acknowledged as the beginning of representing fracture mechanics as a quantitative science. About three decades

later Irwin (1957) provided an alternative approach in order to assess the strength of a cracked solid. Irwin reformulated a criterion for fracture, which ultimately has led to a breakthrough of fracture mechanics and its use in engineering science. A more detailed discussion on the history of fracture mechanics can be found in Gross and Seelig (2017), Broberg (1999), Cherepanov (1979) and Kanninen and Popelar (1985).

In this work, a macroscopic continuum-mechanical description of the fracture behaviour is employed where microscopic events are not explicitly modelled. The region in which complex microscopic processes of bond breaking take place is denoted as process zone. Using a continuum-mechanical approach, the size of the process zone must be negligibly small in comparison to any characteristic macroscopic length of the body. Furthermore, the fracture event is supposed to be brittle, that is, only a small amount of inelastic deformation occurs on a macroscopic scale. Additionally, the region of possible inelastic deformation outside the process zone is assumed to be negligibly small from a macroscopic point of view. This defines the framework of linear elastic fracture mechanics (LEFM) where the entire body is regarded as linear elastic and the stress and displacement fields follow from linear elasticity theory.

2.3.1 Linear elastic fracture mechanics

The presence of a crack or a notch due to material or geometric discontinuities induces a highly localised stress concentration. In the framework of linear elasticity, stresses even have a singular character which means that mathematically infinite stresses arise right a the notch tip. Such singularities clearly represent an artefact of the simplified linear theory and are not observable in reality since inelastic deformation of the material takes place. However, if the plastic zone is sufficiently small as supposed in LEFM, the stress field in the vicinity of the notch tip is quite well captured by linear elasticity as schematically shown in Fig. 2.4. Since stress concentrations appear very localised and brittle crack formation is governed by the local stress field in the vicinity of the notch-tip, the near-tip fields are of particular interest for a fracture mechanics analysis. It was first shown by Williams (1952), that stresses and displacements in the vicinity of a sharp, homogeneous notch could be written in form of a series expansion (also referred to as Williams expansion) with respect to the radial distance r from the notch tip:

$$\begin{aligned} \underline{u} &= \sum_{k=1}^{\infty} K_k r^{\lambda_k} \underline{u}_k(\varphi), \\ \boldsymbol{\sigma} &= \sum_{k=1}^{\infty} K_k r^{\lambda_k - 1} \boldsymbol{\sigma}_k(\varphi). \end{aligned} \tag{2.50}$$

As observed in Eq. (2.50), the behaviour of the field variables with respect to the radial direction is characterised by the exponents λ_i which are arranged as $\lambda_k \leq \lambda_{k+1}$. The behaviour in circumferential direction is defined by the eigenfunctions $\underline{u}_k(\varphi)$ and $\boldsymbol{\sigma}_k(\varphi)$, respectively. Although originally derived for the case of a homogeneous notch, the expansion (2.50) also holds in the case of multi-material situations (Cherepanov,

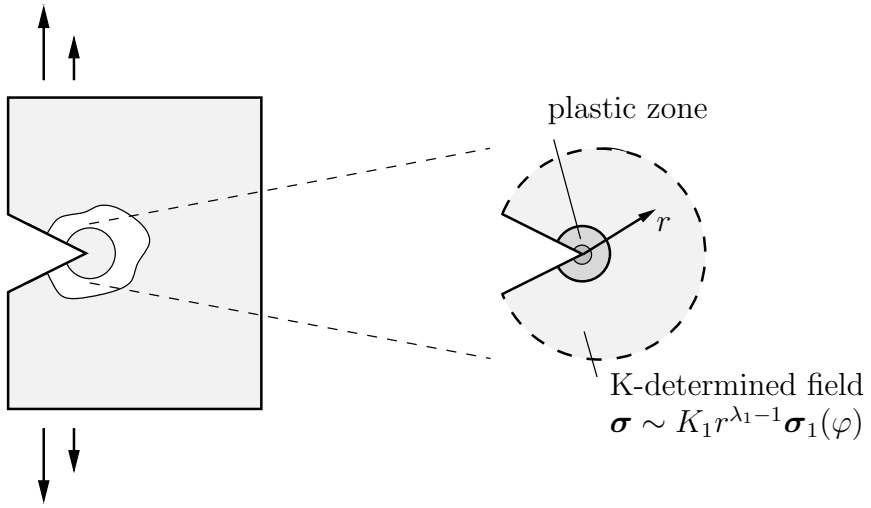

Figure 2.4: Global structure and vicinity of the notch-tip. The process zone (dark grey) and plastic zone are well embedded in the linear elastic K-determined field.

1979, Zak and Williams, 1963, Felger et al., 2019a,b). The exponents λ_i, referred to as eigenvalues, as well as the eigenfunctions $\underline{u}_k(\varphi)$ and $\boldsymbol{\sigma}_k(\varphi)$ are generalised quantities. They are completely defined using asymptotic analysis and depend only on the local notch geometry, e.g. the notch opening angle or the elastic mismatch of the constituents. The coefficients K_i, scaling each eigensolution are denoted as generalised stress intensity factors (GSIFs). The GSIFs are global quantities depending on the overall, global geometry of the structure as well as the far-field loading conditions. Consequently, the GSIFs cannot be determined solely based on asymptotic analysis but instead require the complete solution of the underlying BVP[7] Based on the expansions in Eq (2.50), the following classification and restrictions for the exponents λ_i can be deduced:

$$\begin{array}{rl} \lambda_i \geq 0: & \text{bounded strain energy } \Pi_{\text{int}} < \infty, \\ \lambda_i = 0: & \text{rigid body translations,} \\ 0 < \lambda_i \leq 1: & \text{singular stresses for } r \to 0\ , \\ \lambda_i = 1: & \text{rigid body rotation or state of homogeneous stress,} \\ \lambda_i \geq 1: & \text{bounded stresses for } r \to 0\ . \end{array} \tag{2.51}$$

If the exponent λ_i is smaller than one, unbounded stresses occur at the origin $r = 0$ forming a stress singularity. In this case, λ_i is also denoted as singularity exponent. However, the exponent λ_i must not attain negative values in order to represent a well-defined solution satisfying the physical requirement of bounded strain energy. The special case of a crack is of fundamental importance in fracture mechanics. In the two-dimensional case, the asymptotic expansion of the stress field in the vicinity of the crack in a homogeneous material reads:

$$\boldsymbol{\sigma} \sim K_1^{\mathrm{I}} r^{-1/2} \boldsymbol{\sigma}_1^{\mathrm{I}}(\varphi) + K_1^{\mathrm{II}} r^{-1/2} \boldsymbol{\sigma}_1^{\mathrm{II}}(\varphi) \quad \text{as} \quad r \to 0. \tag{2.52}$$

[7] In contrast to cracks where the stress intensity factor is defined by $K_{\mathrm{I}} = \lim_{r \to 0} \sqrt{2\pi r}\, \sigma_{\varphi\varphi}(\varphi = 0)$ there is no established convention in literature for generalised stress intensity factors.

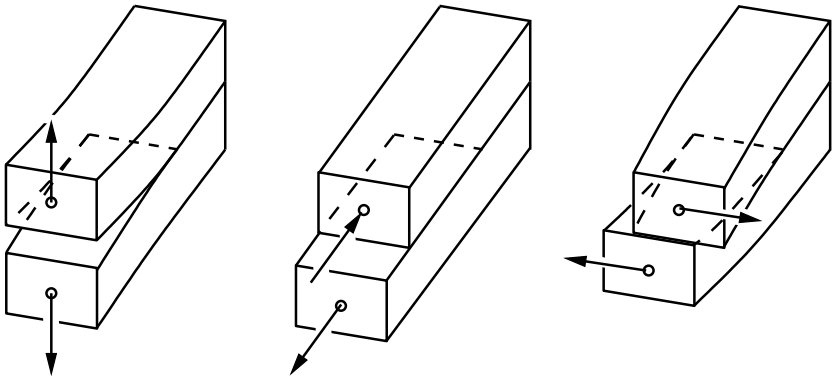

Figure 2.5: Crack opening modes.

Here, the symbol "$\sim$" means "asymptotically equal to". On account of Eq. (2.52), the stresses are singular right at the crack tip and display a characteristic $1/\sqrt{r}$ behaviour in radial direction. Moreover, the two leading-order terms have an identical singularity exponent. These terms are indicated with I and II, respectively and are associated with different deformation modes or crack-opening modes. According to Fig. 2.5, a mode I corresponds to a symmetric crack-opening mode whereas a mode II deformation represents an anti-symmetric deformation. In the three-dimensional case, a further anti-symmetric mode III exists. In a general loading case, all modes are triggered simultaneously which is referred to as mixed-mode condition. The intensity of the mode I and mode II contribution is given by the intensity factors K_1^{I} and K_1^{II}, respectively. It was Irwin who proposed a criterion for fracture stating that crack growth takes place if the present intensity factor reaches a critical value. For pure mode I, II and III conditions, the fracture criterion yields:

$$K_1^{\mathrm{I}} = K_{\mathrm{Ic}}, \quad K_1^{\mathrm{II}} = K_{\mathrm{IIc}}, \quad K_1^{\mathrm{III}} = K_{\mathrm{IIIc}}. \tag{2.53}$$

The criterion according to Eq. (2.53) is also referred to as K-concept. The quantities $K_{\mathrm{Ic}}, K_{\mathrm{IIc}}$ and K_{IIIc} are called fracture toughnesses. Each fracture toughness represents a material parameter, which is determined by appropriate experimental tests, e.g. a compact tension test, a three-point bending test according to the ASTM–Standard E399-90 or a DCB test in combination with the J-integral as outlined in Rosendahl et al. (2019c). In case of mixed-mode conditions, the fracture criterion of Eq. (2.53) must be generalised, cf. Gross and Seelig (2017).

Besides using stress intensity factors (K-concept), the energy balance during crack formation plays an essential role and serves as a basis for formulating fracture criteria. On account of Eq. (2.28), the energy balance reads

$$\dot{K} + \dot{\Pi} + \dot{\Phi} = 0, \tag{2.54}$$

where $\dot{\Phi} \geq 0$ represents the rate of energy dissipation during crack growth and the existence of an external potential is supposed. Based on the work by Griffith (1921), the dissipation $\mathrm{d}\Phi$ due to infinitesimal crack growth $\mathrm{d}A = d\,\mathrm{d}a$ takes the

form

$$\mathrm{d}\Phi = \mathcal{G}_c(A)\dot{A}\,\mathrm{d}t = d\,\mathcal{G}_c(a)\,\mathrm{d}a. \tag{2.55}$$

The quantity $\mathcal{G}_c$ is called crack resistance, critical energy release rate or fracture toughness and represents a material property. Substituting Eq. (2.55) into the energy balance Eq. (2.54) and neglecting inertia effects ($\mathrm{d}K = 0$) yields the energy criterion:

$$-\frac{\mathrm{d}\Pi}{\mathrm{d}A} = \mathcal{G} = \mathcal{G}_c. \tag{2.56}$$

The quantity $\mathcal{G}$ is called energy release rate (ERR). The energy criterion in Eq. (2.56) states, that an existing crack starts to grow if the rate of energy released during infinitesimal crack propagation equals the energy consumed by the fracture process. The energy dissipation can be explicitly calculated for instance by means of the so-called crack-closure integral (Gross and Seelig, 2017). This yields a connection between the ERR and the stress intensity factors. For pure mode I, II and mode III loading, respectively, it follows[8]:

$$\underbrace{\mathcal{G}_{\mathrm{I}} = \frac{\kappa+1}{8G}\left(K_1^{\mathrm{I}}\right)^2}_{\text{mode I}}, \quad \underbrace{\mathcal{G}_{\mathrm{II}} = \frac{\kappa+1}{8G}\left(K_1^{\mathrm{II}}\right)^2}_{\text{mode II}}, \quad \underbrace{\mathcal{G}_{\mathrm{III}} = \frac{1}{2G}\left(K_1^{\mathrm{III}}\right)^2}_{\text{mode III}}. \tag{2.57}$$

On account of Eq. (2.57), the energy based criterion is equivalent to the K-concept for pure modes. If mixed-mode conditions are present, it follows in the general three-dimensional case:

$$\mathcal{G} = \frac{\kappa+1}{8G}\left(\left(K_1^{\mathrm{I}}\right)^2 + \left(K_1^{\mathrm{II}}\right)^2\right) + \frac{1}{2G}\left(K_1^{\mathrm{III}}\right)^2. \tag{2.58}$$

2.3.2 Calculation of generalised stress intensity factors (GSIFs)

In contrast to the eigenvalues and eigenfunctions as local quantities, the intensity factors K_i are global quantities depending on the structure's overall geometry as well as on the loading conditions. Since a solution of the complete BVP is required for their calculation, FEA is employed and the intensity factors are extracted from the numerical solution. Out of the existing methods in literature, the contour integral method (CIM) also referred to as dual-singular function method or reciprocal work contour method has proven to be well suited for calculating GSIFs and is used in the present work. The CIM relies on the previously introduced path independent Ψ-integral (2.44) which in fact plays a double role, that is, calculating the difference in total potential energy and GSIF extraction. The path independence enables to evaluate the integral in a certain distance away from the singularity. This avoids the numerical issue of accurately capturing the field variables in the close vicinity of the singularity as it is necessary in alternative approaches (Carpinteri, 1987, Dunn et al., 1997c,b).

[8]Note that these relations are based on a specific normalisation of the crack-tip fields.

As shown in detail in Section 3, the exponents and eigenfunctions represent the solution of an eigenvalue problem. An important property of the associated characteristic equation is that to every positive solution $\lambda_i > 0$ there exists an associated negative solution $-\lambda_i$. Thus, to every eigenvalue-eigenfunction pair $\{\lambda_i, \underline{u}_i\}$, denoted as primal solution, there is a corresponding combination $\{-\lambda_i, \underline{u}_{-i}\}$ referred to as dual solution. Every dual solution satisfies the governing field equations of linear elasticity as well as presumed boundary and transmission conditions of the local notch configuration. However, according to Eq. (2.51), dual solutions imply unbounded strain energy[9] and thus do not possess a physical meaning at first sight[10]. In terms of GSIF calculation, dual functions play solely a mathematical role and represent an essential part to extract the GSIF out of a numerical solution. The idea of GSIF extraction using CIM relies on the bi-orthogonality property of the Ψ-integral. This can be derived using the primal and associated dual eigensolutions as input of the Ψ-integral in Eq. (2.44):

$$\underline{u}^{(1)} = r^{\lambda_i}\underline{u}_i(\varphi), \quad \underline{u}^{(2)} = r^{-\lambda_j}\underline{u}_{-j}(\varphi). \tag{2.59}$$

Since the Ψ-integral is path independent, a circular integration path with radius R is chosen for sake of simplicity. This yields:

$$\Psi\left(r^{\lambda_i}\underline{u}_i, r^{-\lambda_j}\underline{u}_{-j}\right) = \frac{R^{\lambda_i-\lambda_j}}{2}\int_\gamma \left(\boldsymbol{\sigma}_i \cdot \underline{n} \cdot \underline{u}_{-j} - \boldsymbol{\sigma}_{-j} \cdot \underline{n} \cdot \underline{u}_i\right) \mathrm{d}\varphi. \tag{2.60}$$

As a consequence of the integral's path independence, the right-hand side of Eq. (2.60) must not depend on the radius R. This implies that the integral on the right-hand side must vanish for $i \neq j$ leading to:

$$\Psi\left(r^{\lambda_i}\underline{u}_i(\varphi), r^{-\lambda_j}\underline{u}_{-j}(\varphi)\right) = 0 \quad \text{for} \quad i \neq j. \tag{2.61}$$

The relation in Eq. (2.61) is denoted as bi-orthogonality property of the Ψ-integral and represents the key property within the GSIF extraction procedure. In order to compute the GSIF K_i a numerical solution $\underline{u}^{\mathrm{FE}}$ of the corresponding BVP is generated using FEA. Subsequently, the Ψ-integral is evaluated using $\underline{u}^{\mathrm{FE}}$ and the dual solution $r^{-\lambda_i}\underline{u}_{-i}(\varphi)$ as input data. Since the numerical solution can be generally represented as an infinite series expansion, it follows:

$$\Psi\left(\underline{u}^{\mathrm{FE}}, r^{-\lambda_i}\underline{u}_{-i}(\varphi)\right) = \Psi\left(\sum_{k=1}^{\infty} K_k r^{\lambda_k}\underline{u}_k(\varphi), r^{-\lambda_i}\underline{u}_{-i}(\varphi)\right). \tag{2.62}$$

Exploiting the bi-linearity of the Ψ-integral, Eq. (2.62) can be rewritten as

$$\Psi\left(\underline{u}^{\mathrm{FE}}, r^{-\lambda_i}\underline{u}_{-i}(\varphi)\right) = \sum_{k=1}^{\infty} K_k \Psi\left(r^{\lambda_k}\underline{u}_k(\varphi), r^{-\lambda_i}\underline{u}_{-i}(\varphi)\right). \tag{2.63}$$

According to the bi-orthogonality property in Eq. (2.61), all terms with $k \neq -i$ vanish in Eq. (2.63). This ultimately yields the desired relation for the intensity

[9] Supposed that the point corresponding to $r \to 0$ is located within the problem's domain.

[10] Indeed, within the framework of matched asymptotic expansions outlined in Section 3, dual solutions have a physical meaning.

factor:

$$K_i = \frac{\Psi\left(\underline{u}^{\mathrm{FE}}, r^{-\lambda_i}\underline{u}_{-i}(\varphi)\right)}{\Psi\left(r^{\lambda_i}\underline{u}_i(\varphi), r^{-\lambda_i}\underline{u}_{-i}(\varphi)\right)}. \tag{2.64}$$

Thus, the dual solutions play the mathematical role of an extraction function.

2.4 Finite fracture mechanics and the coupled stress and energy criterion

The Griffith energy criterion as well as the K-concept have a clear restriction: these criteria are only applicable if a pre-existing crack is present. In terms of crack initiation, the energy release rate $\mathcal{G}$ vanishes if the length of an existing crack tends to zero[11]. Hence, an energy criterion according to Eq. (2.56) can never be fulfilled and does not yield physical results. This restriction has been overcome by the concept of finite fracture mechanics (FFM) as originally proposed by Hashin (1996) for brittle failure. Following the idea of FFM, the process of crack initiation is modelled as an instantaneous formation of a finite sized crack. The crack nucleation process is regarded as a fracture event appearing in a very short time and it is neither possible nor of interest to resolve this time scale and explicitly follow its development. In this modelling approach the finite crack length forms a new unknown in contrast to classical fracture mechanics, which is restricted to infinitesimal crack growth. In order to determine the failure load at the nucleation σ_{f} and the remaining unknowns such as the finite crack length Δa or the angle of crack initiation, Leguillon (2002) proposed a coupled criterion (CC) consisting of a stress and an energy criterion.

The stress criterion is formulated by means of an equivalent stress function $g(\sigma_{ij})$ relating the stresses to the corresponding material strength. The stress criterion can then be written in the form

$$g(\boldsymbol{\sigma}(\underline{x})) \geq 1 \ \forall \underline{x} \in \partial\Omega_{\mathrm{C}}, \tag{2.65}$$

where $\partial\Omega_{\mathrm{C}}$ represents the potential crack surface. In case of mixed-mode conditions where normal stresses σ_{nn} as well as shear stresses τ_{nt} are present on the potential crack path, a criterion of the form[12]

$$g = \left[\left(\frac{<\sigma_{\mathrm{nn}}>}{\sigma_{\mathrm{c}}}\right)^p + \left(\frac{\tau_{\mathrm{nt}}}{\tau_{\mathrm{c}}}\right)^p\right]^{\frac{1}{p}} \geq 1 \tag{2.66}$$

is employed. The parameter p controls the shape of the failure curve. Setting $p = 1$ corresponds to a Mohr-Coulomb-type criterion whereas $p \to \infty$ yields a rectangular region without an interaction of shear and normal contribution. In this work, $p = 2$ is used which corresponds to an elliptical failure curve and has proven to be in a good agreement with experimental data (García and Leguillon, 2012, Seweryn et al., 1997).

[11] See Eq. (3.34).
[12] $< x >= x^+ = \max(0, x)$

Alternatively, a maximum principal stress criterion could be used. However, as the crack path does not necessarily follow the associated principal directions, the maximum principal stress criterion appears not very intuitive in the approach followed in the present work. Additional, more generalised criteria can be found in Rosendahl et al. (2019a,b).

The energy criterion is established based on the energy balance. In the spirit of a Griffith-type approach within classical LEFM, the dissipation $\Delta\Phi$ due to the initiation of a finite crack of size $\Delta A = d\,\Delta a$ takes the form

$$\Delta\Phi = d\int_0^{\Delta a} \mathcal{G}_c(a)\mathrm{d}a. \tag{2.67}$$

The fracture toughness $\mathcal{G}_c$ can be dependent on the crack length a. The energy balance is then evaluated between the state before and after crack onset. If the initial state prior to the fracture event is in equilibrium, the kinetic energy can only increase which yields:

$$\Delta\Pi + d\int_0^{\Delta a} \mathcal{G}_c(a)\mathrm{d}a \leq 0. \tag{2.68}$$

The energy criterion is formulated dividing Eq. (2.68) by the crack size $\Delta A = d\Delta a$:

$$-\frac{\Delta\Pi}{\Delta A} = \bar{\mathcal{G}} = \frac{1}{\Delta a}\int_0^{\Delta a} \mathcal{G}(a)\mathrm{d}a \geq \frac{1}{\Delta a}\int_0^{\Delta a} \mathcal{G}_c(a)\mathrm{d}a. \tag{2.69}$$

The quantity $\bar{\mathcal{G}}$ is denoted as the incremental energy release rate (IERR) and represents the finite counterpart to the differential energy release rate $\mathcal{G} = -\mathrm{d}\Pi/\mathrm{d}A$ in classical LEFM. One possibility to account for the effect of mixed-mode conditions on the energy dissipation is to introduce a mixed-mode angle χ defined by the ratio of the shear and normal tractions acting on the potential crack path (Mantič, 2009, Muñoz-Reja et al., 2016, García and Leguillon, 2012):

$$\chi = \tan^{-1}\left(\frac{\tau_{\mathrm{nt}}(a)}{\sigma_{\mathrm{nn}}(a)}\right). \tag{2.70}$$

Hence, the mixed-mode angle χ is a measure of mode II to mode I loading conditions and the fracture toughness is regarded as a function $\mathcal{G}_c(\chi(a), a)$ depending on χ. In this work it is assumed that the fracture toughness depends only on the mixed-mode angle $\mathcal{G}_c(\chi(a))$, neglecting an additional influence of the crack length itself. Furthermore, the phenomenological law proposed by Hutchinson and Suo (1991) is employed, relating the effective fracture toughness $\mathcal{G}_{\mathrm{c}}$ to the mode I contribution $\mathcal{G}_{\mathrm{Ic}}$, the mode II contribution $\mathcal{G}_{\mathrm{IIc}}$ and the mixed mode angle χ:

$$\mathcal{G}_{\mathrm{c}} = \mathcal{G}_{\mathrm{Ic}}\left(1 + \tan^2\left[(1-\Lambda)\chi\right]\right). \tag{2.71}$$

The dimensionless parameter Λ is given by

$$\Lambda = 1 - \frac{2}{\pi}\tan^{-1}\left(\sqrt{\frac{\mathcal{G}_{\mathrm{IIc}}}{\mathcal{G}_{\mathrm{Ic}}} - 1}\right). \tag{2.72}$$

Thus, for the special case of $\mathcal{G}_{\mathrm{IIc}} = \mathcal{G}_{\mathrm{Ic}}$, it follows that $\Lambda = 1$ and the toughness $\mathcal{G} = \mathcal{G}_{\mathrm{Ic}}$ is independent of the mixed-mode angle. Alternatively, the energy criterion can be formulated by separating the energy released during crack initiation into the parts associated with a crack opening mode I and II, respectively and relate each part to its corresponding fracture toughness:

$$\sqrt{\left(\frac{\mathcal{G}_{\mathrm{I}}}{\mathcal{G}_{\mathrm{Ic}}}\right)^2 + \left(\frac{\mathcal{G}_{\mathrm{II}}}{\mathcal{G}_{\mathrm{IIc}}}\right)^2} \geq 1. \tag{2.73}$$

However, the criterion in Eq. (2.73) requires the mode I and mode II contributions $\mathcal{G}_{\mathrm{I}}, \mathcal{G}_{\mathrm{II}}$ to be known, which is not feasible within the present asymptotic framework.

Within Leguillon's coupled criterion, the energy criterion plays the role of a lower bound for the crack length whereas the stress criterion forms an upper bound. The coupled criterion predicts crack onset if both, the stress and the energy criterion are fulfilled simultaneously. In the general case the corresponding failure load F_{f} can be obtained solving the following optimization problem:

$$F_{\mathrm{f}} = \min_{\Delta a, F, \eta_i} \left\{ F \;\middle|\; g\left(\boldsymbol{\sigma}\left(\underline{x}\right)\right) \geq 1 \;\forall \underline{x} \in \partial\Omega_{\mathrm{C}} \quad \wedge \quad \bar{\mathcal{G}} \geq \frac{1}{\Delta a}\int_0^{\Delta a} \mathcal{G}_{\mathrm{c}}(\chi(a))\mathrm{d}a \right\}. \tag{2.74}$$

All variables affecting the optimisation problem in addition to F and Δa are denoted with η_i and are further specified throughout this work.

The coupled criterion provides a criterion for crack onset and it is naturally to ask what happens afterwards. Since a crack is present after nucleation, this question can be answered based on classical LEFM employing the ERR. On account of Eq. (2.69), the following relation holds for the ERR of an initiated crack with length Δa:

$$\mathcal{G}(\Delta a) = \Delta a \frac{\mathrm{d}\bar{\mathcal{G}}(\Delta a)}{\mathrm{d}(\Delta a)} + \bar{\mathcal{G}}(\Delta a). \tag{2.75}$$

For crack nucleation to take place $\bar{\mathcal{G}}(\Delta a) \geq \mathcal{G}_c$ holds and $\Delta a > 0$. If the IERR is an increasing function with respect to the crack length at Δa, it follows:

$$\mathcal{G}(\Delta a) > \mathcal{G}_c. \tag{2.76}$$

In this case, the initiated crack continues to grow which is why crack onset is often associated with unstable crack propagation leading to catastrophic failure of the specimen.

Chapter 3

Extended asymptotic framework for energy release during crack onset

In this section, the method of matched asymptotic expansions is employed in order to derive a series expansion for the change in potential energy and the associated IERR due to crack formation. At the outset, the asymptotic stress and displacement field in the vicinity of a bi-material notch is established using the method of complex potentials. Based on the work by Leguillon (1999), Leguillon and Sanchez-Palencia (1987) and Leguillon (1993), the singular perturbed problem of an elastic body containing a small crack is given and the matched asymptotic expansions framework is established starting with the leading-order term approximation. Subsequently, the asymptotic series is extended by higher-order terms taking into account complex, oscillatory solutions. In this context, a very valuable symmetry property that is known in literature from a numerical point of view is rigorously proven for the first time. The section ends with a description of higher-order correction terms. Based on a model problem as used in Felger and Becker (2017a) the effects and implications of these terms on the asymptotic description of energy dissipation is discussed.

3.1 Introduction

In order to evaluate the CC, the stresses in the uncracked state as well as the IERR due to crack formation must be determined. In terms of computational costs, the IERR is the challenging part since a new BVP must be solved for each admissible crack configuration. In the presence of stress concentrations and presuming brittle fracture, crack initiation is mainly triggered by the local notch stress field and the length of the nucleated crack is typically much smaller in comparison to a characteristic structural length. Hence, two length scales are involved modelling the phenomena of crack formation: the crack length itself representing the small scale and the macroscopic structural length. If the crack length is sufficiently small compared to any characteristic structural length, methods of asymptotic analysis can be used very advantageously. Instead of solving the governing BVP of the cracked (perturbed) state on the perturbed domain, two asymptotic descriptions characterising the solution behaviour on different scales are employed: the outer expansion defined on the outer domain and the inner expansion defined on the inner domain. Subsequently, inner and outer expansions are connected using a matching principle.

For motivation purpose, consider the bi-material configuration with a crack along the interface according to Fig. 3.1. The crack length Δa, however, is small compared to the

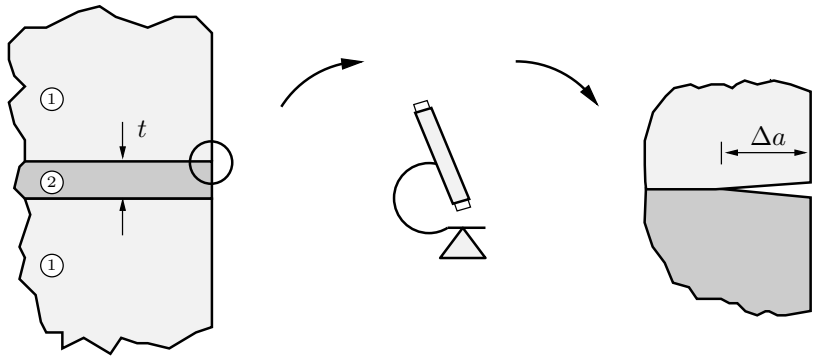

Figure 3.1: Sketch of a bi-material joint configuration with a small crack of length Δa.

macroscopic length t and is barely visible on a macroscopic scale. Performing a zoom-in view as shown on the right-hand side, the small crack of length Δa becomes visible. In the asymptotic case of a very small crack, a large zoom factor is needed in order to resolve the crack. This leads to the effect that information on the macroscopic length scale gets lost, cf. Fig. 3.1 on the right-hand side. Putting it slightly differently, on a scale defined by the macroscopic length t, the small crack is not visible and on a scale such that the crack length is resolved, the macroscopic length can no longer be captured. This essentially motivates the idea of matched asymptotic expansions invoking two domains, that is, a macroscopic outer domain characterised by a macroscopic length and an enlarged inner domain characterised by the crack length. There are two advantageous features using the method of matched asymptotic expansions. First, from a numerical point of view, both length scales can be treated separately instead of using one numerical model where both length scales must be resolved simultaneously. This means that the outer problem depends on the global geometry and the loading conditions of the structure whereas the inner problem is only affected by the local geometry of the notch and the crack. Thus, the inner problem is solved universally once for all and the solution can be used for many other configurations. Second, explicit relations for the IERR are obtained further reducing computational effort. Employing the method of matched asymptotic expansions yields a series expansion of the IERR and its leading-order term writes:

$$\bar{\mathcal{G}} \sim K_1^2 \Delta a^{2\lambda_1 - 1} \Psi_{11} \quad \text{as} \quad \Delta a \to 0. \tag{3.1}$$

Here, only one FEA is needed to determine the scaling coefficient Ψ_{11}. Alternatively, a purely numerical approach can be followed in order to compute $\bar{\mathcal{G}}(\Delta a)$. Since the crack length is a priori unknown within FFM, numerous FEA have to be performed varying the crack length. Typically, a discretisation using 20 values for Δa suffices to adequately render the behaviour of the IERR. This results in a saving of 19 FEA employing asymptotics, or to put it slightly differently, a saving of 95%. Consequently, the more parameters affect the energy dissipation, for instance if the angle of crack initiation is considered as an additional unknown as in Section 4.4, the higher the saving in absolute numbers. Extrapolating further and thinking of the practically important scenario where not only one but numerous notches exist and the point of crack initiation is a priori unknown, it becomes clear that a purely numerical approach will end up in

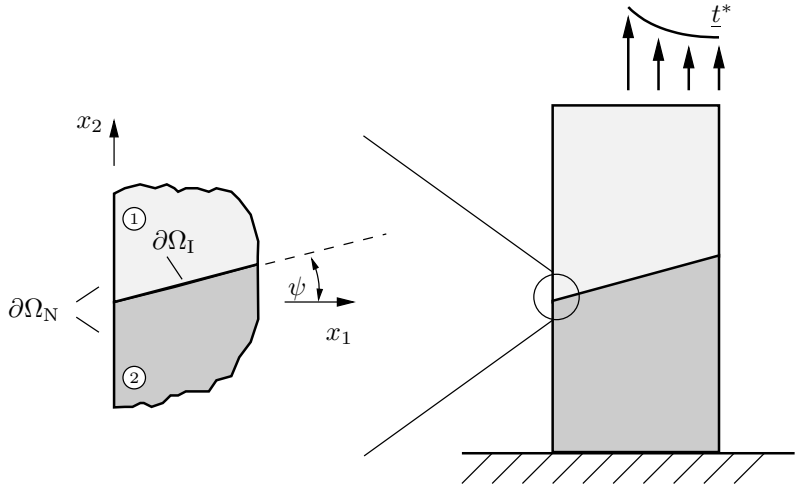

Figure 3.2: Sketch of a bi-material joint and its local notch configuration. The notch faces are denoted as $\partial\Omega_\mathrm{N}$, $\partial\Omega_\mathrm{I}$ is the material interface and the interface orientation is characterised by the angle ψ.

enormous computation costs. For these reasons, the method of MAE is used throughout the present work in order to efficiently calculate the IERR for cracks emanating from bi-material notches and sharp corners (Section 4) as well as from rounded notches (Section 5).

3.2 Asymptotic expansion of stresses and displacements at the notch-tip

Consider exemplarily the bi-material notch configuration depicted in Fig. 3.2. Let us focus on the bi-material notch to the far left, where the location of the notch-tip coincides with the origin of the employed coordinate system. Since the local behaviour of the stresses and displacements at the notch-tip is of interest, it is not necessary to solve the complete underlying BVP. Instead, local solutions valid in the close vicinity surrounding the notch-tip (indicated by the zoom-in view) are considered within the asymptotic methodology. In order to determine these local solutions, the complex potential method is applied. Following Cherepanov (1979), the complex potentials are assumed to have the following form

$$\Phi_k^{(1)}(z) = \sum_i \left(A_{ki}^{(1)} z^{\lambda_i} + B_{ki}^{(1)} z^{\overline{\lambda}_i} \right), \qquad \Phi_k^{(2)}(z) = \sum_i \left(A_{ki}^{(2)} z^{\lambda_i} + B_{ki}^{(2)} z^{\overline{\lambda}_i} \right), \tag{3.2}$$

where the superscripts (1) and (2) indicate the corresponding material. The complex coefficients $A_{ki}^{(j)}$ and $B_{ki}^{(j)}$ as well as the exponents λ_i in Eq. (3.2) are calculated requiring that transmission (continuity) conditions along the material interface $\partial\Omega_\mathrm{I}$ as well as stress-free boundary conditions along the notch faces $\partial\Omega_\mathrm{N}$ are satisfied:

$$\left(\sigma_{\varphi\varphi}^{(1)} + \mathrm{i}\tau_{r\varphi}^{(1)} \right)_{\partial\Omega_\mathrm{I}} = \left(\sigma_{\varphi\varphi}^{(2)} + \mathrm{i}\tau_{r\varphi}^{(2)} \right)_{\partial\Omega_\mathrm{I}}, \tag{3.3}$$

$$\left(u_r^{(1)} + \mathrm{i}u_\varphi^{(1)}\right)_{\partial\Omega_\mathrm{I}} = \left(u_r^{(2)} + \mathrm{i}u_\varphi^{(2)}\right)_{\partial\Omega_\mathrm{I}}, \tag{3.4}$$

$$\left(\sigma_{\varphi\varphi}^{(1)} + \mathrm{i}\tau_{r\varphi}^{(1)}\right)_{\partial\Omega_\mathrm{N}} = 0, \tag{3.5}$$

$$\left(\sigma_{\varphi\varphi}^{(2)} + \mathrm{i}\tau_{r\varphi}^{(2)}\right)_{\partial\Omega_\mathrm{N}} = 0. \tag{3.6}$$

The set of Eqn. (3.3)-(3.6) represents the constraints characterising any admissible asymptotic solution at the notch-tip. Note that transmission conditions according to Eqn. (3.3)-(3.4) corresponds to a perfect bonding prohibiting any relative motion between both constitutes. Next, stresses and displacements are expressed through the complex potentials employing the Kolosov-Muskhelishvili formulae (2.45). The relations (3.3)-(3.6) together with their complex conjugates form a system of eight linear equations:

$$\mathbf{D}\underline{a}_i = 0, \quad \underline{a}_i = \left(A_{1i}^{(1)}, \overline{B}_{1i}^{(1)}, A_{2i}^{(1)}, \overline{B}_{2i}^{(1)}, A_{1i}^{(2)}, \overline{B}_{1i}^{(2)}, A_{2i}^{(2)}, \overline{B}_{2i}^{(2)}\right)^T, \quad \mathbf{D} \in \mathbb{C}^{8\mathrm{x}8}. \tag{3.7}$$

Non-trivial solutions exist only for a singular coefficient matrix $\mathbf{D}$ leading to the following characteristic equation:

$$\det[\mathbf{D}(\lambda)] = 0. \tag{3.8}$$

Solving Eq. (3.8) ultimately yields an infinite set of exponents $\{\lambda_1, \lambda_2, \ldots\}$ also denoted as eigenvalues. The characteristic equation (3.8) is generally non-linear and the exponents are calculated numerically either using the computer algebra system MATHEMATICA or the package for scientific computing NUMPY within a PYTHON environment. The associated vector $\underline{a}_i$, also denoted as eigenvector, contains the complex coefficients $A_{ij}^{(k)}$ as well as $B_{ij}^{(k)}$ and can be determined by computing the kernel of the matrix $\mathbf{D}(\lambda_i)$. Note that only boundary and transmission conditions in the vicinity of the notch-tip are taken into account within the asymptotic approach. This results in a non-unique solution covering all possible responses at the notch's vertex. This is also reflected by the fact, that the involved complex parameters $A_{ij}^{(k)}$ and $B_{ij}^{(k)}$ are determined up to a multiplicative constant that cannot be obtained using asymptotic analysis. After having computed the eigenvalues λ_i and the associated eigenvectors $\underline{a}_i$, the stress and displacement fields in the vicinity of the notch-tip can be expressed in form of a coordinate expansion with respect to the distance r ($j = 1, 2$):

$$\boldsymbol{\sigma}^{(j)}(r,\varphi) = \sum_{i=1}^{\infty} \left(K_i r^{\lambda_i - 1}\boldsymbol{\sigma}_i^{(j)}(\varphi) + \overline{K}_i r^{\overline{\lambda}_i - 1}\overline{\boldsymbol{\sigma}}_i^{(j)}(\varphi)\right), \tag{3.9}$$

$$\underline{u}^{(j)}(r,\varphi) = \sum_{i=1}^{\infty} \left(K_i r^{\lambda_i}\underline{u}_i^{(j)}(\varphi) + \overline{K}_i r^{\overline{\lambda}_i}\overline{\underline{u}}_i^{(j)}(\varphi)\right). \tag{3.10}$$

Note that Eqn. (3.9)-(3.10) hold in the most general case of complex exponents λ_i. The components $\left\{u_{r,i}^{(j)}, u_{\varphi,i}^{(j)}\right\}$ of the displacement eigenfunction $\underline{u}_i^{(j)}$ are given

by

$$\begin{aligned} u_{r,i}^{(j)}(\varphi) &= \frac{1}{4G}\Big((\kappa-\lambda_i)A_{1i}^{(j)}e^{\mathrm{i}\varphi(\lambda_i-1)} + (\kappa-\lambda_i)\overline{B}_{1i}^{(j)}e^{-\mathrm{i}\varphi(\lambda_i-1)} - A_{2i}^{(j)}e^{\mathrm{i}\varphi(\lambda_i+1)} \\ &\quad - \overline{B}_{2i}^{(j)}e^{-\mathrm{i}\varphi(\lambda_i+1)}\Big), \\ u_{\varphi,i}^{(j)}(\varphi) &= \frac{1}{4G\mathrm{i}}\Big((\kappa+\lambda_i)A_{1i}^{(j)}e^{\mathrm{i}\varphi(\lambda_i-1)} - (\kappa+\lambda_i)\overline{B}_{1i}^{(j)}e^{-\mathrm{i}\varphi(\lambda_i-1)} + A_{2i}^{(j)}e^{\mathrm{i}\varphi(\lambda_i+1)} \\ &\quad - \overline{B}_{2i}^{(j)}e^{-\mathrm{i}\varphi(\lambda_i+1)}\Big). \end{aligned} \tag{3.11}$$

The components $\left\{\sigma_{rr,i}^{(j)}, \sigma_{\varphi\varphi,i}^{(j)}, \tau_{r\varphi,i}^{(j)}\right\}$ of stress eigenfunctions $\boldsymbol{\sigma}_i^{(j)}$ can be written as

$$\begin{aligned} \sigma_{\varphi\varphi,i}^{(j)}(\varphi) &= \frac{\lambda_i}{2}\Big((1+\lambda_i)A_{1i}^{(j)}e^{\mathrm{i}\varphi(\lambda_i-1)} + (1+\lambda_i)\overline{B}_{1i}^{(j)}e^{-\mathrm{i}\varphi(\lambda_i-1)} + A_{2i}^{(j)}e^{\mathrm{i}\varphi(\lambda_i+1)} \\ &\quad + \overline{B}_{2i}^{(j)}e^{-\mathrm{i}\varphi(\lambda_i+1)}\Big), \\ \sigma_{rr,i}^{(j)}(\varphi) &= \frac{\lambda_i}{2}\Big((3-\lambda_i)A_{1i}^{(j)}e^{\mathrm{i}\varphi(\lambda_i-1)} + (3-\lambda_i)\overline{B}_{1i}^{(j)}e^{-\mathrm{i}\varphi(\lambda_i-1)} - A_{2i}^{(j)}e^{\mathrm{i}\varphi(\lambda_i+1)} \\ &\quad - \overline{B}_{2i}^{(j)}e^{-\mathrm{i}\varphi(\lambda_i+1)}\Big), \\ \tau_{r\varphi,i}^{(j)}(\varphi) &= \frac{\lambda_i}{2\mathrm{i}}\Big((\lambda_i-1)A_{1i}^{(j)}e^{\mathrm{i}\varphi(\lambda_i-1)} + (1-\lambda_i)\overline{B}_{1i}^{(j)}e^{-\mathrm{i}\varphi(\lambda_i-1)} + A_{2i}^{(j)}e^{\mathrm{i}\varphi(\lambda_i+1)} \\ &\quad - \overline{B}_{2i}^{(j)}e^{-\mathrm{i}\varphi(\lambda_i+1)}\Big). \end{aligned} \tag{3.12}$$

It should be noted that in case of complex exponents λ_i, the field variables possess an oscillatory character with respect to the radial direction:

$$r^{\lambda_i} = r^{\mathrm{Re}[\lambda_i]}e^{\mathrm{i}\,\mathrm{Im}[\lambda_i]\ln(r)} = r^{\mathrm{Re}[\lambda_i]}\left(\cos\left(\mathrm{Im}[\lambda_i]\ln(r)\right) + \mathrm{i}\sin\left(\mathrm{Im}[\lambda_i]\ln(r)\right)\right). \tag{3.13}$$

If $\mathrm{Re}[\lambda_i] < 1$, the associated stresses are singular at the notch-tip and such singularities are also denoted as oscillatory singularities (Suo, 1990).

3.3 One-term outer and inner expansion

Consider the butt-joint configuration as shown in Fig. 3.3(a) in its initial uncracked state prior to the fracture event. The corresponding domain Ω^0 is denoted as unperturbed domain and the elasticity problem defining the unperturbed solution $\underline{U}^0$ writes:

$$\begin{cases} \nabla \cdot \boldsymbol{\sigma}\left(\underline{U}^0\right) = 0 & \text{in} \quad \Omega^0 \\ \boldsymbol{\sigma}\left(\underline{U}^0\right) = \mathbb{C} : \nabla \underline{U}^0 & \text{in} \quad \Omega^0 \\ \boldsymbol{\sigma}\left(\underline{U}^0\right) \cdot \underline{n} = 0 & \text{along} \quad \partial\Omega^0 \setminus \partial\Omega_\sigma \\ \boldsymbol{\sigma}\left(\underline{U}^0\right) \cdot \underline{n} = \underline{t}^* & \text{along} \quad \partial\Omega_\sigma \\ + \text{ transmission conditions} \end{cases} \tag{3.14}$$

The cracked (perturbed) configuration is depicted in Fig. 3.3(b) and the associated domain $\Omega^{\Delta a}$ is denoted as perturbed domain. The function $\underline{U}^{\Delta a}$ is the solution of the

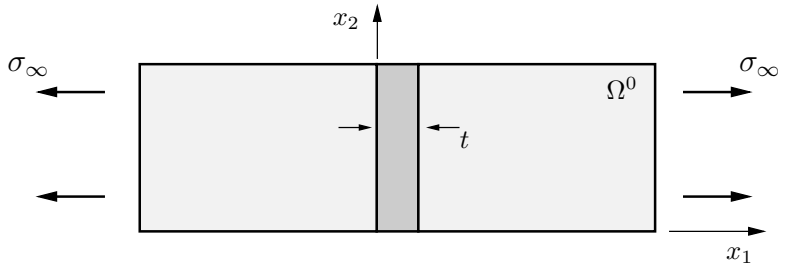

(a) Unperturbed outer domain Ω^0

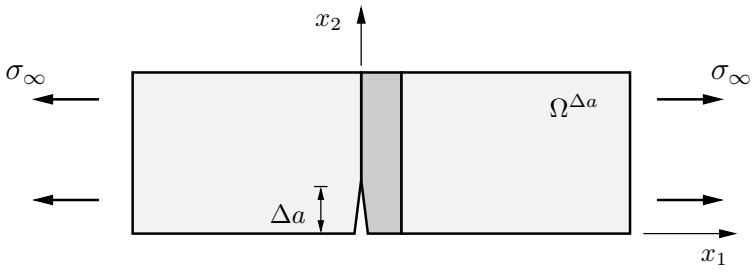

(b) Perturbed domain $\Omega^{\Delta a}$

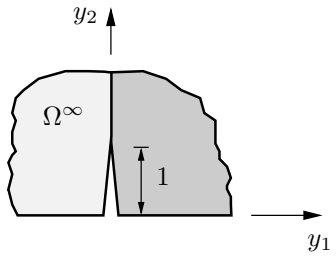

(c) Scaled inner domain Ω^∞ with dimensionless crack length equal to 1.

Figure 3.3: Sketch of outer domain Ω^0, the perturbed domain $\Omega^{\Delta a}$ and the inner domain Ω^∞, respectively.

perturbed problem:

$$\left\{\begin{array}{rcll} \nabla\cdot\boldsymbol{\sigma}\left(\underline{U}^{\Delta a}\right) &=& 0 & \text{in} \quad \Omega^{\Delta a} \\ \boldsymbol{\sigma}\left(\underline{U}^{\Delta a}\right) &=& \mathbb{C}:\nabla\underline{U}^{\Delta a} & \text{in} \quad \Omega^{\Delta a} \\ \boldsymbol{\sigma}\left(\underline{U}^{\Delta a}\right)\cdot\underline{n} &=& 0 & \text{along} \quad \partial\Omega^{\Delta a}\setminus\partial\Omega_\sigma \\ \boldsymbol{\sigma}\left(\underline{U}^{\Delta a}\right)\cdot\underline{n} &=& \underline{t}^* & \text{along} \quad \partial\Omega_\sigma \\ \quad + \text{transmission conditions} & & & \end{array}\right. \tag{3.15}$$

The presence of a crack results in a perturbation of the stress and displacement fields compared to the uncracked, unperturbed state. However, supposed that the crack length Δa is small compared to any characteristic length associated to Ω^0, e.g. the adhesive thickness t, stresses are only affected in a very small region close to the crack. Thus, there exists a so-called boundary layer region, where the presence of a crack significantly changes the field variables. With an increasing distance away from the crack, these perturbations eventually disappear. These observations ultimately lead to the concept of matched asymptotic expansions: The solution $\underline{U}^{\Delta a}$ of the perturbed problem is approximated using two asymptotic descriptions defined on different domains. One description is valid far away from the perturbation and the other captures the boundary layer effects close to the perturbation. The latter is the inner expansion defined on the scaled inner domain. The former is given by the outer expansion, which is formulated with respect to the outer domain where the crack is no longer visible. Consequently, the outer domain in fact coincides with the initial unperturbed domain Ω^0, cf. Fig. 3.3(a). The outer expansion represents an asymptotic expansion for $\Delta a \to 0$ with outer variables x_i fixed and is given by:

$$\begin{gathered} \underline{U}^{\Delta a}(r,\varphi) = \underline{U}^0(r,\varphi) + f_1(\Delta a)\underline{U}^1(r,\varphi) + f_2(\Delta a)\underline{U}^2(r,\varphi) + o(f_2(\Delta a)), \\ \text{with} \quad \lim_{\Delta a\to 0} f_1(\Delta a) = 0 \quad \text{and} \quad \lim_{\Delta a\to 0}\frac{f_2(\Delta a)}{f_1(\Delta a)} = 0. \end{gathered} \tag{3.16}$$

Equation (3.16) states, that for a fixed distance sufficiently far away from the crack, the perturbed solution $\underline{U}^{\Delta a}$ can be approximated by a series expansion composed of the unperturbed solution $\underline{U}^0$ forming the leading-order term and additional higher-order correction terms. All functions $\underline{U}^i$ in Eq. (3.16) are defined on the outer domain.

In order to obtain a solution representation in a region close to the perturbation, the perturbed domain containing the crack is stretched introducing the scaled inner coordinates $y_i = x_i/\Delta a$ and the associated radial coordinate $\rho = r/\Delta a$. In the auxiliary space of the stretched variables y_i, the perturbed domain $\Omega^{\Delta a}$ becomes the semi-infinite inner domain Ω^∞ which is unbounded in the asymptotic limit $\Delta a \to 0$. Due to this homothetic change of variables $x_i \to y_i$, the crack always has unit length in the inner domain Ω^∞ as shwon in Fig. 3.3(c). It is assumed, that the unknown exact solution $\underline{U}^{\Delta a}$ can be expanded with respect to the inner domain in form of an inner expansion, that is, an asymptotic expansion for $\Delta a \to 0$ with inner variables y_i

fixed:

$$\underline{U}^{\Delta a}(r,\varphi) = \underline{U}^{\Delta a}(\Delta a\rho,\varphi) = F_1(\Delta a)\underline{V}^1(\rho,\varphi) + F_2(\Delta a)\underline{V}^2(\rho,\varphi) + o(F_2(\Delta a)), \quad \text{with} \quad \lim_{\Delta a\to 0}\frac{F_2(\Delta a)}{F_1(\Delta a)}. \tag{3.17}$$

Here, the functions $\underline{V}^i$ are defined on the inner domain. The outer and inner expansions in Eqn. (3.16) and (3.17) describe the solution of the perturbed problem outside and inside the boundary layer region, respectively. Since both expansions approximate the same solution, but on different scales, there is a common intermediate region where inner and outer expansion are valid. This leads to the matching principle, stating that the inner behaviour of the outer expansions must match with the outer behaviour of the inner expansion (Van Dyke, 1964, Leguillon and Sanchez-Palencia, 1987, Kaplun, 1954, Lagerstrom and Cole, 1955). These matching conditions ultimately allow for a successive determination of the individual terms of the expansions.

Consider the leading-order term of the outer expansion $\underline{U}^0$. Since this term represents the solution of the unperturbed problem in Eq. (3.14) the solution $\underline{U}^0$ can be expanded in the vicinity of the notch as a coordinate expansion with respect to the radial coordinate r[13]:

$$\underline{U}^0(r,\varphi) \sim \underline{C} + K_1 r^{\lambda_1}\underline{u}_1(\varphi) \quad \text{as} \quad r\to 0. \tag{3.18}$$

The constant $\underline{C}$ represents a rigid body motion which is irrelevant and therefore omitted in the subsequent analysis. The BVP of the outer problem (3.14) is solved numerically using FEA. Having the numerical solution $\underline{U}^0_{\mathrm{FE}}$ at hand, the intensity factor K_1 is extracted using the path independent Ψ-integral:

$$K_1 = \frac{\Psi\left(\underline{U}^0_{\mathrm{FE}}, r^{-\lambda_1}\underline{u}_{-1}(\varphi)\right)}{\Psi\left(r^{\lambda_1}\underline{u}_1(\varphi), \eta^{-\lambda_1}\underline{u}_{-1}(\varphi)\right)}. \tag{3.19}$$

To continue, let us consider the leading-order term of the inner expansion (3.17) defined on the unbounded inner domain Ω^∞. Based on the perturbed problem (3.15) and the inner expansion (3.17), the following BVP can be deduced for $\underline{V}^1$:

$$\left\{\begin{array}{rcll} \nabla_y\cdot\boldsymbol{\sigma}_y\left(\underline{V}^1\right) &=& 0 & \text{in} \quad \Omega^\infty \\ \boldsymbol{\sigma}_y\left(\underline{V}^1\right) &=& \mathbb{C}:\nabla_y\underline{V}^1 & \text{in} \quad \Omega^\infty \\ \boldsymbol{\sigma}_y\left(\underline{V}^1\right)\cdot\underline{n} &=& 0 & \text{along} \quad \partial\Omega^\infty\setminus\partial\Omega_\sigma \\ + \text{ transmission conditions} & & & \end{array}\right. \tag{3.20}$$

Note that the change of variables during scaling implies the following relations:

$$\nabla_y(\cdot) = \nabla(\cdot)\Delta a, \qquad \boldsymbol{\sigma}_y = \boldsymbol{\sigma}\Delta a, \qquad \boldsymbol{\varepsilon}_y = \boldsymbol{\varepsilon}\Delta a. \tag{3.21}$$

[13] In order to avoid cumbersome notation, the eigenfunctions $\underline{u}_i(\varphi)$ and $\boldsymbol{\sigma}_i(\varphi)$ are not equipped with superscripts (1) and (2) for the different materials.

The statement of the inner problem according to Eq. (3.20), however, is incomplete since boundary conditions at infinity are missing. This is not surprising since no connection between inner and outer expansion has been considered so far. Since both expansion are approximations of the same solution a zone of overlapping is supposed where inner and outer expansion give the same result. This is expressed by the matching principle establishing a relation between both expansions. The matching principle has been formulated by Van Dyke (1964) as follows: the one-term inner expansion of the one-term outer expansion should match with the one-term outer expansion of the one-term inner expansion. In other words, the near field of the outer expansion ($r \to 0$) should match with the far-field of the inner expansion ($\rho \to \infty$). The one-term inner expansion of the one-term outer expansion is obtained by rewriting the function $\underline{U}^0$ in inner coordinates and expand for small Δa with inner variables fixed:

$$\underline{U}^{\Delta a} \sim K_1 \rho^{\lambda_1} \Delta a^{\lambda_1} \underline{u}_1(\varphi) \quad \text{as} \quad \Delta a \to 0. \tag{3.22}$$

The counterpart, the outer expansion of the inner expansion is constructed by rewriting Eq. (3.17) in outer coordinates and expand for small Δa with outer variables fixed:

$$\underline{U}^{\Delta a} \sim F_1(\Delta a) \underline{V}^1 \left(\frac{r}{\Delta a}, \varphi \right) \quad \text{as} \quad \Delta a \to 0. \tag{3.23}$$

Equating the relations (3.23) and (3.22) according to the matching principle determines the function F_1 and characterises the outer behaviour of $\underline{V}^1$:

$$F_1(\Delta a) = K_1 \Delta a^{\lambda_1}, \tag{3.24a}$$

$$\underline{V}^1(\rho, \varphi) \sim \rho^{\lambda_1} \underline{u}_1(\varphi) \quad \text{as} \quad \rho \to \infty. \tag{3.24b}$$

Following the notation of Van Dyke (1964), it is convenient to systematise the matching procedure as follows:

1-term outer expansion :	$\underline{U}^{\Delta a} \sim \underline{U}^0(r, \varphi)$	(3.25a)
rewritten in inner variables :	$= \underline{U}^0(\rho\, \Delta a, \varphi)$	(3.25b)
expanded for small Δa :	$= K_1 \Delta a^{\lambda_1} \rho^{\lambda_1} \underline{u}_1 + \ldots$	(3.25c)
1-term inner expansion :	$= K_1 \Delta a^{\lambda_1} \rho^{\lambda_1} \underline{u}_1$	(3.25d)

1-term inner expansion :	$\underline{U}^{\Delta a} \sim F_1(\Delta a) \underline{V}^1(\rho, \varphi)$	(3.26a)
rewritten in outer variables		
and expanded for small Δa :	$= F_1(\Delta a) \underline{V}^1 \left(\frac{r}{\Delta a}, \varphi \right) + \ldots$	(3.26b)
1-term outer expansion :	$= F_1(\Delta a) \underline{V}^1 \left(\frac{r}{\Delta a}, \varphi \right)$	(3.26c)

The matching principle demands to equate (3.25d) and (3.26c) yielding the same result as in Eq. (3.24). The matching principle defines the behaviour of the function $\underline{V}^1$ at infinity

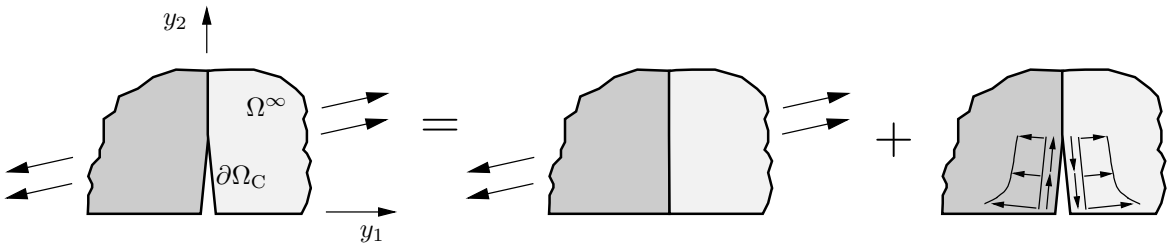

Figure 3.4: Superposition principle: the situation to the far left is equivalent to the superposition of the problem in the middle representing the uncracked configuration and the situation to the far right with appropriate boundary conditions applied along the crack faces $\partial\Omega_C$.

and thus specifies the missing boundary condition of the BVP (3.20). From a physical point of view, Eq. (3.24b) means that far away from the perturbation, the function $\underline{V}^1$ approaches the near-tip fields associated to the unperturbed problem. However, as the dimensionless radius ρ tends to infinity, the prescribed displacements also tend to infinity. From a mathematical point of view, this implies a solution with unbounded energy and thus represents an ill-posed problem in the sense of Lax-Milgram framework (Leguillon and Sanchez-Palencia, 1987). Therefore, Eq. (3.24b) is reformulated using the superposition principle illustrated in Fig. 3.4:

$$\underline{V}^1(\rho,\varphi) = \rho^{\lambda_1}\underline{u}_1(\varphi) + \hat{\underline{V}}_1(\rho,\varphi) \quad \text{with} \quad \lim_{\rho\to\infty} \hat{\underline{V}}_1(\rho,\varphi) = 0. \tag{3.27}$$

The function $\underline{V}^1$ is composed of a first part $\rho^{\lambda_1}\underline{u}_1$ related to the unperturbed problem and a second part $\hat{\underline{V}}_1$ representing the perturbations due to the existence of a small crack. Substituting Eq. (3.27) in Eq. (3.20) yields a well-posed problem with a uniquely defined solution $\hat{\underline{V}}_1$:

$$\left\{\begin{array}{rcll} \nabla_y \cdot \boldsymbol{\sigma}_y\left(\hat{\underline{V}}_1\right) & = & 0 & \text{in} \quad \Omega^\infty \\ \boldsymbol{\sigma}_y\left(\hat{\underline{V}}_1\right) & = & \mathbb{C} : \nabla_y \hat{\underline{V}}_1 & \text{in} \quad \Omega^\infty \\ \boldsymbol{\sigma}_y\left(\hat{\underline{V}}_1\right)\cdot \underline{n} & = & 0 & \text{along} \quad \partial\Omega^\infty \setminus \partial\Omega_C \\ \boldsymbol{\sigma}_y\left(\hat{\underline{V}}_1\right)\cdot \underline{n} & = & -\boldsymbol{\sigma}_y\left(\rho^{\lambda_1}\underline{u}_1(\varphi)\right)\cdot \underline{n} & \text{along} \quad \partial\Omega_C \\ \hat{\underline{V}}_1(\rho,\varphi) & \to & 0 & \text{as} \quad \rho\to\infty \\ + \text{ transmission conditions} & & & \end{array}\right. \tag{3.28}$$

Note that the superposition principle implies tractions on the crack faces $\partial\Omega_C$ as shown in Fig. 3.4. Finally, the one-term inner expansion writes

$$\underline{U}^{\Delta a} = K_1 \Delta a^{\lambda_1}\left(\rho^{\lambda_1}\underline{u}_1(\varphi) + \hat{\underline{V}}_1(\rho,\varphi)\right) + o\left(\Delta a^{\lambda_1}\right). \tag{3.29}$$

Based on the previously obtained inner and outer expansions, asymptotic relations for the IERR can be derived. For this purpose, the path independent Ψ-integral introduced in Eq. (2.43) is employed allowing for the computation of the change in potential energy

due to the onset of a crack:

$$\Delta\Pi = \frac{d}{2}\int_{\gamma}\left(\boldsymbol{\sigma}\left(\underline{U}^{\Delta a}\right)\cdot\underline{n}\cdot\underline{U}^{0} - \boldsymbol{\sigma}\left(\underline{U}^{0}\right)\cdot\underline{n}\cdot\underline{U}^{\Delta a}\right)\mathrm{d}s. \tag{3.30}$$

Again, integration must be performed in a counter-clockwise sense and the integral can either be computed in the physical space characterised by the coordinates x_i or with respect to the scaled inner variables y_i. Choosing the latter and employing the transformation relations according Eq. (3.21), it follows

$$\Delta\Pi = \frac{d}{2}\int_{\gamma}\left(\boldsymbol{\sigma}_y\left(\underline{U}^{\Delta a}\right)\cdot\underline{n}\cdot\underline{U}^{0} - \boldsymbol{\sigma}_y\left(\underline{U}^{0}\right)\cdot\underline{n}\cdot\underline{U}^{\Delta a}\right)\mathrm{d}s_y = \Psi\left(\underline{U}^{\Delta a},\underline{U}^{0}\right)d. \tag{3.31}$$

The previously obtained inner and outer expansions are now substituted in Eq. (3.31) to derive the leading-order term of the asymptotic expansion of the IERR. Evaluating all quantities with respect to the inner domain and exploiting the bi-linearity of $\Psi(\cdot,\cdot)$ yields:

$$\Psi\left(\underline{U}^{\Delta a},\underline{U}^{0}\right) = \Psi\left(K_1\Delta a^{\lambda_1}\left(\rho^{\lambda_1}\underline{u}_1(\varphi) + \hat{\underline{V}}_1(\rho,\varphi)\right), K_1\Delta a^{\lambda_1}\rho^{\lambda_1}\underline{u}_1(\varphi)\right) + \ldots \tag{3.32}$$

The change of potential energy writes:

$$\Delta\Pi = dK_1^2\Delta a^{2\lambda_1}\Psi\left(\hat{\underline{V}}_1,\rho^{\lambda_1}\underline{u}_1\right) + o\left(\Delta a^{2\lambda_1}\right). \tag{3.33}$$

Relating the change of potential energy to the area $d\Delta a$ of the initiated crack finally yields the leading-order term of the expansion of the IERR $\bar{\mathcal{G}}$:

$$\bar{\mathcal{G}} = K_1^2\Delta a^{2\lambda_1-1}\Psi_{11} + o\left(\Delta a^{2\lambda_1-1}\right), \tag{3.34}$$

with

$$\Psi_{11} = \Psi\left(\rho^{\lambda_1}\underline{u}_1,\hat{\underline{V}}_1\right) = -\Psi\left(\hat{\underline{V}}_1,\rho^{\lambda_1}\underline{u}_1\right). \tag{3.35}$$

In particular, Eq. (3.34) shows that the IERR vanishes for $\Delta a \to 0$ in case of a weak stress singularity ($\lambda_1 > 1/2$) and on account of Eq. (2.75), it follows that the ERR vanishes, too.

3.4 Complex higher-order terms

To proceed with high-order terms, the starting point is to consider additional higher-order terms in the coordinate expansion of $\underline{U}^0$. Subsequently, corresponding terms of the inner expansion are derived. In case of higher-order terms, the corresponding intensity factors K_i and associated exponents λ_i are typically complex requiring special attention. Without loss of generality, let us consider the following expansion of $\underline{U}^0$ with a real first-order term and complex second-order terms:

$$\underline{U}^0(r,\varphi) = K_1 r^{\lambda_1}\underline{u}_1(\varphi) + K_2 r^{\lambda_2}\underline{u}_2(\varphi) + \overline{K}_2 r^{\overline{\lambda}_2}\overline{\underline{u}}_2(\varphi) + o(r^{\mathrm{Re}[\lambda_2]}), \quad \text{as} \quad r \to 0. \tag{3.36}$$

The complex terms $r^{\lambda_2}\underline{u}_2$ and $r^{\overline{\lambda}_2}\overline{\underline{u}}_2$ in Eq. (3.36) always appear in associated complex conjugated pairs. Hence, their linear combination yields a real valued physical quantity which becomes clear when rewriting Eq. (3.36) equivalently as:

$$\underline{U}^0(r,\varphi) = K_1 r^{\lambda_1}\underline{u}_1(\varphi) + 2\mathrm{Re}\left[K_2 r^{\lambda_2}\underline{u}_2(\varphi)\right] + o(r^{\mathrm{Re}[\lambda_2]}), \quad \text{as} \quad r \to 0. \tag{3.37}$$

Despite the complex nature of the GSIF's, the extraction procedure employing the Ψ-integral can be used analogously to the real case:

$$K_2 = \frac{\Psi\left(\underline{U}^0_{\mathrm{FE}}, r^{-\lambda_2}\underline{u}_{-2}(\varphi)\right)}{\Psi\left(r^{\lambda_2}\underline{u}_2(\varphi), r^{-\lambda_2}\underline{u}_{-2}(\varphi)\right)}. \tag{3.38}$$

Having the outer expansion at hand, the systematic matching procedure is carried out again. This allows for obtaining the additional second-order terms of the inner expansion. Based on the outer expansion in Eq. (3.36) it follows:

$$\begin{aligned}
&\textit{1-term outer expansion}: && \underline{U}^{\Delta a} \sim \underline{U}^0(r,\varphi) && \text{(3.39a)}\\
&\quad\text{rewritten in inner variables}: && = \underline{U}^0(\rho\,\Delta a,\varphi) && \text{(3.39b)}\\
&\quad\text{expanded for small } \Delta a: && = K_1\Delta a^{\lambda_1}\rho^{\lambda_1}\underline{u}_1 + \ldots && \text{(3.39c)}\\
&\quad\text{2-term inner expansion}: && = K_1\Delta a^{\lambda_1}\rho^{\lambda_1}\underline{u}_1 + K_2\Delta a^{\lambda_2}\rho^{\lambda_2}\underline{u}_2 && \\
& && \quad + \overline{K}_2\Delta a^{\overline{\lambda}_2}\rho^{\overline{\lambda}_2}\overline{\underline{u}}_2 && \text{(3.39d)}
\end{aligned}$$

$$\begin{aligned}
&\textit{2-term inner expansion}: && \underline{U}^{\Delta a} \sim F_1(\Delta a)\underline{V}^1(\rho,\varphi) + F_2(\Delta a)\underline{V}^2(\rho,\varphi) && \text{(3.40a)}\\
&\quad\text{rewritten in outer variables} && && \\
&\quad\text{and expanded for small } \Delta a: && = F_1(\Delta a)\underline{V}^1\left(\frac{r}{\Delta a},\varphi\right) + \ldots && \text{(3.40b)}\\
&\quad\text{2-term outer expansion}: && = F_1(\Delta a)\underline{V}^1\left(\frac{r}{\Delta a},\varphi\right) + F_2(\Delta a)\underline{V}^2\left(\frac{r}{\Delta a},\varphi\right) && \\
& && \quad + F_3(\Delta a)\underline{V}^3\left(\frac{r}{\Delta a},\varphi\right) && \text{(3.40c)}
\end{aligned}$$

Equating Eq. (3.39d) and Eq. (3.40c) according to the matching principle yields

$$F_2(\Delta a) = K_2\Delta a^{\lambda_2}, \tag{3.41a}$$
$$\underline{V}^2(\rho,\varphi) \sim \rho^{\lambda_2}\underline{u}_2(\varphi) \quad \text{as} \quad \rho \to \infty, \tag{3.41b}$$

and

$$F_3(\Delta a) = \overline{K}_2\Delta a^{\overline{\lambda}_2}, \tag{3.42a}$$
$$\underline{V}^3(\rho,\varphi) \sim \rho^{\overline{\lambda}_2}\overline{\underline{u}}_2(\varphi) \quad \text{as} \quad \rho \to \infty. \tag{3.42b}$$

Again, a superposition principle is employed to ensure well-posed problems. Based on Eq. (3.41b) and (3.42b), this yields:

$$\underline{V}^2(\rho,\varphi) = \rho^{\lambda_2}\underline{u}_2(\varphi) + \hat{\underline{V}}_2(\rho,\varphi), \tag{3.43}$$

$$\underline{V}^3(\rho,\varphi) = \rho^{\overline{\lambda}_2}\overline{\underline{u}}_2(\varphi) + \overline{\hat{\underline{V}}}_2(\rho,\varphi). \tag{3.44}$$

The functions $\hat{\underline{V}}_2$ and $\overline{\hat{\underline{V}}}_2$ vanish at infinity and are calculated using FEA. Since both functions are complex, however, they have to be divided into a real and an imaginary part to allow for a computation employing the commercial finite element software Abaqus. With $\hat{\underline{V}}_2 = \hat{\underline{V}}_{2,\mathrm{Re}} + \mathrm{i}\hat{\underline{V}}_{2,\mathrm{Im}}$, two BVPs have to be solved for the real and the imaginary part, respectively:

$$\left\{\begin{array}{rcll} \nabla_y \cdot \boldsymbol{\sigma}_y\left(\hat{\underline{V}}_{2,\mathrm{Re}}\right) &=& 0 & \text{in} \quad \Omega^\infty \\ \boldsymbol{\sigma}_y\left(\hat{\underline{V}}_{2,\mathrm{Re}}\right) &=& \mathbb{C} : \nabla_y \hat{\underline{V}}_{2,\mathrm{Re}} & \text{in} \quad \Omega^\infty \\ \boldsymbol{\sigma}_y\left(\hat{\underline{V}}_{2,\mathrm{Re}}\right)\cdot\underline{n} &=& 0 & \text{along} \quad \partial\Omega^\infty \setminus \partial\Omega_\mathrm{C} \\ \boldsymbol{\sigma}_y\left(\hat{\underline{V}}_{2,\mathrm{Re}}\right)\cdot\underline{n} &=& -\boldsymbol{\sigma}_y\left(\mathrm{Re}\left[\rho^{\lambda_2}\underline{u}_2(\varphi)\right]\right)\cdot\underline{n} & \text{along} \quad \partial\Omega_\mathrm{C} \\ \hat{\underline{V}}_{2,\mathrm{Re}}(\rho,\varphi) &\to& 0 & \text{as} \quad \rho\to\infty \\ + \text{ transmission conditions,} & & & \end{array}\right. \tag{3.45}$$

and

$$\left\{\begin{array}{rcll} \nabla_y \cdot \boldsymbol{\sigma}_y\left(\hat{\underline{V}}_{2,\mathrm{Im}}\right) &=& 0 & \text{in} \quad \Omega^\infty \\ \boldsymbol{\sigma}_y\left(\hat{\underline{V}}_{2,\mathrm{Im}}\right) &=& \mathbb{C} : \nabla_y \hat{\underline{V}}_{2,\mathrm{Im}} & \text{in} \quad \Omega^\infty \\ \boldsymbol{\sigma}_y\left(\hat{\underline{V}}_{2,\mathrm{Im}}\right)\cdot\underline{n} &=& 0 & \text{along} \quad \partial\Omega^\infty \setminus \partial\Omega_\mathrm{C} \\ \boldsymbol{\sigma}_y\left(\hat{\underline{V}}_{2,\mathrm{Im}}\right)\cdot\underline{n} &=& -\boldsymbol{\sigma}_y\left(\mathrm{Im}\left[\rho^{\lambda_2}\underline{u}_2(\varphi)\right]\right)\cdot\underline{n} & \text{along} \quad \partial\Omega_\mathrm{C} \\ \hat{\underline{V}}_{2,\mathrm{Im}}(\rho,\varphi) &\to& 0 & \text{as} \quad \rho\to\infty \\ + \text{ transmission conditions.} & & & \end{array}\right. \tag{3.46}$$

Ultimately, the two-term inner expansion takes the form:

$$\begin{aligned} \underline{U}^{\Delta a} = {} & K_1 \Delta a^{\lambda_1}\left(\rho^{\lambda_1}\underline{u}_1(\varphi) + \hat{\underline{V}}_1(\rho,\varphi)\right) + K_2\Delta a^{\lambda_2}\left(\rho^{\lambda_2}\underline{u}_2(\varphi) + \hat{\underline{V}}_2(\rho,\varphi)\right) \\ & + \overline{K}_2\Delta a^{\overline{\lambda}_2}\left(\rho^{\overline{\lambda}_2}\overline{\underline{u}}_2(\varphi) + \overline{\hat{\underline{V}}}_2(\rho,\varphi)\right) + o\left(\Delta a^{\lambda_2}\right). \end{aligned} \tag{3.47}$$

This matching process can be further continued to gradually obtain higher inner terms. However, attention has to be paid on the higher-order correction term $f_1(\Delta a)\underline{U}_1(r,\varphi)$ within the outer expansion which also affects the inner expansion and has to be incorporated correctly, cf. Section 3.5.

Based on the extended series expansions, an asymptotic expansion of the IERR containing higher-order terms is derived. To this end, the unperturbed solution $\underline{U}^0$ and the two-term inner expansion in Eq. (3.47) are substituted in Eq. (3.31). Using the bi-linearity of the Ψ-integral the change in potential energy per thickness d

reads:

$$\begin{aligned}\frac{\Delta\Pi}{d} = \Psi\left(\underline{U}^{\Delta a}, \underline{U}^{0}\right) &= K_1^2 \Delta a^{2\lambda_1}\, \Psi\left(\rho^{\lambda_1}\underline{u}_1(\varphi) + \underline{\hat{V}}_1(\rho,\varphi), \rho^{\lambda_1}\underline{u}_1(\varphi)\right) \\ &+ K_1 K_2 \Delta a^{\lambda_1+\lambda_2}\, \Psi\left(\rho^{\lambda_1}\underline{u}_1(\varphi) + \underline{\hat{V}}_1(\rho,\varphi), \rho^{\lambda_2}\underline{u}_2(\varphi)\right) \\ &+ K_1 \overline{K}_2 \Delta a^{\lambda_1+\bar{\lambda}_2}\, \Psi\left(\rho^{\lambda_1}\underline{u}_1(\varphi) + \underline{\hat{V}}_1(\rho,\varphi), \rho^{\bar{\lambda}_2}\overline{\underline{u}}_2(\varphi)\right) \\ &+ K_2 K_1 \Delta a^{\lambda_1+\lambda_2}\, \Psi\left(\rho^{\lambda_2}\underline{u}_2(\varphi) + \underline{\hat{V}}_2(\rho,\varphi), \rho^{\lambda_1}\underline{u}_1(\varphi)\right) \\ &+ K_2^2 \Delta a^{2\lambda_2}\, \Psi\left(\rho^{\lambda_2}\underline{u}_2(\varphi) + \underline{\hat{V}}_2(\rho,\varphi), \rho^{\lambda_2}\underline{u}_2(\varphi)\right) \\ &+ K_2 \overline{K}_2 \Delta a^{\lambda_2+\bar{\lambda}_2}\, \Psi\left(\rho^{\lambda_2}\underline{u}_2(\varphi) + \underline{\hat{V}}_2(\rho,\varphi), \rho^{\bar{\lambda}_2}\overline{\underline{u}}_2(\varphi)\right) \\ &+ \overline{K}_2 K_1 \Delta a^{\lambda_1+\bar{\lambda}_2}\, \Psi\left(\rho^{\bar{\lambda}_2}\overline{\underline{u}}_2(\varphi) + \overline{\underline{\hat{V}}}_2(\rho,\varphi), \rho^{\lambda_1}\underline{u}_1(\varphi)\right) \\ &+ \overline{K}_2 K_2 \Delta a^{\lambda_2+\bar{\lambda}_2}\, \Psi\left(\rho^{\bar{\lambda}_2}\overline{\underline{u}}_2(\varphi) + \overline{\underline{\hat{V}}}_2(\rho,\varphi), \rho^{\lambda_2}\underline{u}_2(\varphi)\right) \\ &+ \overline{K}_2^2 \Delta a^{2\bar{\lambda}_2}\, \Psi\left(\rho^{\bar{\lambda}_2}\overline{\underline{u}}_2(\varphi) + \overline{\underline{\hat{V}}}_2(\rho,\varphi), \rho^{\bar{\lambda}_2}\overline{\underline{u}}_2(\varphi)\right) + \dots \end{aligned} \tag{3.48}$$

This relation can be further simplified employing the bi-orthogonality property of the Ψ-integral according to Eq. (2.61) which yields

$$\begin{aligned}-\Psi\left(\underline{U}^{\Delta a}, \underline{U}^{0}\right) &= K_1^2 \Delta a^{2\lambda_1} \Psi_{11} + 2\mathrm{Re}\left[K_1 K_2 \left(\Psi_{12} + \Psi_{21}\right) \Delta a^{\lambda_1+\lambda_2}\right] \\ &+ \left(K_2 \overline{K}_2 \Psi_{22} + 2\mathrm{Re}\left[K_2^2 \Delta a^{2\mathrm{i}\,\mathrm{Im}[\lambda_2]} \Psi_{33}\right]\right) \Delta a^{2\mathrm{Re}[\lambda_2]} + o\left(\Delta a^{2\mathrm{Re}[\lambda_2]}\right), \end{aligned} \tag{3.49}$$

with the quantities

$$\begin{aligned} &\Psi_{11} = \Psi\left(\rho^{\lambda_1}\underline{u}_1, \underline{\hat{V}}_1\right), \\ &\Psi_{12} = \Psi\left(\rho^{\lambda_1}\underline{u}_1(\varphi), \underline{\hat{V}}_2(\rho,\varphi)\right), \qquad \Psi_{21} = \Psi\left(\rho^{\lambda_2}\underline{u}_2(\varphi), \underline{\hat{V}}_1(\rho,\varphi)\right), \\ &\Psi_{22} = 2\mathrm{Re}\left[\Psi\left(\rho^{\bar{\lambda}_2}\overline{\underline{u}}_2(\varphi), \underline{\hat{V}}_2(\rho,\varphi)\right)\right], \quad \Psi_{33} = \Psi\left(\rho^{\lambda_2}\underline{u}_2(\varphi), \underline{\hat{V}}_2(\rho,\varphi)\right). \end{aligned} \tag{3.50}$$

Relating the change of potential energy to the crack surface $d\Delta a$ finally yields the desired extended expansion of the IERR:

$$\begin{aligned}\bar{\mathcal{G}} = \frac{\Delta\Pi}{d\Delta a} &= K_1^2 \Delta a^{2\lambda_1-1} \Psi_{11} + 2\mathrm{Re}\left[K_1 K_2 \left(\Psi_{12} + \Psi_{21}\right) \Delta a^{\lambda_1+\lambda_2-1}\right] \\ &+ \left(K_2 \overline{K}_2 \Psi_{22} + 2\mathrm{Re}\left[K_2^2 \Delta a^{2\mathrm{i}\,\mathrm{Im}[\lambda_2]} \Psi_{33}\right]\right) \Delta a^{2\mathrm{Re}[\lambda_2]-1} + o\left(\Delta a^{2\mathrm{Re}[\lambda_2]-1}\right). \end{aligned} \tag{3.51}$$

The coefficients Ψ_{12} and Ψ_{21} possess an interesting and very practical symmetry property, which will be used in the forthcoming sections. Although this property has been numerically observed in literature, a rigorous proof is still missing and will be deduced in the following. According to the definition of the Ψ-integral in Eq. (2.44), the coefficients Ψ_{12} and Ψ_{21} write, respectively:

$$\Psi_{21} = -\frac{1}{2}\int_\gamma \left(\boldsymbol{\sigma}_y\left(\underline{\hat{V}}_1\right)\cdot\underline{n}\cdot\rho^{\lambda_2}\underline{u}_2(\varphi) - \boldsymbol{\sigma}_y\left(\rho^{\lambda_2}\underline{u}_2(\varphi)\right)\cdot\underline{n}\cdot\underline{\hat{V}}_1\right)\mathrm{d}s_y, \tag{3.52}$$

$$\Psi_{12} = -\frac{1}{2}\int_\gamma \left(\boldsymbol{\sigma}_y\left(\underline{\hat{V}}_2\right)\cdot\underline{n}\cdot\rho^{\lambda_1}\underline{u}_1(\varphi) - \boldsymbol{\sigma}_y\left(\rho^{\lambda_1}\underline{u}_1(\varphi)\right)\cdot\underline{n}\cdot\underline{\hat{V}}_2\right)\mathrm{d}s_y. \tag{3.53}$$

Since the contour γ can be chosen arbitrarily, let us chose the crack contour γ_c itself as contour. Invoking the boundary conditions associated to $\underline{\hat{V}}_1$ and $\underline{\hat{V}}_2$ according to Eqn. (3.28), (3.45) and (3.46) it follows:

$$\Psi_{21} = \frac{1}{2}\int_{\gamma_c} \left(\boldsymbol{\sigma}_y\left(\rho^{\lambda_1}\underline{u}_1(\varphi)\right)\cdot\underline{n}\cdot\rho^{\lambda_2}\underline{u}_2(\varphi) - \boldsymbol{\sigma}_y\left(\underline{\hat{V}}_2\right)\cdot\underline{n}\cdot\underline{\hat{V}}_1\right)\mathrm{d}s_y, \tag{3.54}$$

$$\Psi_{12} = \frac{1}{2}\int_{\gamma_c} \left(\boldsymbol{\sigma}_y\left(\rho^{\lambda_2}\underline{u}_2(\varphi)\right)\cdot\underline{n}\cdot\rho^{\lambda_1}\underline{u}_1(\varphi) - \boldsymbol{\sigma}_y\left(\underline{\hat{V}}_1\right)\cdot\underline{n}\cdot\underline{\hat{V}}_2\right)\mathrm{d}s_y. \tag{3.55}$$

The eigensolutions $r^{\lambda_1}\underline{u}_1(\varphi)$ and $r^{\lambda_2}\underline{u}_2(\varphi)$ define the notch-tip field of the uncracked state. Thus, the displacements and stresses associated to these solutions are continuous across γ_c. This implies:

$$\int_{\gamma_c} \boldsymbol{\sigma}_y\left(\rho^{\lambda_1}\underline{u}_1(\varphi)\right)\cdot\underline{n}\cdot\rho^{\lambda_2}\underline{u}_2(\varphi)\mathrm{d}s_y = 0, \tag{3.56}$$

$$\int_{\gamma_c} \boldsymbol{\sigma}_y\left(\rho^{\lambda_2}\underline{u}_2(\varphi)\right)\cdot\underline{n}\cdot\rho^{\lambda_1}\underline{u}_1(\varphi)\mathrm{d}s_y = 0. \tag{3.57}$$

Using these identities and subtraction of Eq. (3.55) from (3.54) leads to:

$$\Psi_{21} - \Psi_{12} = \frac{1}{2}\int_{\gamma_c} \left(\boldsymbol{\sigma}_y\left(\underline{\hat{V}}_1\right)\cdot\underline{n}\cdot\underline{\hat{V}}_2 - \boldsymbol{\sigma}_y\left(\underline{\hat{V}}_2\right)\cdot\underline{n}\cdot\underline{\hat{V}}_1\right)\mathrm{d}s_y. \tag{3.58}$$

Invoking Betti's theorem, the right-hand side of Eq. (3.58) vanishes which eventually proves the desired symmetry relation:

$$\Psi_{21} = \Psi_{12}. \tag{3.59}$$

Using this symmetry property, the expansion of the IERR takes the form:

$$\begin{aligned}\bar{\mathcal{G}} = {} & K_1^2\Delta a^{2\lambda_1-1}\Psi_{11} + 4\mathrm{Re}\left[K_1K_2\Psi_{12}\Delta a^{\lambda_1+\lambda_2-1}\right] \\ & + \left(K_2\overline{K}_2\Psi_{22} + 2\mathrm{Re}\left[K_2^2\Delta a^{2\mathrm{i}\,\mathrm{Im}[\lambda_2]}\Psi_{33}\right]\right)\Delta a^{2\mathrm{Re}[\lambda_2]-1} + o\left(\Delta a^{2\mathrm{Re}[\lambda_2]-1}\right).\end{aligned} \tag{3.60}$$

3.5 Higher-order interaction between inner and outer expansion

So far, the individual terms of the inner expansion have been derived based on the leading-order term $\underline{U}^0$ of the outer expansion and the matching conditions. Conversely, the terms of the inner expansion affect the higher-order correction term $f_1(\Delta a)\underline{U}^1(r,\varphi)$ of the outer expansion as illustrated in Fig. 3.5. These higher-order terms in turn affect the inner expansion and so on. This consecutive interaction between inner and outer expansion is briefly outlined below, and the insights gained are of general importance, especially for the asymptotic expansions derived in Section 5.

In order to define the higher-order correction term $f_1(\Delta a)\underline{U}^1(r,\varphi)$ in the outer expansion the matching process described in the previous section is essentially reversed: the inner expansion is rewritten in outer coordinates and subsequently expanded for small Δa

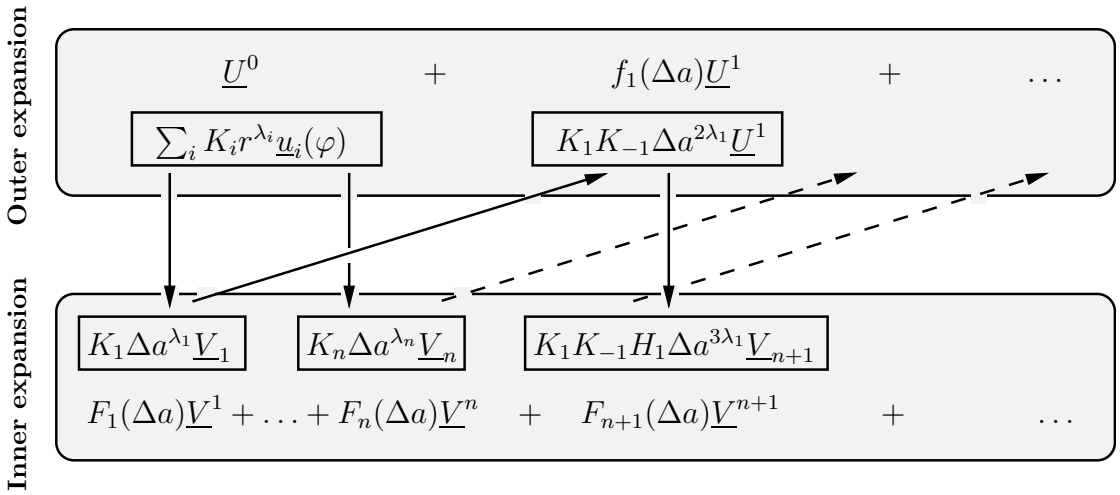

Figure 3.5: Interrelation between terms of outer and inner expansion.

with outer variable r fixed:

$$\underline{U}^{\Delta a}(r,\varphi) \sim K_1\Delta a^{\lambda_1}\left(\left(\frac{r}{\Delta a}\right)^{\lambda_1}\underline{u}_1(\varphi) + \hat{\underline{V}}_1\left(\frac{r}{\Delta a},\varphi\right)\right) \quad \text{as} \quad \Delta a \to 0. \tag{3.61}$$

Hence, the behaviour of $\hat{\underline{V}}_1$ at infinity has to be investigated in order to further proceed with the successive matching process. According to Eq. (3.28), the solution $\hat{\underline{V}}_1$ vanishes at infinity and at the same time satisfies stress-free boundary conditions at the notch faces $\partial\Omega_{\mathrm{N}}$. Analogous to the coordinate expansion of $\underline{U}^0$ in the vicinity of the notch, cf. Eq. (3.18), there is a corresponding coordinate expansion of $\hat{\underline{V}}_1$ at infinity employing the dual exponents and associated dual eigenfunctions:

$$\hat{\underline{V}}_1(\rho,\varphi) \sim \sum_{k=1}^{N} K_{-k}\rho^{-\lambda_k}\underline{u}_{-k}(\varphi) \quad \text{as} \quad \rho \to \infty. \tag{3.62}$$

Consequently, expanding Eq. (3.61) for small crack lengths Δa writes:

$$\underline{U}^{\Delta a} \sim K_1\Delta a^{\lambda_1}\left(\left(\frac{r}{\Delta a}\right)^{\lambda_1}\underline{u}_1(\varphi) + K_{-1}\left(\frac{r}{\Delta a}\right)^{-\lambda_1}\underline{u}_{-1}(\varphi)\right) \quad \text{as} \quad \Delta a \to 0 \tag{3.63}$$

The matching principle as formulated by Van Dyke (1964) reads:

$$\begin{aligned}
&\textit{1-term inner expansion}: && \underline{U}^{\Delta a} \sim K_1\Delta a^{\lambda_1}\left(\rho^{\lambda_1}\underline{u}_1 + \hat{\underline{V}}_1(\rho,\varphi)\right) && \text{(3.64a)}\\
&\text{rewritten in outer variables}: && = K_1\Delta a^{\lambda_1}\left(\left(\frac{r}{\Delta a}\right)^{\lambda_1}\underline{u}_1 + \hat{\underline{V}}_1\left(\frac{r}{\Delta a},\varphi\right)\right) &&\\
&\text{expanded for small } \Delta a: && = K_1\left(r^{\lambda_1}\underline{u}_1 + K_{-1}\Delta a^{2\lambda_1}r^{-\lambda_1}\underline{u}_{-1}\right) + \ldots &&\\
&\text{2-term outer expansion}: && = K_1 r^{\lambda_1}\underline{u}_1 + K_1K_{-1}\Delta a^{2\lambda_1}r^{-\lambda_1}\underline{u}_{-1} && \text{(3.64b)}
\end{aligned}$$

$$\begin{aligned}
&\textit{2-term outer expansion}: && \underline{U}^{\Delta a} \sim \underline{U}^0(r,\varphi) + f_1(\Delta a)\underline{U}^1(r,\varphi) && \text{(3.65a)}\\
&\text{rewritten in inner variables} && && \text{(3.65b)}\\
&\text{and expanded for small } \Delta a: && = \underline{U}^0(\rho\,\Delta a,\varphi) + f_1(\Delta a)\underline{U}^1(\rho\,\Delta a,\varphi) + \ldots &\\
&\text{2-term inner expansion}: && = \underline{U}^0(\rho\,\Delta a,\varphi) + f_1(\Delta a)\underline{U}^1(\rho\,\Delta a,\varphi) && \text{(3.65c)}
\end{aligned}$$

Equating relations (3.64b) and (3.65c) according to the matching principle yields:

$$f_1(\Delta a) = K_1\,K_1^-\Delta a^{2\lambda_1}, \tag{3.66a}$$

$$\underline{U}^1(r,\varphi) \sim r^{-\lambda_1}\underline{u}_{-1}(\varphi) \quad \text{as} \quad r \to 0. \tag{3.66b}$$

Again, the matching condition (3.66b) implies an ill-posed problem since the term of order $O(r^{-\lambda_1})$ leads to unbounded energy for $r \to 0$. This problem can be overcome by means of the following superposition statement:

$$\underline{U}^1(r,\varphi) = r^{-\lambda_1}\underline{u}_{-1}(\varphi) + \underline{\hat{U}}_1(r,\varphi) \quad \text{with} \quad \lim_{r\to 0}\underline{\hat{U}}_1(r,\varphi) = 0. \tag{3.67}$$

Considering the perturbed problem according to Eq. (3.15) the following BVP for the unknown function $\underline{\hat{U}}_1$ arises:

$$\left\{\begin{array}{rcll}
\nabla\cdot\boldsymbol{\sigma}\left(\underline{\hat{U}}_1\right) &=& 0 & \text{in} \quad \Omega^0\\
\boldsymbol{\sigma}\left(\underline{\hat{U}}_1\right) &=& \mathbb{C}:\nabla\underline{\hat{U}}_1 & \text{in} \quad \Omega^0\\
\boldsymbol{\sigma}\left(\underline{\hat{U}}_1\right)\cdot\underline{n} &=& 0 & \text{along} \quad \partial\Omega_{\mathrm{N}}\\
\boldsymbol{\sigma}\left(\underline{\hat{U}}_1\right)\cdot\underline{n} &=& -\boldsymbol{\sigma}\left(r^{-\lambda_1}\underline{u}_{-1}(\varphi)\right)\cdot\underline{n} & \text{along} \quad \partial\Omega^0\setminus\partial\Omega_{\mathrm{N}}\\
\underline{\hat{U}}_1(\rho,\varphi) &\to& 0 & \text{as} \quad r\to 0
\end{array}\right. \tag{3.68}$$

Note that the dual term $r^{-\lambda_1}\underline{u}_{-1}$ acts now as prescribed stresses all along the boundary $\partial\Omega^0$ except for the notch faces $\partial\Omega_{\mathrm{N}}$ where all dual eigenfunctions vanish automatically[14]. Consequently, the underlying BVP is well-defined although the dual eigenfunctions are involved. The outer expansion can be written up to the second-order in Δa as follows:

$$\underline{U}^{\Delta a} = \underbrace{K_1 r^{\lambda_1}\underline{u}_1(\varphi) + \ldots}_{\underline{U}_0} + \underbrace{K_1\,K_1^-\Delta a^{2\lambda_1}\left(r^{-\lambda_1}\underline{u}_{-1}(\varphi) + \underline{\hat{U}}_1(r,\varphi)\right)}_{f_1(\Delta a)\underline{U}_1} + o\left(\Delta a^{2\lambda_1}\right). \tag{3.69}$$

On account of the BVP (3.68) two important features can be observed: First, the applied traction depends on the radial distance r associated to the boundary $\partial\Omega^0\setminus\partial\Omega_{\mathrm{N}}$. Stated slightly differently, the solution $\underline{\hat{U}}_1$ is affected by the size of the domain Ω^0 in such a way that $\underline{\hat{U}}_1$ vanishes in the limit case when the boundary $\partial\Omega^0\setminus\partial\Omega_{\mathrm{N}}$ is located at infinity. Thus, the term $\underline{\hat{U}}_1$ within the outer expansion can be interpreted

[14] The notch faces are depicted in Fig. 3.2.

as a measure of interaction between the perturbation and the outer boundary of the domain. Second, if the traction boundary conditions in the original perturbed problem are replaced equivalently by displacement boundary conditions[15] the boundary conditions in the BVP (3.68) must be adapted which eventually leads to a different solution $\underline{\hat{U}}_1$. Hence, the difference in energy dissipation due to crack onset between force-controlled and displacement-controlled loading is reflected by the higher-order correction term.

Next, the effect of the higher-order correction term $f_1(\Delta a)\underline{U}^1(r,\varphi)$ on the inner expansion is examined. For this purpose, the inner behaviour of the outer expansion is required, that is, the behaviour of $\underline{\hat{U}}_1(r,\varphi)$ for $r \to 0$. Since $\underline{\hat{U}}_1$ is defined on the unperturbed outer domain Ω^0, it possesses a similar coordinate expansion as $\underline{U}^0$ with respect the radial coordinate r:

$$\underline{\hat{U}}_1(r,\varphi) \sim \sum_{k=1}^{N} H_k r^{\lambda_k} \underline{u}_k(\varphi) \quad \text{as} \quad r \to 0. \tag{3.70}$$

The corresponding intensity factors are denoted by H_i in order avoid any confusion with the intensity factors K_i associated to $\underline{U}^0$. It follows:

$$\begin{aligned}
&\textit{2-term outer expansion}: && \underline{U}^{\Delta a} \sim \underline{U}^0(r,\varphi) + f_1(\Delta a)\underline{U}^1(r,\varphi) && \text{(3.71a)}\\
&\quad \text{rewritten in inner variables}: && = \underline{U}^0(\rho\,\Delta a,\varphi) + f_1(\Delta a)\underline{U}^1(\rho\,\Delta a,\varphi) && \text{(3.71b)}\\
&\quad \text{expanded for small } \Delta a: && = K_1 \Delta a^{\lambda_1}\left(\rho^{\lambda_1}\underline{u}_1 + K_{-1}\rho^{-\lambda_1}\underline{u}_{-1}\right) + \dots\\
&\quad n+1\text{-term inner expansion}: && = K_1 \Delta a^{\lambda_1}\left(\rho^{\lambda_1}\underline{u}_1 + K_{-1}\rho^{-\lambda_1}\underline{u}_{-1}\right)\\
& && \quad + K_2 \Delta a^{\lambda_2}\rho^{\lambda_2}\underline{u}_2 + \dots\\
& && \quad + K_1\,K_{-1}\,H_1 \Delta a^{3\lambda_1}\rho^{\lambda_1}\underline{u}_1 && \text{(3.71c)}
\end{aligned}$$

$$\begin{aligned}
&\textit{n+1-term inner expansion}: && \underline{U}^{\Delta a} \sim F_1(\Delta a)\underline{V}^1 + \dots + F_{n+1}(\Delta a)\underline{V}^{n+1} && \text{(3.72)}\\
&\quad \text{rewritten in outer variables}\\
&\quad \text{and expanded for small } \Delta a: && = F_1(\Delta a)\underline{V}^1\left(\frac{r}{\Delta a},\varphi\right) + \dots && \text{(3.73)}\\
&\quad n+1\text{-term outer expansion}: && = F_1(\Delta a)\underline{V}^1\left(\frac{r}{\Delta a},\varphi\right)\\
& && \quad + \dots + F_{n+1}(\Delta a)\underline{V}^{n+1}\left(\frac{r}{\Delta a},\varphi\right) && \text{(3.74)}
\end{aligned}$$

Following Fig. 3.5, the index $n+1$ is introduced, since it depends on the problem-specific eigenvalue spectrum at which position the term $K_1\,K_1^-\,H_1\Delta a^{3\lambda_1}\rho^{\lambda_1}$ in Eq. (3.71c) appears in the inner expansion of the outer expansion. For instance, if $\lambda_1 < 3\lambda_1 < \lambda_2$ the interaction term arises at the second position and it follows $n+1=2$. If $\lambda_1 < \lambda_2 < 3\lambda_1 < \lambda_3$ it follows $n+1=3$. Evaluating the matching condition and again utilising

[15] This means that the reaction forces in case of displacement-controlled loading equal the prescribed tractions in case of force-controlled loading.

the superposition principle ultimately yields:

$$F_{n+1}(\Delta a) = K_1\, K_1^-\, H_1 \Delta a^{3\lambda_1}, \tag{3.75a}$$

$$\underline{V}^{n+1}(\rho,\varphi) = \rho^{\lambda_1}\underline{u}_1(\varphi) + \hat{\underline{V}}_1(\rho,\varphi) \quad \text{as} \quad \rho \to \infty \tag{3.75b}$$

The behaviour of the function $\hat{\underline{V}}_1$ at infinity is already given by Eq. (3.27). The inner expansion can now be written in the form:

$$\begin{aligned}\underline{U}^{\Delta a} \sim & K_1 \Delta a^{\lambda_1}\left(\rho^{\lambda_1}\underline{u}_1(\varphi) + \hat{\underline{V}}_1(\rho,\varphi)\right) + K_2 \Delta a^{\lambda_2}\left(\rho^{\lambda_2}\underline{u}_2(\varphi) + \hat{\underline{V}}_2(\rho,\varphi)\right) + \dots \\ & + K_1\, K_1^-\, H_1 \Delta a^{3\lambda_1}\left(\rho^{\lambda_1}\underline{u}_1(\varphi) + \hat{\underline{V}}_1(\rho,\varphi)\right) \quad \text{as} \quad \Delta a \to 0.\end{aligned} \tag{3.76}$$

Thus, the higher-order correction term of the outer expansion affects the inner expansion with terms of order $O(3\lambda_1)$. The effect of these higher-order terms on the energy dissipation due to crack formation and hence the IERR is studied exemplarily using the model problem sketched in Fig. 3.6(a). A 90°-notch with a circular boundary of radius R is considered. At the boundary of the perturbed domain $\Omega^{\Delta a}$, either tractions or equivalent displacement conditions are prescribed:

$$\underline{t}^* = K_1 R^{\lambda_1 - 1}\boldsymbol{\sigma}_1(\varphi)\cdot\underline{n} \quad \text{or} \quad \underline{u}^* = K_1 R^{\lambda_1}\underline{u}_1(\varphi) \quad \text{along} \quad \partial\Omega^{\Delta a}\setminus\partial\Omega_{\mathrm{N}}. \tag{3.77}$$

The model problem is constructed in such a way that the unperturbed solution $\underline{U}^0$ is completely known and equals the eigenfunction:

$$\underline{U}^0(r,\varphi) = K_1 r^{\lambda_1}\underline{u}_1(\varphi). \tag{3.78}$$

Substituting the solution (3.78) of the unperturbed problem and the inner expansion (3.76) into the Ψ-integral yields the following expression of the IERR:

$$\bar{\mathcal{G}}(\Delta a) = K_1^2 \Delta a^{2\lambda_1 - 1}\Psi_{11} + K_1^2 K_{-1} H_1 \Delta a^{4\lambda_1 - 1}\Psi_{11} + o\left(\Delta a^{4\lambda_1 - 1}\right), \tag{3.79}$$

with

$$\Psi_{11} = \Psi\left(\rho^{\lambda_1}\underline{u}_1, \hat{\underline{V}}_1\right). \tag{3.80}$$

The solution $\hat{\underline{V}}_1^{\mathrm{FE}}$ is computed numerically using FEA. The intensity factor K_{-1} associated to the dual eigenfunction $r^{-\lambda_1}\underline{u}_{-1}$ is calculated by

$$K_{-1} = \frac{\Psi\left(\hat{\underline{V}}_1^{\mathrm{FE}}, r^{\lambda_1}\underline{u}_1(\varphi)\right)}{\Psi\left(r^{\lambda_1}\underline{u}_1(\varphi), \eta^{-\lambda_1}\underline{u}_{-1}(\varphi)\right)}. \tag{3.81}$$

In order to calculate the quantity H_1, the BVP (3.68) is solved using FEA and it follows:

$$H_1 = \frac{\Psi\left(\hat{\underline{U}}_1^{\mathrm{FE}}, r^{-\lambda_1}\underline{u}_{-1}(\varphi)\right)}{\Psi\left(r^{\lambda_1}\underline{u}_1(\varphi), \eta^{-\lambda_1}\underline{u}_{-1}(\varphi)\right)}. \tag{3.82}$$

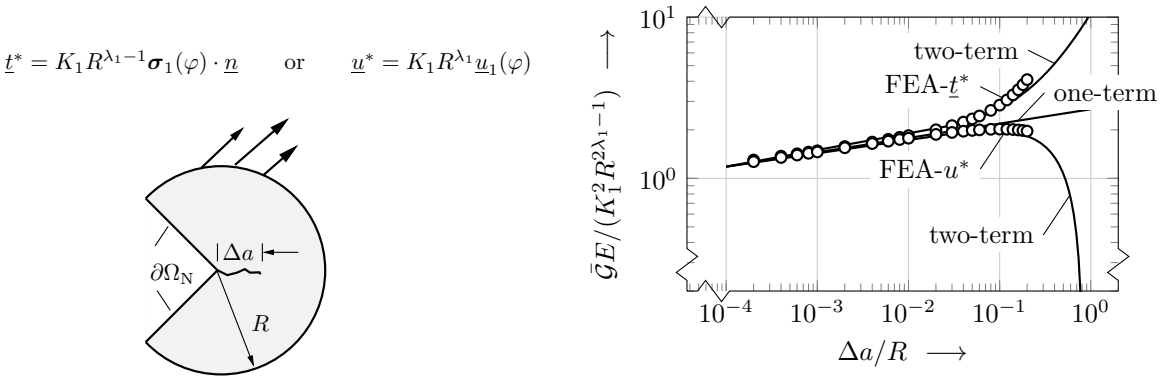

(a) Schematics of the model problem with boundary conditions applied on the portion $\partial\Omega^{\Delta a} \setminus \partial\Omega_\mathrm{N}$ of the boundary $\partial\Omega^{\Delta a}$.

(b) IERR with respect to the dimensionless crack length $\Delta a/R$.

Figure 3.6: Model problem of a 90° re-entrant corner with an outer radius R containing a crack of length Δa. The notch is either loaded by applied traction $\underline{t}^*$ or displacements $\underline{u}^*$ along the outer boundary.

The dimensionless IERR for force-controlled loading as well as for equivalent displacement-controlled loading is shown in Fig. 3.6(b) with respect to the normalised crack length $\Delta a/R$. For both cases, a numerical reference solution of the IERR is computed and compared against the asymptotic expansion according to Eq. (3.79). Since the type of boundary conditions affects the solution only in form of higher-order terms, the results for force-controlled and displacement-controlled loading coincide for small values of $\Delta a/R$. In this region, the leading-order term captures the IERR irrespectively of the boundary conditions. Only for $\Delta a/R > 0.1$ results start to increasingly deviate and the effect of boundary conditions becomes visible. As shown in Fig. 3.6(b), this behaviour can be rendered employing higher-order correction terms. However, this requires to calculate $\underline{\hat{U}}_1$ and therefore increases the computational effort. Supposing that the crack length is sufficiently small compared to a characteristic structural length, these higher-order terms are not taken into account in the subsequent analysis without loss of generality. The structural situations tackled in the subsequent sections serve as a basis for a thorough discussion and assessment of the asymptotic's range of validity and applicability.

Chapter 4

Mixed-mode failure at homogeneous and bi-material junctions

In this section, crack initiation at homogeneous and bi-material notches is predicted employing the coupled stress and energy criterion. Under the hypothesis of brittle fracture and that cracks can be considered as small compared to any other characteristic structural length, an efficient semi-analytical framework is presented based on asymptotic expansions of stresses and energy dissipation. Three different structural situations are examined where mixed-mode conditions are present. First, a butt joint under uniaxial tensile loading is considered where failure occurs along the material interface between adhesive and adherend. Second, a homogeneous 90° *re-entrant corner is investigated offering multiple admissible crack configurations under mixed-mode loading. Third, failure of a bi-material scarf joint under four-point bending is investigated where competing failure scenarios are present. Based on fully numerical reference solutions, the suitability and restrictions of the asymptotic approach are discussed in detail. In comparison with cohesive zone modelling and experimental data from literature, it is shown that the asymptotic approach allows for accurately predicting the critical load at failure, the finite crack length and the crack initiation angle. Moreover, the criterion allows for identifying the correct failure configuration out of a set of competing failure scenarios. The modelling and results presented in this section have been published in the International Journal of Solids and Structures (Felger et al., 2019a) and in Composite Structures (Felger et al., 2019b).*

4.1 Introduction

The applied asymptotic methodology is sketched in Fig. 4.1 to provide an overview of the particular steps. At the outset, the primal eigenvalues and eigenfunctions as well as the dual eigenvalues and eigenfunctions are determined employing the method of complex potentials. Subsequently, the unperturbed problem where no crack is present is solved numerically and the required GSIFs are calculated using the Ψ-integral. To compute the scaling coefficients Ψ_{ij} involved in the expansion of the IERR, the corresponding BVPs on the scaled inner domain Ω^∞ are solved by means of FEA. Finally, the asymptotic expansions of stresses and IERR are substituted in the CC.

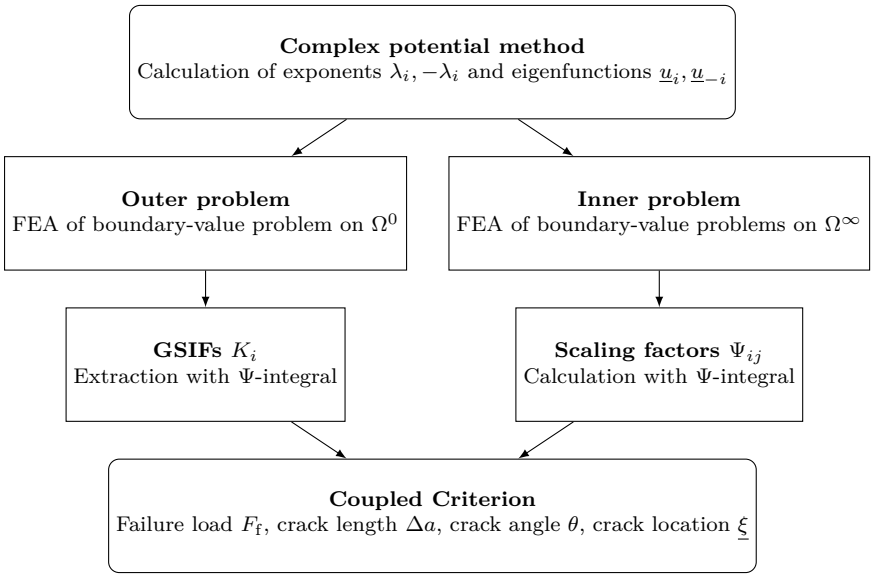

Figure 4.1: Overview of the asymptotic approach

4.2 Failure of butt joints under uniform tensile loading

The adhesively bonded butt joint represents the most common joint configuration for testing the response of adhesives under tensile, compressive and shear loading. However, butt joints are typically avoided in structural joints since comparatively small bending moments induce high peeling stresses, which may cause joint's failure. Nevertheless, edge-to-edge butt joint configurations still exist for instance in rotor blades of wind turbines where composite materials are used (Sørensen, 2009) or in plastic-encapsulated LSI (Large Scale Integrated Circuit) devices (Murakami, 1989). Furthermore, butt joints offer a very suitable way to characterise the adhesive strength and are therefore used in standardised tests (ASTM D897, 2016, ASTM D2095, 2015). In contrast to tests with bulk specimens, the adhesive is tested in a thin-film form representing real service conditions most precisely. Hence, an efficient mechanical model of a butt joint is most desired offering a simple and reliable evaluation of test data and serving as a basis for inverse parameter identification. In the above-mentioned tests, the adhesive effective strength is obtained by relating the measured failure load to the bonded area. In reality, however, the stress field and failure process are rather complex although the joint's geometry is quite simple. High stress concentrations, which even are mathematically singular, occur at the bi-material points at the material interface. These stress singularities trigger failure which occurs adhesively along the interface in a small region at the bi-material junction (Reedy , 1993, Anderson and DeVries, 1989).

Consider a butt joint of length l, width w and adhesive thickness t under uniform tensile loading σ_∞ as depicted in Fig. 4.2. Young's modulus and Poisson's ratio of the adherends and the adhesive are denoted as E_1, ν_1 and E_2, ν_2, respectively. The employed adhesive is supposed to possess a brittle failure behaviour and the size of the plastic zone is negligible in comparison to all other length scales involved. Thus, crack onset is mainly governed by the local linear-elastic notch stress field which is

accurately represented by the leading-order terms of the stress asymptotic expansion. According to the experiments by Reedy and Guess (1995) and Reedy (2002), crack formation is assumed along the material interface and the event of crack onset is followed by catastrophic failure of the joint. Butt joint failure is assessed employing the semi-analytical asymptotic approach. In particular, the effects of the adhesive thickness and the elastic mismatch between adhesive and adherend on the failure load are discussed in detail. Results are compared to numerical cohesive zone data and to a purely numerical evaluation of the CC in order to examine the validity range of the asymptotic approach. Finally, theoretical predictions are validated against experimental findings from literature.

4.2.1 Asymptotic stress field and comparison with numerics

The asymptotic stress field is characterised by the corresponding eigenvalues and eigenvectors representing the solution of the eigenvalue problem in Eq. (3.7). The involved coefficient matrix $\mathbf{D}$ corresponding to the local notch geometry of the butt joint, cf. Fig. 4.3, reads:

$$\mathbf{D} = \begin{pmatrix} 1 & \lambda & 0 & 1 & -1 & -\lambda & 0 & -1 \\ \lambda & 1 & 1 & 0 & -\lambda & -1 & -1 & 0 \\ \kappa_1 & -\lambda & 0 & -1 & -\kappa_2\tilde{G} & \lambda\tilde{G} & 0 & \tilde{G} \\ -\lambda & \kappa_1 & -1 & 0 & \lambda\tilde{G} & -\kappa_2\tilde{G} & \tilde{G} & 0 \\ \mathrm{i}^{\lambda-1} & \mathrm{i}\lambda(-\mathrm{i})^{\lambda} & 0 & -\mathrm{i}^{\lambda+1} & 0 & 0 & 0 & 0 \\ \lambda\mathrm{i}^{\lambda-1} & (-\mathrm{i})^{\lambda-1} & \mathrm{i}^{\lambda+1} & 0 & 0 & 0 & 0 & 0 \\ 0 & 0 & 0 & 0 & \mathrm{i}\lambda(-\mathrm{i})^{\lambda} & \mathrm{i}^{\lambda-1} & -\mathrm{i}^{\lambda+1} & 0 \\ 0 & 0 & 0 & 0 & (-\mathrm{i})^{\lambda-1} & \lambda\mathrm{i}^{\lambda-1} & 0 & \mathrm{i}^{\lambda+1} \end{pmatrix}. \tag{4.1}$$

Here, $\tilde{G} = G_1/G_2$ denotes the shear modulus ratio of adherend and adhesive. Caused by the elastic mismatch, stress singularities may arise at the point where dissimilar materials meet each other. In order to get a first impression of the eigenvalue spectrum for the considered bi-material configuration, the eigenvalues inducing singularities, also denoted as singularity exponents, are calculated based on the characteristic equation (3.8) using the coefficient matrix in Eq. (4.1). In Fig. 4.3, the exponent λ_1 is plotted

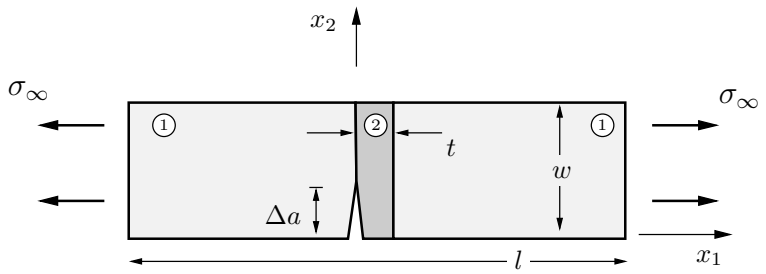

Figure 4.2: Butt joint specimen with length l, width w and adhesive thickness t under uniform tensile loading σ_∞ with a crack of length Δa associated to failure. Young's modulus and Poisson's ratio of the adherends and the adhesive are denoted as E_1, ν_1 and E_2, ν_2, respectively.

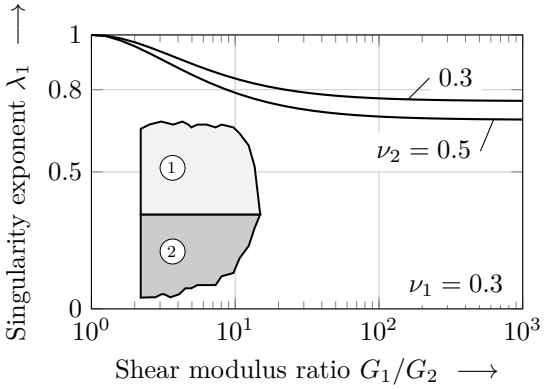

Figure 4.3: Singularity exponent λ_1 of a straight edge bi-material notch configuration with respect to the shear modulus ratio G_1/G_2 of the constituents.

against the shear modulus ratio G_1/G_2. Since the local notch geometry is a straight edge, no singularity arises for $G_1/G_2 = 1$ and $\nu_1 = \nu_2$, that is, a homogeneous material. However, as long as a material mismatch is present, stress singularities occur. It is observed that the singularity exponent λ_1 decreases with increasing material mismatch, that is, the stress singularity becomes stronger. Moreover, λ_1 finally approaches an asymptote for $G_1/G_2 \to \infty$ and the limit value depends only on Poisson's ratio ν_2 of the adhesive.

After eigenvalues and eigenvectors are determined, the GSIFs can be calculated and the local notch stress field is fully characterised. The procedure of GSIF extraction is exemplarily demonstrated considering a butt joint composed of epoxy adhesive and steel adherends as shown in Fig. 4.4(a). The corresponding material parameters are given in Table A.1. Let us focus on K_1 associated with the leading-order term in the expansion of the stress field:

$$\boldsymbol{\sigma}\,(r,\varphi) \sim K_1 r^{\lambda_1 - 1} \boldsymbol{\sigma}_1(\varphi) \quad \text{as} \quad r \to 0. \tag{4.2}$$

Since λ_1 and $\boldsymbol{\sigma}_1(\varphi)$ are universal quantities independent of the macroscopic parameters, e.g. the adhesive thickness, it is the intensity factor K_1 which must account for the impact of the adhesive thickness t and the far-field loading σ_∞:

$$K_1 = f(t, \sigma_\infty). \tag{4.3}$$

Using a LF-system (length-force-system), the dimensions of the dependent variable K_1 and the independent variables t and σ_∞ are summarised in the following dimension matrix:

$$\begin{array}{c|c|ccc} & & K_1 & t & \sigma_\infty \\ \hline L & \| & -1-\lambda_1 & 1 & -2 \\ F & \| & 1 & 0 & 1 \end{array} \tag{4.4}$$

Applying Buckingham's Π theorem of dimensional analysis, cf. Barenblatt and Isaakovich

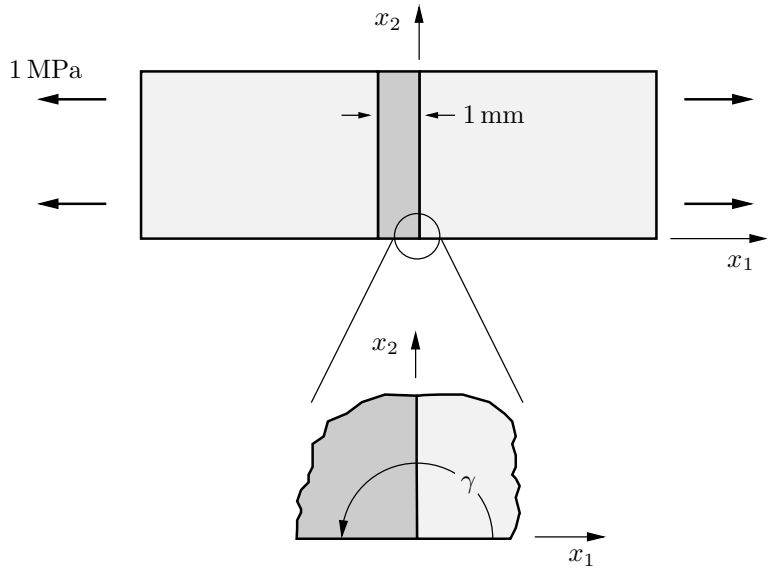

(a) Schematic of the butt joint with unit loading $\sigma_\infty = 1$ MPa and unit adhesive thickness $t = 1$ mm.

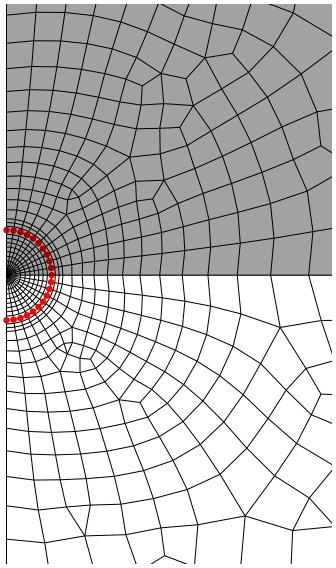

(b) Detail of FE model with integration path indicated in red.

Figure 4.4: Extraction of the GSIF K_1 using the Ψ-integral for the considered butt joint configuration.

(1996), allows for rewriting Eq. (4.3) in the dimensionally correct form:

$$K_1 = \hat{K}_1 t^{1-\lambda_1} \sigma_\infty. \tag{4.5}$$

Equation (4.5) represents a scaling law describing how K_1 scales in terms of the adhesive thickness and the applied far-field loading. $\hat{K}_1$ is a dimensionless constant to be determined using one FEA and the Ψ-integral according to Section 2.3.2. Evaluating the Ψ-integral, integration is performed along the path γ in a counter-clockwise sense as depicted in Fig. 4.4(a). In the numerical model, it is suitable to set the adhesive thickness equal to unit-length and the loading equal to unit-stress. In that case, the numerical value of K_1 equals $\hat{K}_1$ and employing the Ψ-integral yields:

$$\hat{K}_1 = \frac{\Psi\left(\underline{u}^{\mathrm{FE}}, r^{-\lambda_1}\underline{u}_{-1}(\varphi)\right)}{\Psi\left(r^{\lambda_1}\underline{u}_1(\varphi), r^{-\lambda_1}\underline{u}_{-1}(\varphi)\right)}. \tag{4.6}$$

The mesh of the comparative finite element model is depicted in Fig. 4.4(b) and the path of integration along which the Ψ-integral is evaluated is highlighted in red. A radial mesh in the vicinity of the bi-material notch tip is employed and a quarter-model is used applying proper displacement symmetry boundary conditions. The numerical model is generated employing the commercial FE software Abaqus. The model has approximately 1×10^4 degrees of freedom and continuum plane strain elements (CPE4) are used. Convergence as well as path-independence of the Ψ-integral were checked. For an efficient calculation of the GSIFs, the evaluation of the Ψ-integral has been

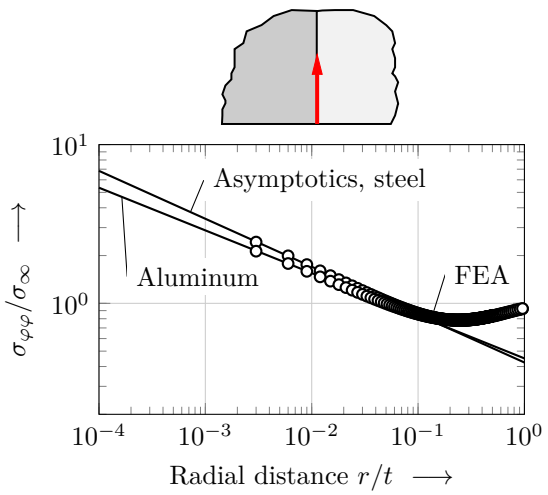

(a) Normalised circumferential stress $\sigma_{\varphi\varphi}$ with respect to the normalised radial distance r along the material interface. Results are given for an epoxy adhesive combined with either steel or aluminum adherends, respectively.

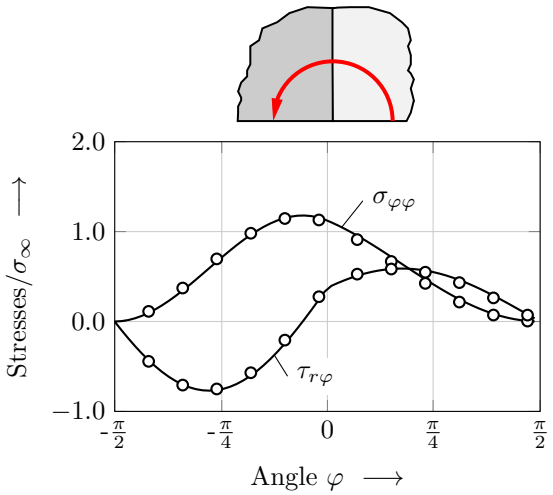

(b) Stress distribution along a circular path fully enclosing the notch tip at a normalised distance $r/t = 0.04$. Results are given for an epoxy adhesive (left) combined with steel adherends (right). Material interface at $\varphi = 0$.

Figure 4.5: Comparison between leading-order asymptotic stress solution and numerical finite element results in radial as well as circumferential direction. Results according to the asymptotic approach are plotted as solid lines.

implemented and automatised as a post-processing operation in PYTHON. A comparison between the asymptotic notch stress field and numerical data using FEA is provided in Fig. 4.5. Two configurations, that is, a steel-epoxy and an aluminum-epoxy joint are examined. The behaviour of the circumferential stress $\sigma_{\varphi\varphi}$ with respect to the normalised radial coordinate r/t is depicted in Fig. 4.5(a). Stresses are evaluated along the material interface. Since a log–log plot is employed, the asymptotic solution according to Eq. (4.2) appears as a straight line with slope $\lambda_1 - 1$. A comparison shows that the slope as well as the intercept of the straight lines are in a very good agreement with the numerical data. This represents a sound indication for an accurate calculation of K_1 as well as the correctness of the singularity exponent λ_1. Furthermore, the effect of the elastic contrast is rendered correctly. Higher local stresses appear in the case of steel adherends compared to aluminum adherends. The leading-order term correctly captures the numerical reference data up to a distance of 10% of the adhesive thickness t. For larger relative distances, the accuracy of the leading-order term decreases since the influence of higher-order terms within the series expansion is getting more pronounced. Figure 4.5(b) shows the circumferential distribution of the stress components $\sigma_{\varphi\varphi}$ and $\tau_{r\varphi}$ along a circular path enclosing the notch-tip. The path is located at a normalised distance $r/t = 0.04$ away from the bi-material point. It is observed, that the numerical results are rendered correctly by the asymptotic solution, again indicating correctness of the eigenfunction $\boldsymbol{\sigma}_1(\varphi)$, the eigenvalue λ_1 as well as K_1. Looking at the distribution of the shear stress $\tau_{r\varphi}$, a kink at $\varphi = 0$ is observed as a result of the transition from one material to the other.

4.2.2 Asymptotics of the energy release and comparison with numerics

After the local notch stress field is determined, let us investigate the asymptotic expansion of the IERR. According to Section 3 and Eq. (4.5), the expansion writes at the leading-order:

$$\bar{\mathcal{G}} \sim \left(\hat{K}_1 \sigma_\infty t^{1-\lambda_1}\right)^2 \Delta a^{2\lambda_1 - 1} \Psi_{11} \quad \text{as} \quad \Delta a \to 0. \tag{4.7}$$

The scaling coefficient Ψ_{11} is calculated by means of the Ψ-integral in Eq. (3.50), inserting the eigenfunction $\rho^{\lambda_1}\underline{u}_1$ and the function $\underline{\hat{V}}_1$. The function $\underline{\hat{V}}_1$ is the solution of the BVP (3.28) which is solved numerically using FEA. Calculations are performed on a semicircular domain representing the inner domain Ω^∞. To properly describe the infinite domain Ω^∞, the numerical model is artificially bounded with an outer radius significantly larger compared to the perturbation (the crack of unit length). Here, a normalised radius of approximately 250 has been identified as a suitable choice in accordance with Yosibash et al. (2006). Alternatively, infinite elements can also be used which, however, are not included in the standard element library of Abaqus. A detail of the employed FE mesh showing the vicinity of the crack is provided in Fig. 4.6(a). The Ψ-integral is evaluated with respect to the inner domain and the path of integration is indicated by red dots. The presented crack opening results from applied tractions along the crack faces as stated in the underlying BVP. The right crack face corresponds to the epoxy adhesive, thus the deformation is more pronounced compared to the left crack face associated to the stiffer adherend. Since the eigensolution and the function $\underline{\hat{V}}_1$ are independent of any global quantities such as the applied far field loading or the adhesive thickness, the scaling coefficient Ψ_{11} depends only on local parameters, that is, the material mismatch of the bi-material junction[16]:

$$\Psi_{11} = F(E_1, E_2, \nu_1, \nu_2). \tag{4.8}$$

According to Eq. (4.7), Ψ_{11} has the dimension of 1/MPa and applying dimensional analysis directly yields

$$\Psi_{11} = \frac{1}{E_2} \hat{\Psi}_{11} \left(\frac{E_1}{E_2}, \nu_1, \nu_2\right), \tag{4.9}$$

with the dimensionless quantity $\hat{\Psi}_{11}$. Combining Eq. (4.7) with Eq. (4.9), the expansion of the IERR reads:

$$\bar{\mathcal{G}} \sim \frac{\hat{K}_1^2 \sigma_\infty^2 t}{E_2} \hat{\Psi}_{11} \left(\frac{E_1}{E_2}, \nu_1, \nu_2\right) \left(\frac{\Delta a}{t}\right)^{2\lambda_1 - 1} \quad \text{as} \quad \Delta a \to 0. \tag{4.10}$$

The normalised IERR for an epoxy-steel and an epoxy-aluminum butt joint is depicted in Fig. 4.6(b) with respect to the dimensionless crack length $\Delta a/t$. The leading-order approximation in Eq. (4.10) is compared against finite element data employing 20 discrete crack lengths. Since logarithmic scales are used, the asymptotic solution

[16] In general, the scaling coefficient also depends on the orientation of the crack as a local quantity which is not relevant at this point since crack onset is presumed along the interface.

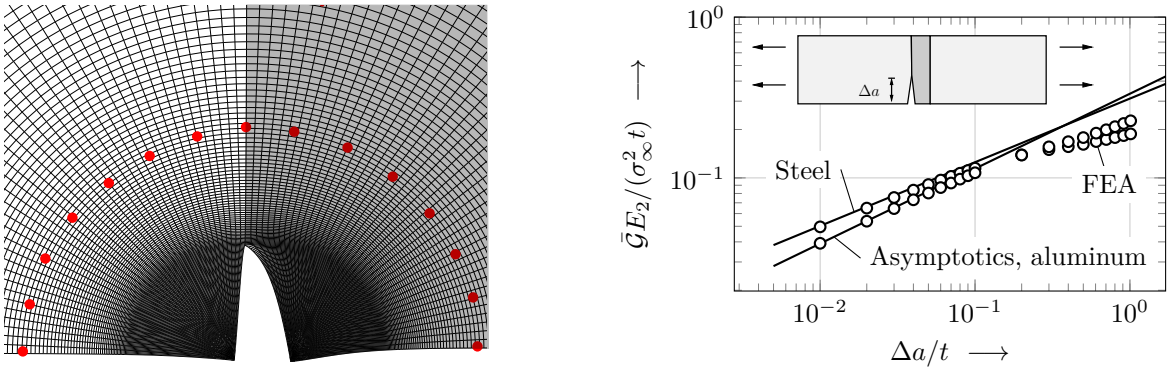

(a) Detail of the finite element mesh used for the inner configuration in the vicinity of the crack with unit length.

(b) Comparison of the leading-order term and numerical reference data for a steel-epoxy and an aluminum-epoxy butt joint.

Figure 4.6: Asymptotic expansion of the IERR: employed numerical model and comparison to reference data.

appears as a straight line with slope $2\lambda_1 - 1$. It is observed that results based on the asymptotic approach are in a very good agreement with the numerical reference data for crack lengths up to 10% of the adhesive's thickness. Furthermore, the effect of different material combinations on the IERR is covered correctly. In case of larger cracks, the leading-order asymptotic solution deviates from the reference data since higher-order terms start to play a dominant role.

4.2.3 Asymptotic failure predictions and numerical reference data

The obtained asymptotic expansions for the stresses and the IERR are now used to evaluate the CC and predict the critical load at failure of the butt joint. As shown in Section 4.2.1, stresses along the interface show a monotonically decreasing behaviour with increasing distance to the notch tip. In contrast, the IERR is a monotonically increasing function with respect to the crack length Δa. Under these circumstances, the optimisation problem in Eq. (2.74) defining the CC simplifies to

$$\sigma_\mathrm{f} = \min_{\Delta a, \sigma_\infty} \left\{ \sigma_\infty \;\middle|\; g\left(\boldsymbol{\sigma}\left(\underline{x}_\mathrm{ct}\right)\right) = 1 \quad \wedge \quad \bar{\mathcal{G}}(\Delta a) = \frac{1}{\Delta a}\int_0^{\Delta a} \mathcal{G}_c(\chi(a))\mathrm{d}a \right\}, \tag{4.11}$$

where $\underline{x}_\mathrm{ct}$ denotes the coordinates of the potential crack tip. In this case, the critical far-field stress at failure and the corresponding finite crack size can be calculated without employing sophisticated strategies of non-linear optimisation. Since $\boldsymbol{\sigma} \propto \sigma_\infty$ and $\bar{\mathcal{G}} \propto \sigma_\infty^2$ holds within linear elasticity, the relation

$$\frac{\bar{\mathcal{G}}(\Delta a)}{g\left(\boldsymbol{\sigma}\left(\underline{x}_\mathrm{ct}\right)\right)^2} = \frac{1}{\Delta a}\int_0^{\Delta a} \mathcal{G}_c(\chi(a))\mathrm{d}a \tag{4.12}$$

is independent of the far-field loading σ_∞ and its solution directly yields the resulting finite crack length Δa. The associated failure stress can be determined subsequently evaluating either the stress or the energy criterion using the previously calculated crack length. Since the crack is presumed to form along the material interface, normal stresses $\sigma_{\varphi\varphi}$ as well as shear stresses $\tau_{r\varphi}$ are present. To account for this mixed-mode condition, the elliptical interaction law introduced in Eq. (2.66) is employed, setting $p = 2$. Based on Eq. (4.2), the stress criterion evaluated at the potential location of the crack tip $(r = \Delta a, \varphi = 0)$ reads:

$$g\left(\boldsymbol{\sigma}\left(\underline{x}_{\mathrm{ct}}\right)\right) = \hat{K}_1 t^{1-\lambda_1} \Delta a^{\lambda_1 - 1} \sigma_\infty \sqrt{\left(\frac{\sigma_{\varphi\varphi,1}(\varphi=0)}{\sigma_{\mathrm{c}}}\right)^2 + \left(\frac{\tau_{r\varphi,1}(\varphi=0)}{\tau_{\mathrm{c}}}\right)^2} = 1. \tag{4.13}$$

Note that $\sigma_{\varphi\varphi,1}(\varphi)$ and $\tau_{r\varphi,1}(\varphi)$ are dimensionless stress eigenfunctions, which depend only on the circumferential coordinate φ, cf. Eq. (3.12). In terms of the energy criterion, the simple criterion $\bar{\mathcal{G}} = \mathcal{G}_{\mathrm{Ic}}$ is employed disregarding any effect of the mixed-mode angle on the fracture toughness:

$$\frac{\hat{K}_1^2 \sigma_\infty^2 t}{E_2}\, \hat{\Psi}_{11}\left(\frac{E_1}{E_2}, \nu_1, \nu_2\right) \left(\frac{\Delta a}{t}\right)^{2\lambda_1 - 1} = \mathcal{G}_{\mathrm{Ic}}. \tag{4.14}$$

The effect of using a mixed-mode energy criterion is discussed at the end of this section. The two relations in Eqn. (4.13)-(4.14) form a system of two equations which can be directly solved for the two unknowns, that is, the failure stress σ_{f} and the finite crack length Δa:

$$\sigma_{\mathrm{f}} = \frac{1}{\hat{K}_1} \left(\frac{\mathcal{G}_{\mathrm{Ic}} E_2}{\hat{\Psi}_{11}\, t}\right)^{1-\lambda_1} \left(\left(\frac{\sigma_{\varphi\varphi,1}(\varphi=0)}{\sigma_{\mathrm{c}}}\right)^2 + \left(\frac{\tau_{r\varphi,1}(\varphi=0)}{\tau_{\mathrm{c}}}\right)^2\right)^{\frac{1-2\lambda_1}{2}}, \tag{4.15}$$

$$\Delta a = \frac{\mathcal{G}_{\mathrm{Ic}} E_2}{\sigma_{\mathrm{c}}^2} \frac{1}{\hat{\Psi}_{11}} \left(\sigma_{\varphi\varphi,1}(\varphi=0)^2 + \left(\frac{\sigma_{\mathrm{c}} \tau_{r\varphi,1}(\varphi=0)}{\tau_{\mathrm{c}}}\right)^2\right). \tag{4.16}$$

It is worth mentioning, that there is a formal similarity between Eq. (4.16) for the crack length and the relations for the critical distances in Eq. (1.1) given at the beginning of this work. However, the coefficient $\hat{\Psi}_{11}$ automatically adjusts the "critical distance" to the local notch geometry without the need of an additional fit to experimental data. Moreover, this shows that a critical distance in the present framework does not represent a material property but depends on the geometrical features of the structure.

In order to check the accuracy of Eq. (4.15) and Eq. (4.16), the CC is additionally evaluated based on numerical data for the stresses and the IERR. According to dimensional analysis, these quantities can be written in the form:

$$\sigma_{ij} = \sigma_\infty \hat{\sigma}_{ij}\left(\frac{r}{t}, \frac{E_2}{E_1}, \nu_1, \nu_2\right), \tag{4.17}$$

$$\bar{\mathcal{G}} = \frac{\sigma_\infty^2\, t}{E_2}\, \hat{\bar{\mathcal{G}}}\left(\frac{\Delta a}{t}, \frac{E_1}{E_2}, \nu_1, \nu_2\right). \tag{4.18}$$

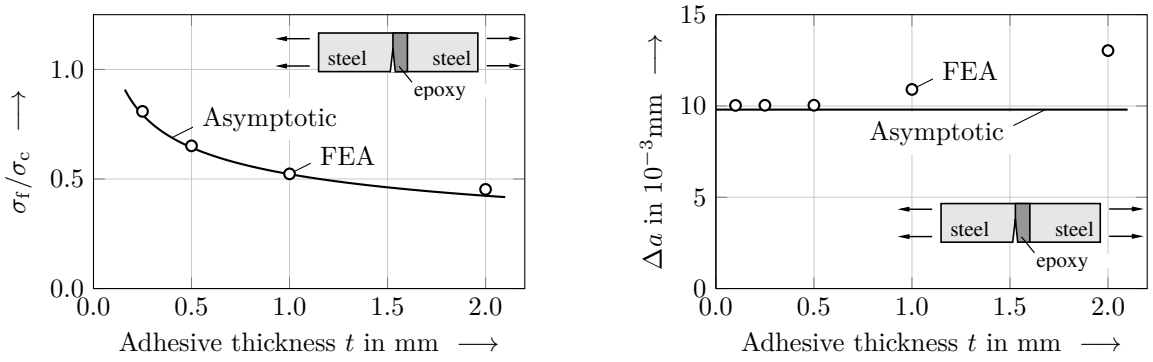

(a) Dimensionless failure stress.

(b) Finite crack length.

Figure 4.7: Comparison of the failure stress and finite crack size according to the CC obtained by using asymptotics and a fully numerical reference solution. Joint dimensions: $l = 66.2$ mm, $w = 28.6$ mm.

Here, $\hat{\sigma}_{ij}$ and $\hat{\hat{\mathcal{G}}}$ are dimensionless functions, respectively, which are calculated using FEA. On account of Eq. (4.12), the resulting crack length Δa can be determined from the relation

$$\frac{\hat{\hat{\mathcal{G}}}}{\hat{\sigma}_{\varphi\varphi}^2 + \left(\frac{\hat{\tau}_{r\varphi}\sigma_c}{\tau_c}\right)^2} = \frac{\mathcal{G}_{\mathrm{Ic}} E_2}{t\,\sigma_c^2}. \tag{4.19}$$

The dimensionless functions $\hat{\sigma}_{ij}$ and $\hat{\hat{\mathcal{G}}}$ on the left-hand side are calculated numerically for different values of the dimensionless ratios r/t and $\Delta a/t$, respectively. Subsequently, a spline interpolation of these functions is performed and a numerical root search using either MATHEMATICA or PYTHON is carried out to solve Eq. (4.19) for the resulting dimensionless crack length. A comparison between the asymptotic approach and a purely numerical evaluation of the CC in terms of failure stress and crack length is shown in Fig. 4.7. The results are based on a steel-epoxy joint with material properties according to Table A.1. The predicted normalised failure stress σ_f/σ_c is plotted in Fig. 4.7(a) with respect to the adhesive thickness t. A very good agreement between numerics and asymptotics is observed with a maximum relative error smaller than 6%. Both approaches yield a decreasing failure stress for an increasing adhesive thickness t. This behaviour is also referred to as adhesive thickness effect (da Silva et al., 2006, Stein et al., 2015, Weißgraeber and Becker, 2013), and can be captured using the CC. The corresponding finite crack length Δa is depicted in Fig. 4.7(b). According to Eq. (4.16), the crack length is independent of the adhesive thickness in the asymptotic approach and takes the value $\Delta a = 0.0098$ mm. Hence, the initial assumption that the perturbation is much smaller compared to a characteristic structural length is satisfied for the considered range of adhesive thickness. The numerical data shows a varying crack length with respect to the adhesive thickness finally approaching the asymptotic prediction for small values of t.

The results in Fig. 4.7 are based on the simple form of the energy criterion $\bar{\mathcal{G}} = \mathcal{G}_{\mathrm{Ic}}$ and it is natural to ask, to which extent the prediction of the joint's effective strength is affected by taking into account an energy mixed-mode criterion. Let us investigate this effect using the phenomenological mixed-mode criterion in Eq. (2.71) proposed by Hutchinson and Suo (1991). This criterion essentially provides an effective fracture toughness $\mathcal{G}_{\mathrm{c}}$ depending on $\mathcal{G}_{\mathrm{Ic}}$, $\mathcal{G}_{\mathrm{IIc}}$ and the mixed-mode angle χ. For only the fracture toughness $\mathcal{G}_{\mathrm{Ic}}$ of the employed epoxy adhesive is known, it is assumed that $\mathcal{G}_{\mathrm{IIc}} = 2\mathcal{G}_{\mathrm{Ic}}$ holds as frequently observed in experiments (Stein et al., 2015). In this case the energy criterion takes the form:

$$\bar{\mathcal{G}} = \mathcal{G}_{\mathrm{c}} = \mathcal{G}_{\mathrm{Ic}} \left(1 + \tan^2\left(\frac{\chi}{2}\right)\right). \tag{4.20}$$

Using asymptotics, the ratio of shear and normal stresses along the material interface prior to fracture is given by:

$$\frac{\tau_{\mathrm{nt}}}{\sigma_{\mathrm{nn}}} = \frac{K_1 r^{\lambda_1} \tau_{r\varphi,1}}{K_1 r^{\lambda_1} \sigma_{\varphi\varphi,1}} = 0.33. \tag{4.21}$$

This corresponds to a mixed-mode angle of $\chi = \tan^{-1}(\tau_{\mathrm{nt}}/\sigma_{\mathrm{nn}}) \approx 18°$. Substituting this result in Eq. (4.20) finally yields a 2.7% increase in fracture toughness compared to the mode I fracture toughness:

$$\mathcal{G}_{\mathrm{c}} = 1.027\, \mathcal{G}_{\mathrm{Ic}}. \tag{4.22}$$

On account of relation (4.15), it follows directly that changing the fracture toughness from $\mathcal{G}_{\mathrm{Ic}}$ to $\mathcal{G}_{\mathrm{c}}$ according to the mixed-mode criterion results in the following modified failure stress $\tilde{\sigma}_{\mathrm{f}}$:

$$\tilde{\sigma}_{\mathrm{f}} = \sigma_{\mathrm{f}} \left(\frac{\mathcal{G}_{\mathrm{c}}}{\mathcal{G}_{\mathrm{Ic}}}\right)^{1-\lambda_1} = 1.008\sigma_{\mathrm{f}}. \tag{4.23}$$

Equation (4.23) has two implications: Firstly, taking into account the effect of mixed-mode conditions on fracture toughness results in a 0.8% increase in failure stress compared to solely using $\mathcal{G}_{\mathrm{Ic}}$. Consequently, a mixed-mode energy criterion only has a small effect for mixed-mode angles smaller than 20°. Secondly, Eq. (4.23) in fact represents a scaling law characterising how the failure stress scales with the fracture toughness. It follows, that changing the fracture toughness only has a sub-linear effect on the failure stress[17]. More precisely, in the case of a steel-epoxy joint with $\lambda_1 = 0.7$ doubling the fracture toughness of the epoxy would lead to a 23% increase in the joint's failure stress. It is the semi-analytical nature of the asymptotic approach that unveils such scaling laws, which are extremely valuable for a physically sound understanding of the failure behaviour and engineering considerations such as sensitivity analyses and the assessment of uncertainties.

[17]Note that $\lambda_1 > 0$ is a general restriction and thus leads to sub-linear scaling.

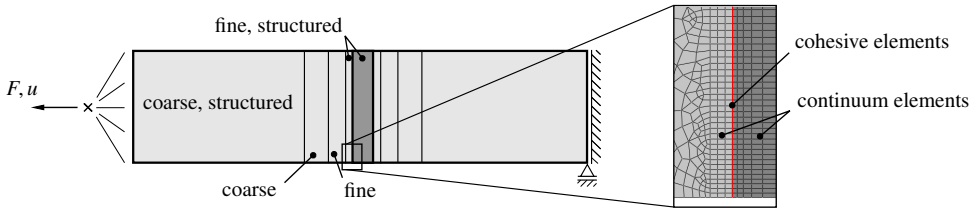

Figure 4.8: Finite element model of the butt joint using CZM with partitioning of the mesh. A zoom with an enlarged detail of the mesh focusing on the location where crack onset is prone to occur is provided.

4.2.4 Comparing asymptotic predictions against cohesive zone model

For validation purpose, numerical reference solutions employing ABAQUS and its embedded Cohesive Zone Model (CZM) formulation are employed. Cohesive zone modelling is an established technique in terms of simulating fracture in adhesive joints (da Silva and Campilho, 2012) and is often used for a detailed assessment of novel predictive approaches (Stein et al., 2015, Rosendahl et al., 2017, Martin et al., 2016). Moreover, the ABAQUS standard cohesive zone implementation has proven to be in a very good agreement with experimental data of adhesively bonded joints (Campilho et al., 2013, 2009) and thus serves as a reliable reference solution for the asymptotic failure model. Within cohesive zone modelling, crack initiation and growth along a predefined path is simulated by means of a non-linear traction separation law. The traction separation law yields an elastic response up to a certain point of damage initiation followed by a progressive damage evolution. However, careful modelling is needed for an accurate and realistic failure prediction since additional numerical parameters such as the characteristic cohesive element length and a viscous regularization parameter to control convergence issues have to be adequately identified.

The finite element model employed in the present study is a full model of the butt joint. For the adhesive and adherends, continuum plane strain elements (CPE4) are used and the models have approximately 3×10^5 degrees of freedom. Displacement controlled loading is considered to avoid numerical difficulties using constant far-field stresses that would yield infinite displacements at failure. Zero-thickness cohesive zone elements based on a bi-linear traction-separation law are employed and placed at the material interface of adhesive and adherend, cf. Fig. 4.8. In order to eliminate any change in the global structural stiffness, the initial elastic stiffness of the cohesive zone elements is set to $10^7\,\mathrm{N/mm^2}$ following the recommendation of Gonçalves et al. (2000). Using CZM, the point of damage initiation is governed by a stress criterion. Here, the quadratic interaction law as used within the CC is used. If the stress criterion is fulfilled, a linear degradation of the element stiffness initiates and a complete debonding is predicted if an energy criterion is satisfied. The load at crack onset and hence the failure load is defined as the peak load in the load-displacement curve of the numerical simulation. The non-physical numerical parameters, that is, the viscous regularization parameter χ_{reg} and the cohesive element size l_{cz} are determined based on convergence studies for each structural situation. Results for an exemplary butt joint configuration are shown in Fig. 4.9. Based on a convergence argument, these findings indicate that a cohesive

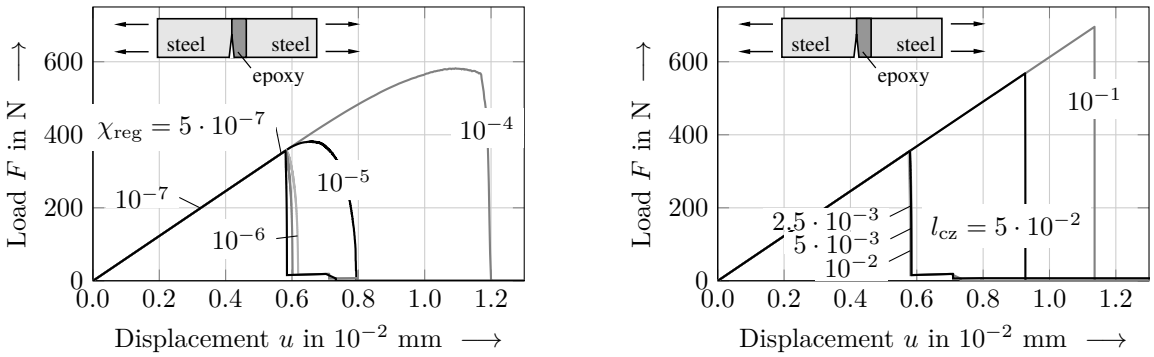

(a) Effect of dimensionless viscous damping parameter χ_{reg}.

(b) Effect of cohesive element size l_{cz} measured in mm.

Figure 4.9: Convergence studies addressing the impact of the viscous regularization parameter χ_{reg} and the cohesive element size l_{cz} on the failure load F_{f}.

element size of $l_{\text{cz}} = 5 \cdot 10^{-3}\,\text{mm}$ and a regularization parameter $\chi_{\text{reg}} = 10^{-7}$ provide reliable numerical data so that results are not affected by χ_{reg} and l_{cz}, respectively. Turon et al. (2007) proposed a lower bound of the cohesive zone length depending only on material parameters of the adhesive,

$$l_{\text{cz,low}} = \frac{E_2 \mathcal{G}_c}{\sigma_{\text{c}}^2}, \tag{4.24}$$

which attains a value of $l_{\text{cz,low}} = 0.012\,\text{mm}$ for the considered epoxy. Consequently, using two elements within the cohesive zone suffices in the present case. This result agrees with the findings by Falk et al. (2001) and Davila et al. (2001) indicating that the use of two or three elements in the cohesive zone is recommended to obtain accurate failure predictions. Note that the defined cohesive zone length is proportional to the crack length derived with the asymptotic evaluation of the CC, cf. Eq. (4.16).

Having adequate values for the regularization parameter and the cohesive element size at hand, let us compare the CZM predictions with results based on the CC using the explicit relation (4.15). Figure 4.10 shows the predicted joint strength with respect to the adhesive thickness for a steel-epoxy joint, cf. Fig. 4.10(a), and an aluminum-epoxy joint, cf. Fig. 4.10(b), respectively. From a qualitative perspective, both approaches are in a very good agreement showing a decreasing joint strength with increasing adhesive thickness. Note that calculations using CZM are non-linear in nature and one simulation can take up to one hour. This underlines the efficiency of the asymptotic approach, where the failure load is given explicitly. It is observed, that the CZM yields slightly lower failure stresses compared to the CC. The maximum relative error between both models is approximately 12%. Previous studies have shown, that the shape of the employed traction separation law affects the prediction of crack initiation (Acary and Monerie, 2005, Vandellos et al., 2014, Martin et al., 2016). More precisely, Rosendahl et al. (2017) pointed out that a trapezoidal, tri-linear traction separation law is well

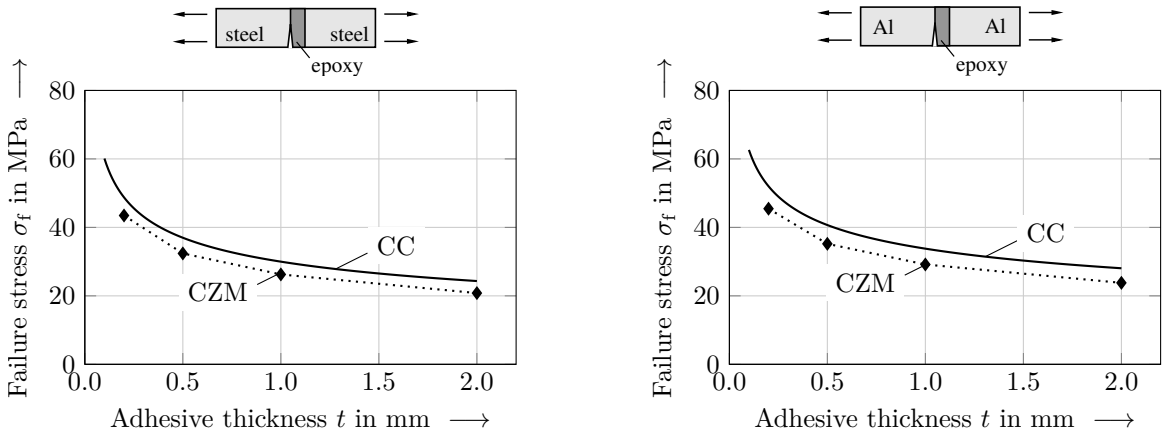

(a) Steel-epoxy butt joint.

(b) Aluminum-epoxy butt joint.

Figure 4.10: Comparison of predictions calculated with the asymptotic approach using Eq. (4.15) against numerical reference solutions employing CZM.

suited for brittle fracture and leads to higher failure loads which are closer to the predictions based on the CC. However, since implementing a trapezoidal law in Abaqus is not straightforward and is accompanied by a significant increase in computational time, this approach is not followed in this work.

4.2.5 Comparison of failure predictions and experimental findings

The theoretical failure predictions according to Eq. (4.15) are compared against experimental data from literature. Experimental results are based on the test series performed by Reedy and Guess (1997) addressing the impact of adhesive thickness t on the effective joint strength. Stainless-steel-adhesive butt joint as well as aluminum-adhesive joints with the dimensions $l = 66.2$ mm, $w = 28.6$ mm and $t = 0.25, 0.5, 1, 2$ mm are investigated. This additionally allows for assessing the impact of the elastic mismatch between adhesive and adherend on the failure stress. The brittle adhesive is a triamine-cured DGEBA epoxy (Shell Epon 828 epoxy resin with a Huntsman T403 hardener) whose material properties are given in Table A.1. After testing, all joints showed an adhesive failure, that is, crack nucleation occurs at a small segment along the material interface resulting in a separation of adhesive and adherend. This suggests employing strength and toughness in form of interface properties in the failure model. However, this is accompanied by the major drawback that interface properties have to be adapted for every combination of adhesive and adherend, cf. Martin et al. (2010), Reedy and Guess (1997). In order to obtain a simple and predictive model, the approach of using bulk material properties of the adhesive is followed as a first-order approximation. This allows for using the standard material data according to the adhesive data sheet and hence enables the applicability of the failure model to a wide range of adhesive joints. Furthermore, this approach has been successfully applied to adhesively bonded

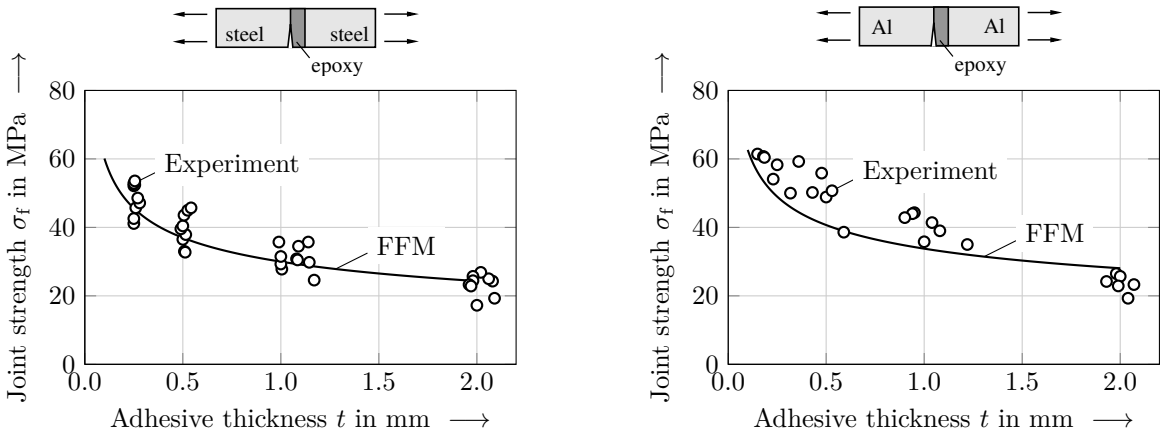

(a) Steel-epoxy butt joint.

(b) Aluminum-epoxy butt joint.

Figure 4.11: Comparison of predictions according to the asymptotic approach against experimental data from literature (Reedy and Guess, 1997).

joints in former studies (Hell et al., 2014, Weißgraeber and Becker, 2013, Stein et al., 2015).

A comparison between predictions and experimental data is given in Fig. 4.11. Despite some scatter, the measured joint strength σ_f decreases with increasing adhesive thickness which is captured correctly by the present failure model. In case of steel adherends as depicted in Fig. 4.11(a), the mean absolute percentage error (MAPE) between the predicted and measured failure stress equals 9.3%. Figure 4.11(b) shows the stress at failure for an aluminum-epoxy joint configuration. Since the stresses along the interface, cf. Fig. 4.5(a), as well as the IERR, cf. 4.6(b), are smaller compared to the steel-epoxy joint, the predicted joint strength increases. This prediction agrees well with the experiments, however, the MAPE increases to 15.1% and the prediction accuracy has slightly decreased compared to the steel-epoxy configuration. One reason for this might be that neglected interface properties play a more dominant role for the aluminum-epoxy joint.

4.3 Failure of a T-structure under uniform tensile loading

In this section, fracture initiation at a 90° re-entrant corner of a T-shaped structure as depicted in Fig. 4.12(a) is investigated. The T-structure is subjected to uniaxial tensile loading σ_∞ and its geometry is characterised by the widths w_1 and w_2, respectively. The dimensions in horizontal direction are large compared to any other length involved. The specimens were machined from polymethyl methacrylates (PMMA), see Table A.1 for material data, and the failure of the specimens can be considered as brittle. Although uniaxial loading is applied, the re-entrant corner is loaded in mixed-mode I and II. Thus, the angle θ at which crack onset occurs is a-priori unknown, cf. Fig. 4.12(b). Dunn et al. (1997c) employed a critical GSIF approach to assess the structural integrity

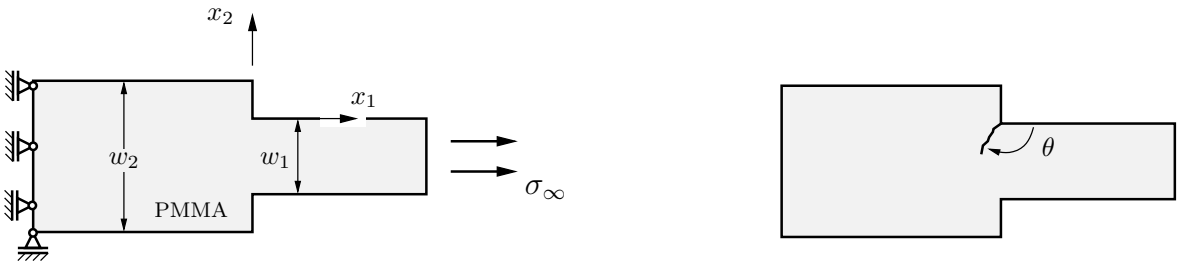

(a) Uncracked T-structure configuration. **(b)** Crack angle θ.

Figure 4.12: T-structure specimen made of PMMA under uniform tensile loading σ_∞ as used by Dunn et al. (1997c). Geometric parameters: width w_1 and w_2.

of the T-structure. Although the predicted failure loads agree with experimental data, there is no prediction of the resulting crack angle. Furthermore, there is no rigorous connection between the GSIF and the energy release rate of fracture mechanics[18], hence the physical meaning of this criterion is unclear. Moreover, the identified critical GSIF does not represent a material parameter since it is affected by the local notch geometry, cf. Dunn et al. (1997a).

In the subsequent analysis, the CC is used to predict failure of the T-specimen. In the case of a 90° corner, two singular modes characterised by the singularity exponents λ_1 and λ_2, respectively, are present and trigger crack nucleation. The associated GSIFs are determined in dependence of w_1 and w_2 by means of the Ψ-integral. Subsequently, the scaling coefficients Ψ_{ij} are calculated to determine the IERR for different crack configurations. Having all involved asymptotic expansions at hand, the CC can be evaluated efficiently and the predictions in terms of failure load and crack angle are compared to experimental findings presented in Dunn et al. (1997c).

4.3.1 The local notch-tip stress field

In order to determine the singularity exponents and associated eigenfunctions, the eigenvalue problem as defined in Eqn. (3.7)-(3.8) is solved. For the case of a homogeneous 90° corner with stress-free boundary conditions along the notch faces the eigenvalue problem reads:

$$\mathbf{D}\underline{a}_i = \begin{pmatrix} e^{\frac{3\mathrm{i}\pi\lambda}{2}} & -\mathrm{i}\lambda & 0 & 1 \\ \mathrm{i}\lambda & e^{-\frac{3\mathrm{i}\pi\lambda}{2}} & 1 & 0 \\ e^{-\frac{3\mathrm{i}\pi\lambda}{2}} & \mathrm{i}\lambda & 0 & 1 \\ -\mathrm{i}\lambda & e^{\frac{3\mathrm{i}\pi\lambda}{2}} & 1 & 0 \end{pmatrix} \begin{pmatrix} A_{1i} \\ \overline{A}_{1i} \\ A_{2i} \\ \overline{A}_{2i} \end{pmatrix}. \tag{4.25}$$

[18]Only for the limiting case of a crack, there is a relation between stress intensity factor and energy release rate.

The corresponding characteristic equation $\det(\mathbf{D}) = 0$ writes:

$$-1 + 2\lambda^2 + \cos(3\pi\lambda) = 0. \tag{4.26}$$

Solving this equation numerically yields two exponents $\lambda_1 = 0.544$ and $\lambda_2 = 0.909$ which are associated to singular stresses at the notch tip. In the asymptotic expansion of the stress field, both singular terms are considered:

$$\boldsymbol{\sigma}(r,\varphi) \sim K_1 r^{\lambda_1 - 1}\boldsymbol{\sigma}_1(\varphi) + K_2 r^{\lambda_2 - 1}\boldsymbol{\sigma}_2(\varphi) \quad \text{as} \quad r \to 0. \tag{4.27}$$

The GSIFs K_1 and K_2 depend on the loading as well as on the geometry of the structure. In the present case, it follows:

$$K_1 = f_1(\sigma_\infty, w_1, w_2), \tag{4.28}$$
$$K_2 = f_2(\sigma_\infty, w_1, w_2). \tag{4.29}$$

Applying dimensional analysis, this can be rewritten in the dimensionally correct form:

$$K_1 = \sigma_\infty\, w_1^{1-\lambda_1}\hat{K}_1\left(\frac{w_1}{w_2}\right), \tag{4.30}$$
$$K_2 = \sigma_\infty\, w_1^{1-\lambda_2}\hat{K}_2\left(\frac{w_1}{w_2}\right). \tag{4.31}$$

The dimensionless functions $\hat{K}_1$ and $\hat{K}_2$ depend only on the ratio of w_1 and w_2 and are calculated employing the Ψ-integral. A finite element model of the T-structure is generated using continuum plane stress elements (CPS4). In the numerical model, the width w_1 is set equal to unity and a unit loading is applied. Having the solutions $\underline{u}^{\mathrm{FE}}$ at hand, the dimensionless GSIFs are calculated according to

$$\hat{K}_1 = \frac{\Psi\left(\underline{u}^{\mathrm{FE}}, r^{-\lambda_1}\underline{u}_{-1}(\varphi)\right)}{\Psi\left(r^{\lambda_1}\underline{u}_1(\varphi), r^{-\lambda_1}\underline{u}_{-1}(\varphi)\right)}, \qquad \hat{K}_2 = \frac{\Psi\left(\underline{u}^{\mathrm{FE}}, r^{-\lambda_2}\underline{u}_{-2}(\varphi)\right)}{\Psi\left(r^{\lambda_2}\underline{u}_2(\varphi), r^{-\lambda_2}\underline{u}_{-2}(\varphi)\right)}. \tag{4.32}$$

The resulting values for $\hat{K}_1$ and $\hat{K}_2$ are shown in Fig. 4.13 with respect to the dimensionless ratio w_1/w_2. It is observed, that mixed mode conditions are changing with w_1/w_2. While the mode I contribution decreases for an increasing w_1/w_2 ratio the mode II contribution increases. The resulting stress distribution in the close vicinity of the re-entrant corner is plotted in Fig. 4.14 for $w_1/w_2 = 1/3$. Stresses are evaluated at a radial distance $r = 0.025w_1$ and the effect of taking mixed-mode conditions into account is examined. Figure 4.14(a) shows the normalised circumferential stress $\sigma_{\varphi\varphi}/\sigma_\infty$ with respect to the angle $\tilde{\varphi}$ counting positive in clockwise direction. The solid lines represent the asymptotic stress solution associated to the leading-order term (mode I) as well as to the combination of first and second-order terms (mode I+II), respectively. It is observed that the two-term asymptotic series is in a very good agreement with the numerical reference solution. The circumferential stress takes a maximum value at an angle $\tilde{\varphi} \approx 120°$. Hence, the mixed-mode conditions yield a shift of the point of maximum stress to a smaller value of $\tilde{\varphi}$ compared to a pure mode I solution (maximum

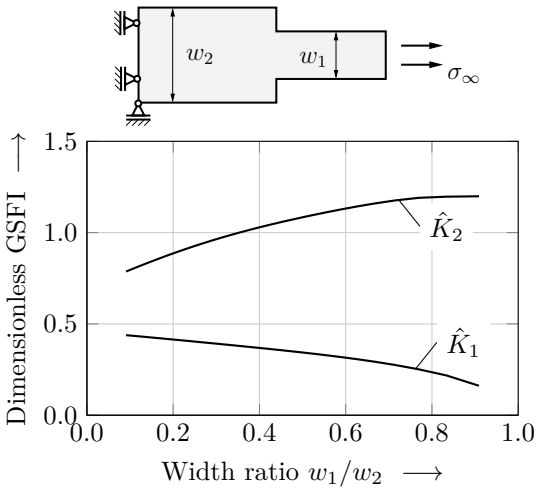

Figure 4.13: Dimensionless generalised stress intensity factors $\hat{K}_1$ and $\hat{K}_2$ with respect to the width ratio w_1/w_2 for the T-structure under uniform tensile loading.

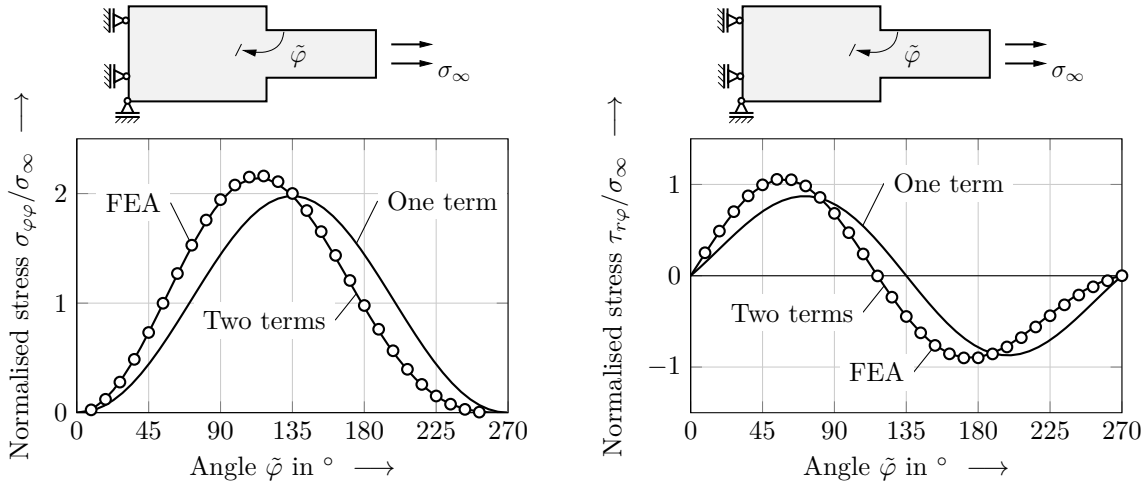

(a) Circumferential stresses.

(b) Shear stresses.

Figure 4.14: Comparison of asymptotic stress field and numerical reference data based on FEA. Stresses are evaluated at a radial distance $r = 0.025w_1$ and are plotted with respect to the angle $\tilde{\varphi}$. Geometry: $w_1/w_2 = 1/3$.

at 135°). An analogous effect is observed for the shear stresses as plotted in Fig. 4.14(b). This already indicates, that potential cracks initiate at an angle θ smaller than 135° as it would be the case for pure mode I conditions. Besides the stresses, the IERR also affects the process of crack formation and the angle at which crack onset occurs which is addressed in the next section.

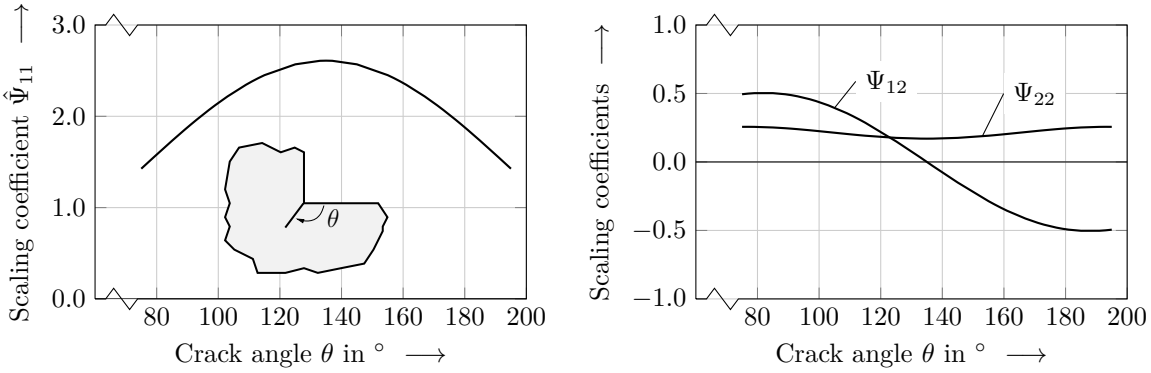

(a) Scaling coefficient $\hat{\Psi}_{11}$.

(b) Scaling coefficients $\hat{\Psi}_{12}, \hat{\Psi}_{22}$.

Figure 4.15: Numerical dimensionless scaling coefficients $\hat{\Psi}_{ij}$ for a 90° re-entrant corner with variable crack angle θ.

4.3.2 Asymptotics of the incremental energy release rate

In case of the T-structure, the IERR rate depends on the lengths w_1, w_2, the crack length Δa, the crack angle θ, the loading σ_∞ as well as on material parameters. This can be generally written as:

$$\bar{\mathcal{G}} = \frac{\sigma_\infty^2 \, w_1}{E} \, \hat{\bar{\mathcal{G}}} \left(\frac{\Delta a}{w_1}, \frac{w_1}{w_2}, \theta, \nu \right). \tag{4.33}$$

Using asymptotics, two singular terms corresponding to a mode I and a mode II contribution are included in the expansion of the stresses. Consequently, higher-order terms enter the expansion of the IERR as well. Employing the general results of Eq. (3.60) for the special case of two real-valued exponents λ_1 and λ_2 it follows:

$$\begin{aligned} \bar{\mathcal{G}} \sim \frac{\sigma_\infty^2 \, w_1}{E} \Bigg[& \hat{K}_1 \left(\frac{w_1}{w_2} \right)^2 \left(\frac{\Delta a}{w_1} \right)^{2\lambda_1 - 1} \hat{\Psi}_{11}(\theta) \\ & + 2 \hat{K}_1 \left(\frac{w_1}{w_2} \right) \hat{K}_2 \left(\frac{w_1}{w_2} \right) \left(\frac{\Delta a}{w_1} \right)^{\lambda_1 + \lambda_2 - 1} \hat{\Psi}_{12}(\theta) \\ & + \hat{K}_2 \left(\frac{w_1}{w_2} \right)^2 \left(\frac{\Delta a}{w_1} \right)^{2\lambda_2 - 1} \hat{\Psi}_{22}(\theta) \Bigg] \quad \text{as} \quad \Delta a \to 0. \end{aligned} \tag{4.34}$$

The involved dimensionless scaling coefficients $\hat{\Psi}_{ij}$ depend on the local notch geometry and hence on the crack angle θ. Note that the scaling coefficients neither depend on the loading conditions of the structure nor on w_1 and w_2 representing global, macroscopic length scales. Thus, the $\hat{\Psi}_{ij}$ are computed once for all and can be employed for a variety of problems that are characterised by a 90° re-entrant corner. Since θ is a-priori unknown, the coefficients must be determined for all admissible crack angles. It is assumed, that crack onset takes place at the upper corner as illustrated in Fig. 4.12(b),

thus the crack angle can attain values between 0° and 270°. The coefficients $\hat{\Psi}_{ij}$ are calculated numerically solving the corresponding inner problems according to Eq. (3.28) and results are shown in Fig. 4.15. The coefficient $\hat{\Psi}_{11}$ is plotted in Fig. 4.15(a) and displays a symmetric behaviour in terms of θ with an axis of symmetry at 135°, that is, the direction of the crack coincides with the axis of symmetry of the local notch configuration. According to the leading-order term, the IERR is maximised for $\theta = 135°$. The coefficients $\hat{\Psi}_{12}$ and $\hat{\Psi}_{22}$ are depicted in Fig. 4.15(b). It is observed, that $\hat{\Psi}_{22}$ also possesses a symmetric behaviour whereas $\hat{\Psi}_{12}$ is antisymmetric. Accounting for the fact that the intensity factors $\hat{K}_1$ and $\hat{K}_2$ attain positive values in the present situation, cf. Fig. 4.13, it follows that the IERR will take its maximum value for crack angles smaller than 135°. This is analogous to the characteristics of the stress distribution in Fig. 4.14. Thus, before ultimately evaluating the CC, cracks are anticipated to initiate at an angle $\theta < 135°$.

4.3.3 Failure predictions and experimental validation

After the asymptotic representation of stresses in Eq. (4.27) and the IERR in Eq. (4.34) are fully determined, the CC is ready to be evaluated and the crack angle θ enters the optimisation problem as an additional parameter. Since the stresses as well as the IERR are monotonic functions the optimisation problem reads:

$$\sigma_{\mathrm{f}} = \min_{\sigma_\infty, \Delta a, \theta} \left\{ \sigma_\infty \;\middle|\; g\left(\boldsymbol{\sigma}\left(\Delta a, \theta\right)\right) = 1 \quad \wedge \quad \bar{\mathcal{G}}(\Delta a, \theta) = \mathcal{G}_{\mathrm{Ic}} \right\}. \tag{4.35}$$

The quadratic interaction law in Eq. (2.66) is used as stress criterion and the simple energy criterion $\bar{\mathcal{G}} = \mathcal{G}_{\mathrm{Ic}}$ is employed. Since the mixed-mode angle is small, an effect of mixed-mode conditions on the fracture toughness is negligible. In order to compute the three unknowns, that is, the failure stress σ_{f}, the crack length Δa and the crack angle θ, the optimisation problem is solved as follows: the failure load and corresponding crack length are calculated in terms of θ. Subsequently, the failure load is minimised with respect to θ and the angle associated to the smallest failure stress eventually determines the final crack configuration. For validation purpose the predictions are compared to experimental data obtained by Dunn et al. (1997c). The employed specimens are made of PMMA with Young's modulus $E = 2.3$ GPa, Poisson's ratio 0.36 and tensile strength $\sigma_{\mathrm{c}} = 68.9$ MPa. The specimens are 100 mm long and the widths are given by $w_2 = 50.8$ mm and $w_1 = 5.08, 10.16, 15.24, 20.32$ mm, respectively. This corresponds to $w_1/w_2 = 0.1, 0.2, 0.3, 0.4$. The observed load-displacement curves showed a linear response eventually followed by brittle fracture.

The far-field stress at failure σ_{f} is shown in Fig. 4.16(a) with respect to w_1/w_2 and both solid lines represent the prediction of the CC. The grey line corresponds to material data given above[19] whereas the black line is related to material data from Seweryn et al. (1997), cf. Table A.1. In accordance with experiments, the predicted failure stress increases while decreasing the ratio w_1/w_2 from about 0.5 towards 0. Employing the

[19] No value for the fracture toughness is provided by Dunn et al. (1997c) and the missing data has been adopted from Seweryn et al. (1997).

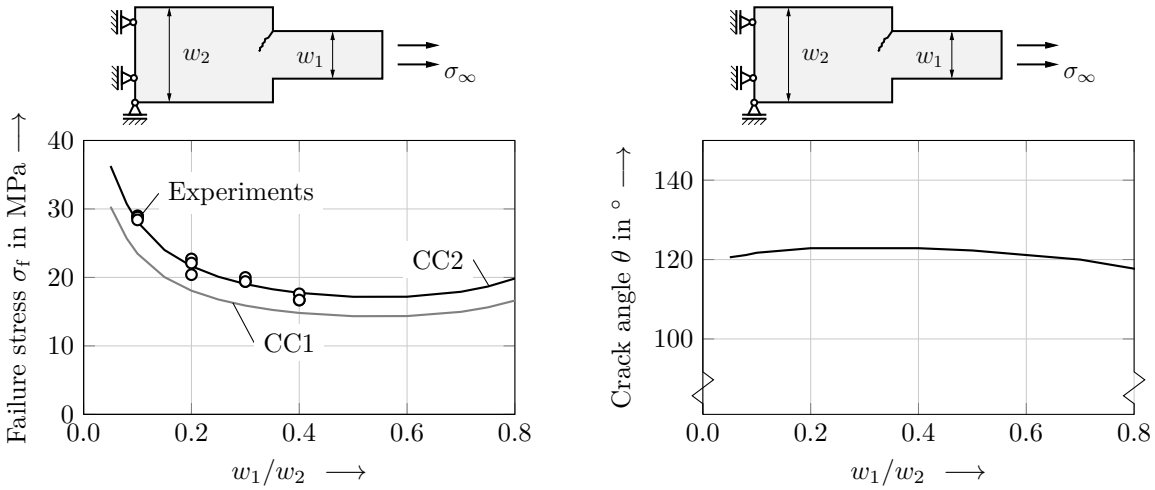

(a) Failure stress σ_f.

(b) Crack angle θ.

Figure 4.16: Failure of a T-structure under uniaxial tensile loading for a varying width ratio w_1/w_2. Comparison between predictions of the CC and experimental results by Dunn et al. (1997c). Geometry: $w_2 = 50.8$, $w_1/w_2 = 0.1, 0.2, 0.3, 0.4$. Material data: CC1 according to Dunn et al. (1997c), CC2 according to Seweryn et al. (1997).

material data of Seweryn et al. (1997), the predictions are in a very good agreement with the experimental data from a qualitative and quantitative point of view and a MAPE of 3.5% is achieved. For the limiting case of $w_1/w_2 = 1$, the T-structure degenerates into an unnotched tensile bar and the resulting failure load σ_f approaches the uniaxial tensile strength of the material. Thus, the effective strength at $w_1/w_2 \approx 0.5$ represents a minimum. Although the predictions are not validated experimentally over the entire range $0 < w_1/w_2 < 1$, it can be deduced that configurations with $w_1/w_2 \approx 0.5$ do not represent favourable structural designs from an engineering point of view and should be avoided as far as possible. The predicted angle θ at which cracks nucleate is shown in Fig. 4.16(b). As already anticipated by the distribution of the stresses and the IERR, the crack angle θ is smaller compared to a pure mode I scenario ($\theta = 135°$) and is roughly constant with respect to w_1/w_2. According to experimental observations, cracks initiate at an angle $\theta \approx 114°$ and subsequently grow towards the other notch which is in a fair agreement with the predictions.

4.4 Failure of a scarf-joint under four-point bending loading

In this section, a scarf-joint under four-point bending loading is considered as depicted in Fig. 4.17. The effect of the material interface orientation on the failure behaviour and the effective joint strength is examined. In some sense, the scarf-joint combines the features of the butt joint considered in Section 4.2 and the T-structure investigated in Section 4.3: it represents a bi-material configuration where the angle of crack initiation is a-priori unknown. Additionally, a competition between two failure scenarios associated

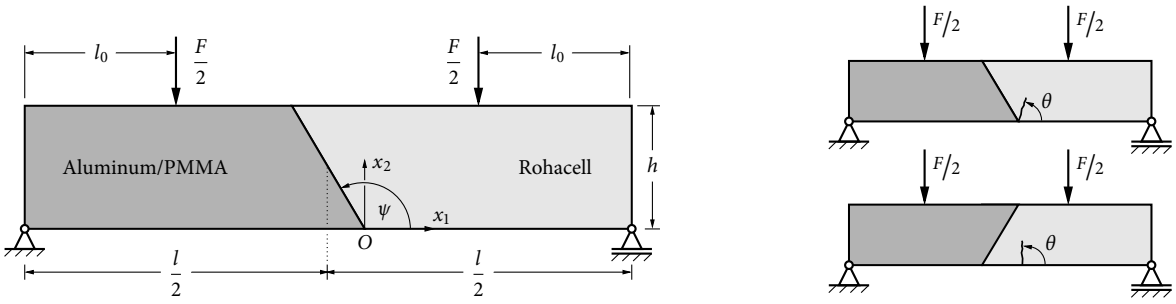

(a) Uncracked scarf joint configuration with interface angle ψ, height $h = 40$ mm, out-of-plate thickness $d = 40$ mm and lengths $l_0 = 150$ mm, $l = 445$ mm.

(b) Sketch of possible crack configurations with initiation angle θ.

Figure 4.17: Bi-material scarf joint under four-point bending loading with aluminum or PMMA adherend on the left-hand side and a Rohacell adherend on the right-hand side as used by Ribeiro-Ayeh and Hallström (2003).

to different locations of crack nucleation is observed as sketched in Fig. 4.17(b): a notch induced failure and a bending failure mode. In case of bending failure characterised by crack onset in a certain distance away from the bi-material point, the CC is evaluated analytically. In case of notch induced failure, crack formation is triggered by the singularity at the bi-material notch. Since the angle at which crack onset occurs is unknown, the asymptotic modelling approach is suitable and reduces the numerical effort significantly. In addition to a first-order asymptotic solution, higher-order terms associated to complex singularity exponents are considered. This extends the range of validity of the asymptotic approximation and thus improves accuracy. Furthermore, an iterative numerical evaluation of the CC is performed serving as a reference solution for the asymptotic approach. The predicted failure load, crack length and crack initiation angle are discussed in detail and theoretical results are compared to experimental findings by Ribeiro-Ayeh and Hallström (2003).

The considered scarf joint consists of a Rohacell 51 foam typically used in sandwich structures and an aluminium or a PMMA adherend. The related material data can be found in Table A.1. All materials are assumed to be linear elastic and isotropic. Furthermore, the foam is modelled as a homogeneous continuum with effective macroscopic material properties. A two-dimensional plane-strain model of the joint is employed implying through-thickness cracks. Further, a perfectly bonded interface between both constituents is presumed and the interface orientation is characterised by the angle ψ, cf. Fig. 4.17(a). The elastic contrast between both adherends induces a localised stress concentration with mathematically infinite stresses at the bi-material point O. Hence, it is reasonable to assume that cracks emanate from O as depicted in the upper part of Fig. 4.17(b). In addition, a physically sound restriction is that only cohesive failure of Rohacell occurs. That is, no crack nucleation takes place in the other adherend possessing significantly higher material strength and fracture toughness, or along the interface revealing good adhesion properties as confirmed by tests conducted by Ribeiro-Ayeh and Hallström (2003). This implies that the sector of admissible crack

configurations becomes narrower with a decreasing interface angle. This constraint, however, may lead to crack formation in a certain distance away from the bi-material point as depicted at the bottom of Fig. 4.17(b). The scenario which ultimately occurs is associated to the smallest failure load F_f given by:

$$F_\mathrm{f} = \min_{F,\Delta a,\theta,\underline{\xi}} \left\{ F \;\middle|\; g\left(\boldsymbol{\sigma}\left(\underline{x}_\mathrm{ct}\right)\right) = 1 \quad \wedge \quad \bar{\mathcal{G}}(\Delta a, \theta) = \mathcal{G}_\mathrm{Ic} \right\}. \tag{4.36}$$

Note that the a priori unknown location of crack initiation denoted by $\underline{\xi}$ enters the formulation of the optimisation problem. The coordinate of the crack tip is denoted by x_ct. As stress criterion, the quadratic interaction law based on Eq. (2.66) is used.

4.4.1 Bending failure of the joint

In the case of small interface angles ψ, experiments reveal that cracks nucleate vertically at a finite distance away from the interface well within the Rohacell, cf. Fig. 4.17(b). This failure scenario is subsequently referred to as bending failure. The simplest approach to model bending failure in the present four-point bending setup is to assume a single homogeneous Rohacell beam of length $l = 145$ mm subjected to pure bending loading at its ends. In this case, both stress solution and energy release rate are readily available. Since no shear stresses are present along the potential crack path, the stress criterion evaluated in the uncracked state reads:

$$\sigma_\mathrm{c} = \sigma_{11}(x_2 = \Delta a), \tag{4.37}$$

with

$$\sigma_{11}(x_2) = \sigma_\mathrm{E}\left(1 - \frac{2x_2}{h}\right). \tag{4.38}$$

The beam edge stress is denoted by σ_E and is given by

$$\sigma_\mathrm{E} = 3\frac{F l_0}{d h^2}. \tag{4.39}$$

Further, F and l_0 are the four-point bending rig force load and its lever, respectively, d is the beam's out-of-plane thickness and h its height, cf. Fig.4.17(a). The energy criterion is formulated by means of the mode I stress intensity factor K_I:

$$K_\mathrm{Ic}^2 = \frac{1}{\Delta a}\int_0^{\Delta a} K_\mathrm{I}^2(a)\,\mathrm{d}a. \tag{4.40}$$

In the present case, the stress intensity factor of an edge crack with length a in a finite-width plate subjected to bending loading is employed:

$$K_\mathrm{I}(a) = \sigma_\mathrm{E}\sqrt{\pi a}\; g\left(\frac{a}{h}\right). \tag{4.41}$$

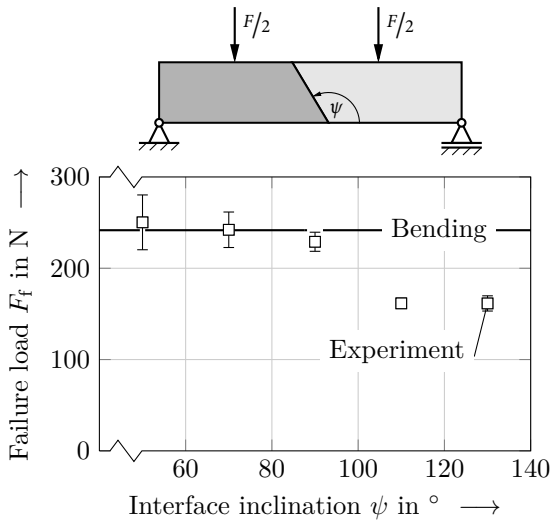

Figure 4.18: Four-point bending failure loads F_f of aluminum–Rohacell scarf joints with bending failure load predictions according to the CC in dependence of the scarf angle ψ.

The corresponding empirical formula for $g(a/h)$ is given in Tada et al. (2000),

$$g\left(\frac{a}{h}\right) = 1.122 - 1.40\left(\frac{a}{h}\right) + 7.33\left(\frac{a}{h}\right)^2 - 13.08\left(\frac{a}{h}\right)^3 + 14.0\left(\frac{a}{h}\right)^4, \tag{4.42}$$

with a relative error of 0.2% for $a/h \leq 0.6$. Since both stress and IERR change monotonically with increasing distance from the free-edge, the CC simplifies to a single equation dividing Eq. (4.40) by the square of Eq. (4.37):

$$\frac{\dfrac{1}{\Delta a}\displaystyle\int_0^{\Delta a} \pi a\; g\left(\frac{a}{h}\right)^2 \mathrm{d}a}{\left(1 - \dfrac{2\Delta a}{h}\right)^2} = \left(\frac{K_\mathrm{Ic}}{\sigma_\mathrm{c}}\right)^2. \tag{4.43}$$

Equation (4.43) can be solved directly for its only unknown Δa and the corresponding failure load F_f is obtained from either Eq. (4.37) or Eq. (4.40).

In Fig. 4.18 predictions of the CC in case of bending failure are compared against four-point bending test results for different scarf angles. As a result of the homogeneous beam assumption, the predicted failure load F_f is independent of the scarf angle. For joints with a sufficiently small interface angle ψ the present model provides very good failure predictions compared to the experimental data. For interface angles up to $\approx 80°$, the measured failure load seems to be unaffected by the interface orientation. This supports that the simplifying assumption of a pure bending failure holds and represents an admissible approximation. For angles $\geq 90°$ the sustained loads deviate increasingly from the predictions. In this domain, failure is triggered by the bi-material notch which is discussed in the following.

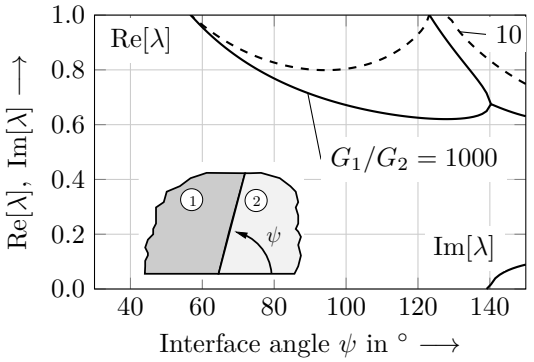

Figure 4.19: Singularity exponent λ corresponding to the bi-material notch configuration of the scarf joint with respect to the interface angle ψ.

4.4.2 Asymptotic approach for notch induced failure

Besides the above-mentioned bending failure, cracks may also emanate from the bi-material notch, that is the point where the interface intersects the free surface. In this case, crack formation is governed by the singular stress field in the close vicinity of the bi-material point. Thus, the asymptotic approach is employed to describe the stress distribution at the notch as well as the IERR for small cracks. The first step is to calculate the eigenvalues and eigenvectors related to the specific notch configuration. The corresponding coefficient matrix $\mathbf{D}$ reads:

$$\mathbf{D} = \begin{pmatrix} 1 & e^{-2i\psi(\lambda-1)}\lambda & 0 & e^{-2i\psi\lambda} & -1 & -e^{-2i\psi(\lambda-1)}\lambda & 0 & -e^{-2i\psi\lambda} \\ \lambda & e^{-2i\psi(\lambda-1)} & e^{2i\psi} & 0 & -\lambda & -e^{-2i\psi(\lambda-1)} & -e^{2i\psi} & 0 \\ \kappa_1 & -e^{-2i\psi(\lambda-1)}\lambda & 0 & -e^{-2i\psi\lambda} & -\kappa_2\hat{G} & e^{-2i\psi(\lambda-1)}\lambda\hat{G} & 0 & e^{-2i\psi\lambda}\hat{G} \\ -\lambda & e^{-2i\psi(\lambda-1)}\kappa_1 & -e^{2i\psi} & 0 & \lambda\hat{G} & -e^{-2i\psi(\lambda-1)}\kappa_2\hat{G} & e^{2i\psi}\hat{G} & 0 \\ 1 & -e^{-i\pi\lambda}\lambda & 0 & e^{-i\pi\lambda} & 0 & 0 & 0 & 0 \\ \lambda & -e^{-i\pi\lambda} & -1 & 0 & 0 & 0 & 0 & 0 \\ 0 & 0 & 0 & 0 & 1 & -e^{-i\pi\lambda}\lambda & 0 & e^{-i\pi\lambda} \\ 0 & 0 & 0 & 0 & \lambda & -e^{-i\pi\lambda} & -1 & 0 \end{pmatrix}. \tag{4.44}$$

Here, $\tilde{G} = G_1/G_2$ denotes the shear modulus ratio between both constituents. The singularity exponents satisfying the characteristic equation $\mathrm{Det}\,(\mathbf{D}) = 0$ are plotted in Fig. 4.19 with respect to the angle ψ. It is observed that not only one but two singular modes may arise. Interestingly, no singularities are present for an interface angle smaller than $\approx 55°$ independent of the material configuration. Increasing the interface angle significantly affects λ and results in rather strong singularities $\lambda \approx 0.6$ for $G_1/G_2 = 1000$. This might be understood as a simple design rule from an engineering point of view, that is, using rather small angles $\psi < 55°$ is favourable in terms of the structure's integrity since no stress singularities are present for this type of loading [20]. This statement is supported by the experimental data in Fig. 4.18. One more interesting

[20] Note that this implies a larger angle on the topside of the beam, which negatively affects the failure load for a reversed bending moment.

feature is observed, that is, complex singularity exponents arise for a sufficiently large interface angle. A typical hint for the occurrence of oscillating singularities is that two real-valued branches meet each other and collapse into one single complex-valued branch. This phenomenon can be observed at an interface angle $\psi \approx 140°$ for $G_1/G_2 = 1000$ and it becomes clear that a framework accounting for complex exponents is crucial.

In order to evaluate the CC, let us first restrict ourselves to the leading-order terms of the expansion of the stresses and the IERR. It follows:

$$\boldsymbol{\sigma}(r,\varphi) \sim \frac{\hat{K}_1 F}{h^2}\left(\frac{r}{h}\right)^{\lambda_1-1}\boldsymbol{\sigma}_1(\varphi) \quad \text{as} \quad r \to 0, \tag{4.45}$$

$$\bar{\mathcal{G}} \sim \frac{\hat{K}_1^2 F^2}{E_2 h^3}\,\hat{\Psi}_{11}(\theta)\left(\frac{\Delta a}{h}\right)^{2\lambda_1-1} \quad \text{as} \quad \Delta a \to 0. \tag{4.46}$$

Here, E_2 represents the Young's modulus of Rohacell. The CC is evaluated for each interface angle ψ with crack length Δa, initiation angle θ and failure load F_f as unknowns. Again, both stress and energy criteria are monotonic functions with respect to the crack length and the optimisation problem can be solved analogously to the previously discussed situations. The failure load F^* and the associated crack length Δa^* in dependence of the initiation angle θ can be written explicitly as

$$F^*(\theta) = \frac{h^{1+\lambda_1}}{\hat{K}_1}\left(\frac{\mathcal{G}_\mathrm{Ic}E_2}{\hat{\Psi}_{11}(\theta)}\right)^{1-\lambda_1}\left(\left(\frac{\sigma_{\varphi\varphi,1}(\theta)}{\sigma_\mathrm{c}}\right)^2+\left(\frac{\tau_{r\varphi,1}(\theta)}{\tau_c}\right)^2\right)^{\frac{1-2\lambda_1}{2}}, \tag{4.47}$$

$$\Delta a^*(\theta) = \frac{\mathcal{G}_\mathrm{Ic}E_2}{\hat{\Psi}_{11}(\theta)}\left(\left(\frac{\sigma_{\varphi\varphi,1}(\theta)}{\sigma_\mathrm{c}}\right)^2+\left(\frac{\tau_{r\varphi,1}(\theta)}{\tau_\mathrm{c}}\right)^2\right). \tag{4.48}$$

The quantities $\{F^*, \Delta a^*\}$ are then calculated for a fixed interface angle while the initiation angle is varied in 1°-steps. A subsequent evaluation of

$$F_\mathrm{f} = \min_\theta \{F^*(\theta)\} \tag{4.49}$$

finally yields the failure load F_f, its associated crack length Δa and the crack initiation angle θ. The failure load F_f is plotted in Fig. 4.20 with respect to the interface angle ψ. Increasing the interface angle leads to a transition from bending failure to notch induced failure. This experimentally observed effect is rendered correctly employing the asymptotic approach. However, the predictions become less precise for larger values of the interface angle. Experimental failure loads are overestimated with a maximum relative error of 25%. In terms of crack length, the predicted lengths are about 6% of the specimen's height. Particularly for large interface angles the present singularity is rather strong $\lambda_1 \approx 0.55$ and the validity range of the one-term asymptotic solution might be exceeded.

In order to assess the range of validity of the asymptotic solution and to further extend its accuracy, the second-order terms are now considered. For this purpose, the behaviour of stresses and the IERR is reconsidered. According to the distribution of the exponent

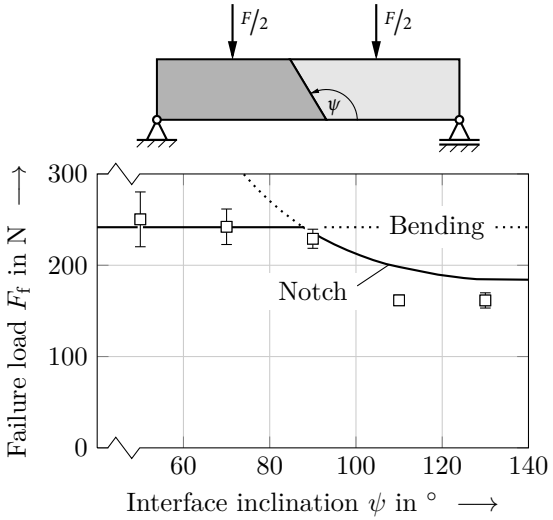

Figure 4.20: Four-point bending test failure load F_f of Rohacell-aluminum scarf joints with respect to the scarf angle ψ. The failure load predictions are obtained using a leading-order term asymptotic solution for notch failure. It can be distinguished between a bending failure mode and notch induced failure.

λ in Fig. 4.19, exponents associated to the second-order term are larger than one for $\psi < 125°$ in case of the Rohacell-Aluminum configuration ($G_1/G_2 = 867$). Moreover, these exponents take complex values which must be accounted for in the asymptotic expansions. Based on the results in Section 3, it follows

$$\boldsymbol{\sigma}(r,\varphi) \sim \frac{F}{h^2}\left(\hat{K}_1\left(\frac{r}{h}\right)^{\lambda_1-1}\boldsymbol{\sigma}_1(\varphi) + \hat{K}_2\left(\frac{r}{h}\right)^{\lambda_2-1}\boldsymbol{\sigma}_2(\varphi) + \overline{\hat{K}}_2\left(\frac{r}{h}\right)^{\overline{\lambda}_2-1}\overline{\boldsymbol{\sigma}}_2(\varphi)\right) \tag{4.50}$$

for the stresses as $r \to 0$ and

$$\bar{\mathcal{G}} \sim \frac{F^2}{E_2 h^3}\left(\hat{K}_1^2\left(\frac{\Delta a}{h}\right)^{2\lambda_1-1}\hat{\Psi}_{11} + 4\mathrm{Re}\left[\hat{K}_1\hat{K}_2\hat{\Psi}_{21}\left(\frac{\Delta a}{h}\right)^{\lambda_1+\lambda_2-1}\right]\right) \tag{4.51}$$

for the IERR up to the second term as $\Delta a \to 0$. Young's modulus of Rohacell is denoted with E_2. It should be noted, that calculating Ψ_{21} contains the function $\underline{\hat{V}}_1$ which is already known from the leading-order term solution. Thus, taking the second-order term into account does not increase the number of finite element calculations. Only two FEA are required in total to compute the quantities $\hat{K}_1, \hat{K}_2, \hat{\Psi}_{11}$ and $\hat{\Psi}_{21}$ for each interface and crack angle.

In order to examine the effect of higher-order terms on the distribution of the stresses and the IERR, let us consider the particular joint configuration with an interface angle $\psi = 90°$. The employed stress criterion in Eq. (2.66) is evaluated along a radial path enclosing a 75°-angle with the x_1-axis. Results based on the first-order term in Eq. (4.45) and terms up to the second-order according to Eq. (4.50) are shown in Fig. 4.21(a). Furthermore, the numerical reference solution is plotted based on a detailed FEA with a very fine mesh in the close vicinity of the bi-material notch. It is observed that

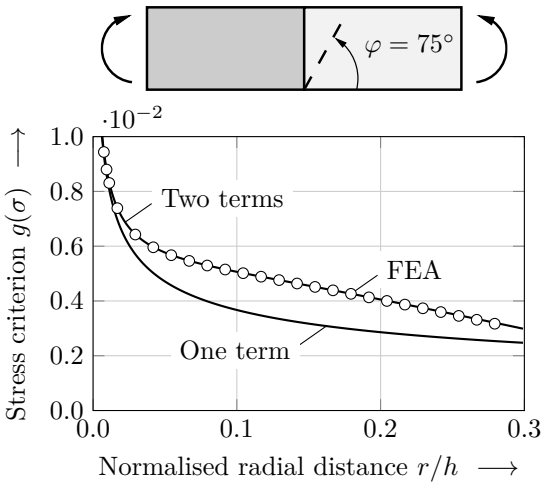

(a) Values of the elliptical stress function for unit load with respect to the dimensionless radial distance r/h from the notch tip along a 75° path in the uncracked state ($\varphi = 75°$).

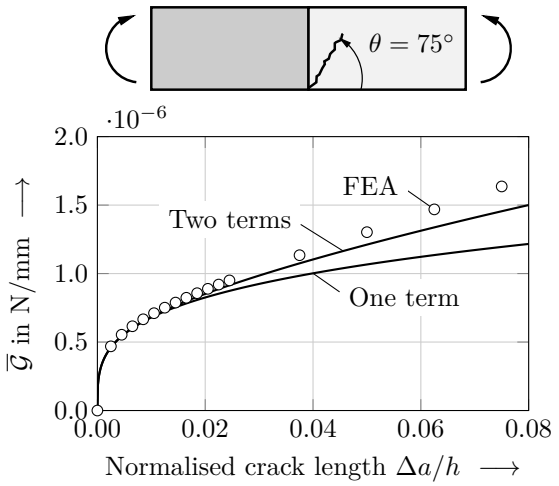

(b) Values of IERR $\bar{\mathcal{G}}$ for unit load with respect to the dimensionless crack length $\Delta a/h$ for a crack initiation angle $\theta = 75°$.

Figure 4.21: Comparison between stress and energy quantities based on a one-term and a two-term asymptotic expansion and numerical reference data for a vertical interface $\psi = 90°$.

the leading-order term is a rather accurate approximation up to a relative distance $r/h \approx 0.02$. Beyond that, higher-order terms start playing an increasingly important role. Using only the first-order term underestimates the reference data with a relative error of 37% at a distance of 10% of the specimen's height. Accounting for these higher-order terms yields a correction to higher values of the equivalent stress function. As a result, the second-order term leads to a significant improvement of the asymptotic solution accuracy showing an excellent agreement with the numerical data. In addition, Fig. 4.21(a) illustrates the very accurate extraction of the GSIFs $\hat{K}_1$ and $\hat{K}_2$ using the Ψ-integral. Besides stress data, let us consider the behaviour of the IERR with respect to the crack length. To assess the accuracy of its asymptotic approximation, a 90°-interface joint configuration is examined having a crack orientated in a 75°-direction ($\theta = 75°$) with respect to the x_1-axis. The IERR $\bar{\mathcal{G}}$ is shown in Fig. 4.21(b) with respect to the dimensionless crack length $\Delta a/h$. The reference solution is obtained calculating the change of total potential energy $\Delta\Pi$ numerically. For this purpose, numerous FEA of the cracked configuration are performed using a very fine mesh to capture the behaviour for small crack lengths correctly. In contrast, the asymptotic approach only required two FEA on the scaled inner domain $\Omega^{\Delta a}$. In comparison with the reference solution, the behaviour for small crack lengths $\Delta a/h \leq 0.02$ is well captured by the leading-order term in Eq (4.46). Including the second-order term according to Eq (4.51) improves the approximation accuracy for larger cracks and at the same time indicates, that the leading-order term tends to underestimate the amount of energy dissipated during crack formation. In summary, incorporating the second-order term into the asymptotics of stresses and the IERR improves the accuracy of the asymptotic solution

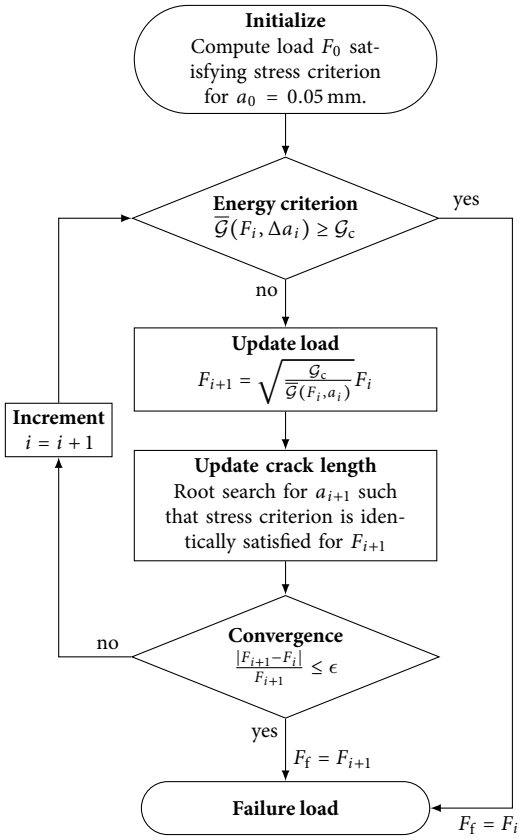

Figure 4.22: Flowchart of the iterative methodology to solve the optimisation problem of the CC.

significantly. Furthermore, no additional computational effort is needed in comparison to a single leading-order term approximation due to the symmetry property $\Psi_{12} = \Psi_{21}$. Moreover, the second-order term enables to estimate the asymptotic's range of validity and whether the error leads to conservative predictions or not, even without having a numerical reference solution at hand. The second-order term shows, that a leading-order solution yields imprecise predictions for $\Delta a/h > 0.02$ and tends to overestimate the failure load, cf. Fig. 4.20.

4.4.3 Iterative numerical approach for notch induced failure

The described asymptotic approach allows for a very efficient treatment of the present crack initiation problem. In order to verify the asymptotic model, notch induced crack formation is analysed fully numerically in the following. Despite computationally more expensive, an efficient methodology is presented to numerically evaluate the CC.

Solving the optimisation problem induced by the CC for a given interface angle ψ requires knowledge of IERRs $\bar{\mathcal{G}}(\Delta a, \theta)$ for any admissible crack configuration. Computing the IERR for a certain crack characterised by $\{\Delta a, \theta\}$, requires to solve a separate BVP for every configuration. This can be carried out for all possible cracks within an offline

stage in which the required data base is built up and all parameters required to solve the optimisation problem are calculated. Based on the computed data, the optimisation problem is then solved which is also referred to as online stage. This methodology is efficient when different material properties are to be examined since these parameters enter the online stage. Since the present crack initiation problem involves two unknowns, the crack length Δa and the crack angle θ, a large set of BVPs must be solved for the offline stage. Consequently, an alternative solution strategy is used in the subsequent analysis. Exploiting certain parameter relations, an iterative, fully online optimisation procedure is employed. The scheme is similar to the one used by Stein et al. (2015) and requires no computationally expensive offline stage. The algorithm efficiently computes the failure load F_f and the corresponding crack length Δa for a specific crack angle θ. Its flowchart is depicted in Fig. 4.22. The scheme is initialised choosing a small initial crack length a_0. In the present case, $a_0 = 0.05\,\mathrm{mm}$ is set equal to the radial length of two elements of the employed finite element mesh. Performing a root search provides the initial load F_0 satisfying the stress criterion at the distance $r = a_0$. In each consecutive iteration i, the energy criterion is evaluated. If it is satisfied with a small tolerance, the failure load F_f and corresponding crack length $\Delta a = a_\mathrm{f}$ are determined. Otherwise, the load is updated. Accounting for $\bar{\mathcal{G}} \propto F^2$, the load F_{i+1} required to fulfil the energy condition at the current crack length a_i can be computed:

$$F_{i+1} = \sqrt{\frac{\mathcal{G}_\mathrm{c}}{\bar{\mathcal{G}}(F_i, a_i)}} F_i \,. \tag{4.52}$$

Again using a root search, a new crack length a_{i+1} is calculated at which the stress criterion is identically fulfilled for the new load F_{i+1}. Crack length and load are updated repeatedly until the change in loading between two consecutive iterations satisfies the convergence criterion

$$\frac{|F_{i+1} - F_i|}{F_{i+1}} \leq \varepsilon \ , \tag{4.53}$$

where a tolerance of $\varepsilon = 10^{-3}$ is sufficient in the present case. This iterative procedure is repeated for different crack angles. Ultimately, the smallest failure load of all tested crack angles represents the final failure load of the structure.

4.4.4 Discussion and validation of the asymptotic approach

The CC is now evaluated using the two-term asymptotic expansions of stresses and IERR. This leads to non-linear algebraic equations which are solved numerically applying Newton's method. Furthermore, the purely numerical methodology is applied serving as reference solution. The failure load F_f is shown in Fig. 4.23(a) in dependence to the interface angle ψ. The predictions are in a very good agreement with the experimental data. The relative error between asymptotics and experiments is smaller than 9%. The point of transition from notch induced failure to the bending failure mode occurs at an interface angle of $\psi \approx 83°$. It is observed that taking into account the second-order term yields a significant improvement of the predicted failure loads compared to the leading-order term approach, cf. Fig. 4.20. In addition, a comparison with the

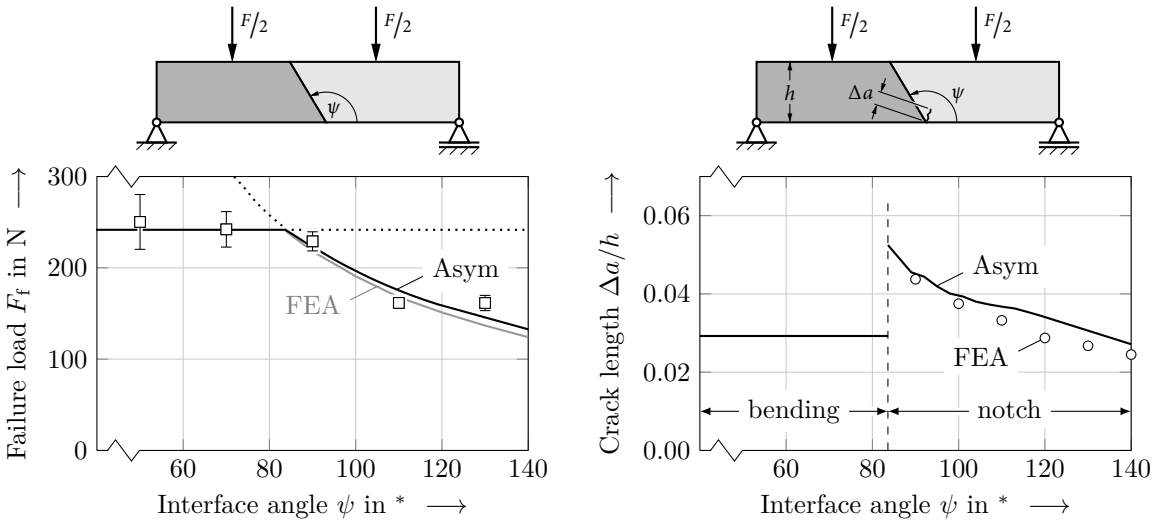

(a) Failure load F_f with respect to the scarf angle ψ.

(b) Asymptotic and numerical prediction of the crack length for varying scarf angle ψ.

Figure 4.23: Comparison between experimentally observed failure loads of the aluminum-Rohacell joint and predictions employing the two-term asymptotic approach as well as numerical reference data.

numerical reference data indicates accurate predictions of the asymptotic approach with a maximum relative error of 6.6%. The corresponding normalised crack length $\Delta a/h$ is plotted in Fig. 4.23(b). In the notch induced failure region, the asymptotic and the numerical predictions show an increasing crack length with a decreasing interface angle. Passing the point of transition to the bending failure region yields a drop in terms of crack length. This is mainly due to the energy criterion and can be interpreted as follows: at the point of transition from notch induced failure to bending failure, cracks are forced to nucleate in parallel to the interface as depicted in Fig. 4.24. However, the stiffer aluminium adherend on the left-hand side impedes deformation and thus crack opening. Hence, the rate at which the energy release increases with respect to the crack length is getting smaller. In case of bending failure, crack formation arises in a sufficient distance[21] from the stiffer adherend leading to a linear behaviour of the IERR ($\lambda_1 = 1$). Consequently, at a certain crack length, the amount of energy that is released becomes higher compared to a crack located in the vicinity of the interface. Therefore, a shorter crack already releases enough energy to fulfil the energy criterion ultimately causing the observed drop in crack length. In terms of a comparison to other failure criteria, the CC shows that the crack length does not represent a material property, as for instance supposed in the TCD based approach by Ribeiro-Ayeh and Hallström (2003). Instead, the crack length depends on the structure's geometry. This unique feature of the CC is ultimately responsible for outperforming the TCD results presented in Ribeiro-Ayeh and Hallström (2003). A maximum relative error of 40%

[21] Note that this distance is not determined with the present modelling. This would require a more detailed model for the bending failure case.

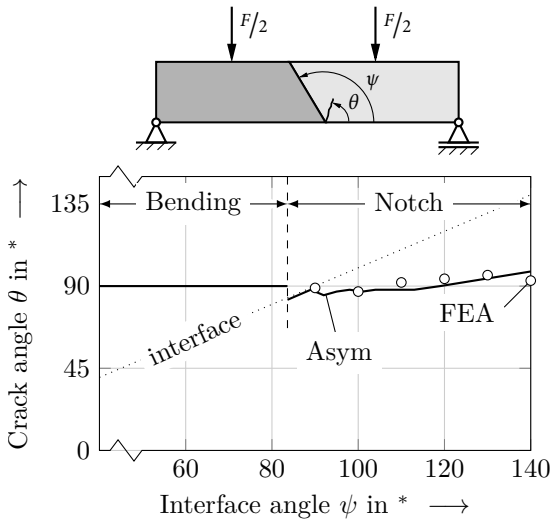

(a) Asymptotic and numerical prediction of the crack angle θ for a varying scarf angle ψ.

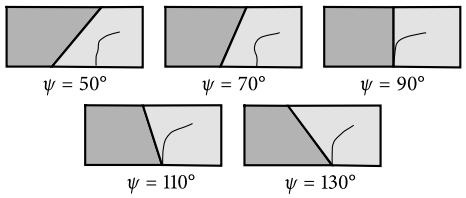

(b) Schematic representation of observed crack paths according to experimental data in Ribeiro-Ayeh and Hallström (2003).

Figure 4.24: Comparison between experimentally observed crack angles θ in case of an aluminum-Rohacell joint and predictions based on the extended asymptotic approach.

between predictions and experiments occurs which drops behind the above mentioned 9% based on the CC. Let us consider the resulting crack initiation angle θ with respect to the interface angle ψ as shown in Fig. 4.24(a). For the notch induced failure mode, it is observed that cracks initiate approximately at a constant 90° angle. Decreasing the interface angle would lead to cracks orientated in parallel to the interface, supposing that notch induced failure still holds. This constraint imposed by the interface yields the transition to bending failure. The experimentally observed crack patterns are schematically illustrated in Fig. 4.24(b) showing that the CC correctly renders the crack initiation process.

The aluminium adherend is now replaced by a PMMA adherend which allows for discussing the effect of changing material properties on the joint's failure behaviour. The corresponding failure load F_f is plotted in Fig. 4.25 with respect to the interface angle. Importantly, it is observed that the failure load within the bending failure region does not change in comparison to the aluminum configuration. This further supports that the applied modelling of a homogeneous Rohacell beam is suitable for bending failure. As a result of the reduced elastic mismatch between both adherends, failure loads are slightly higher than in the Rohacell-aluminum configuration. Again, the CC leads to an accurate failure prediction in comparison to experimental data with a MAPE of 5.4%.

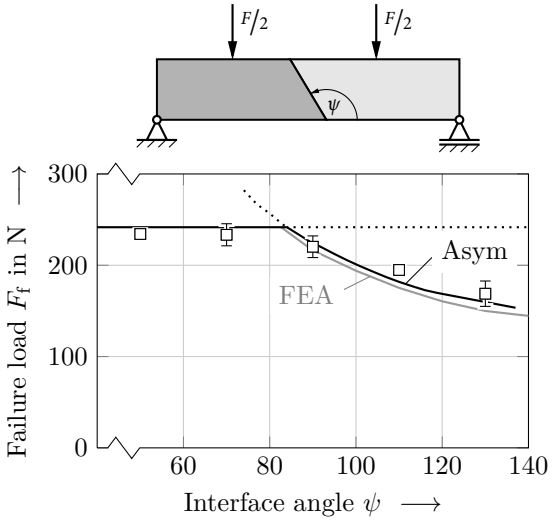

Figure 4.25: Failure load F_f of a PMMA-Rohacell joint with respect to the interface angle ψ. Comparison between predictions according to the extended two-term asymptotic approach, numerical reference data and experimental results by Ribeiro-Ayeh and Hallström (2003).

4.5 Remarks and outlook

Presuming brittle fracture, it has been demonstrated, that crack nucleation at sharp and bi-material notches can be accurately and efficiently assessed employing the present asymptotic approach. A validated model represents the basis for tackling further complex problems featuring competing failure scenarios, such as a single lap joint with fillet (Groth, 1988, Stein et al., 2017) where the point of crack onset as well as the crack orientation are a priori unknown. Furthermore, the methodology applies for modelling advanced testing methods such as the modified Arcan test and enables a detailed characterisation of bonded assemblies under mixed-mode loading conditions. The semi-analytical nature of the asymptotic approach perfectly suits for an inverse parameter identification, e.g. the material strength and toughness, being very time-consuming employing CZM (Valoroso et al., 2013, Valoroso and Fedele, 2010, Maier et al., 2006) or a fully numerical evaluation of the CC (Le Pavic et al., 2017).

Based on case studies presented in this work, it has been investigated to what extent geometrical (e.g. the adhesive thickness) and material parameters (e.g. the elastic mismatch) affect the accuracy of the asymptotic approach. However, the quantities tensile strength and fracture toughness also affect the crack length and hence the validity range of asymptotics. Together, tensile strength, Young's modulus and fracture toughness form a length quantity $L_c = E\mathcal{G}_c/\sigma_c^2$, also referred to as characteristic fracture length (Martin et al., 2016). In future woks, the effect of this fracture length on the resulting crack length and hence on the validity of the asymptotic expansions is worth investigating. Generally, a smaller value of L_c leads to smaller crack lengths implying brittle failure behaviour. Applying the concept of finite fracture mechanics relies on brittle fracture which inherently sets an upper bound for L_c or more precisely for the brittleness number as a metric to quantitatively characterise brittleness (Carpinteri et al., 2008, Cornetti et al., 2012, Weißgraeber and Becker, 2013, Carpinteri, 1982).

Thus, attention has to be paid to not violate the underlying assumptions of finite fracture mechanics. This already indicates the need of generalising the asymptotic approach in order to tackle situations where a small damage or plastic zone is present and its influence in terms of energy dissipation can no longer be neglected. This type of problem has been addresses by Leguillon and Yosibash (2017) showing that a damage zone starts to grow prior to crack formation. In this context, the results of the present work can serve as a basis for further activities.

Further work can also be attributed to a thorough comparison between the coupled criterion and phase-field models of fracture. Here, the phenomenon of finite crack nucleation is of particular interest and the semi-analytical expressions of the asymptotic approach might represent a suitable tool to identify common physical effects.

Besides static failure studied in this work, the problem of fatigue is of crucial importance in engineering practice. Murer and Leguillon (2010) proposed a first idea of modelling fatigue failure of quasi-brittle materials at V-notches employing a Dugdale model and using asymptotics. Here, further experimental data is required and an extension of the model to bi-material problems can be pursued.

Further potential applications of the asymptotic methodology are three-dimensional problems as addresses by Leguillon (2014). Although challenging, the feature of decoupling the length scale associated to crack onset from the macroscopic scale appears to be very advantageous. A suitable starting point for further investigations represents the study by Labossiere and Dunn (2001) of a three-dimensional bi-material joint.

Chapter 5

Crack onset at open holes in composite plates of finite width

In this section, brittle failure of finite-width fibre-reinforced composite plates under uniaxial tension loading containing a circular or elliptical hole is examined. Depending on the material anisotropy, the formation of symmetric as well as antisymmetric crack patterns is investigated accounting for mixed-mode fracture. Due to the extended set of involved parameters, that is the crack direction, the crack length, the hole's geometry and the plate's finite width, a semi-analytical approach as described in the previous sections 3-4 is favourable and provides an efficient failure analysis. However, the major challenge faced in this section is to transfer the approach of matched asymptotic expansions from sharp notch configurations to the rounded notch situation at the hole's boundary. At the outset of the asymptotic modelling, the required stress solution of the uncracked open-hole plate including the effect of the finite width is given based on the method of complex potentials. Subsequently, the matched asymptotic framework is established leading to a power-series expansion of the change in total potential energy due to crack onset. Higher-order terms are considered and the idea of Padé approximation is applied in order to improve the accuracy of the asymptotic solutions. A detailed comparison with numerical reference solutions is performed and the effects of the plate's finite width, the geometry of the hole, the direction of crack initiation as well as the material anisotropy are discussed in detail. Finally, failure predictions based on the asymptotic approach are compared against full-numerical reference solutions and experimental data from literature. The modelling and results presented in this section have been published in Engineering Fracture Mechanics (Felger et al., 2017a) and in the International Journal of Solids and Structures (Felger et al., 2017b).

5.1 Introduction

Joining components in engineering structures induces open holes and cut-outs that significantly affect the structural integrity. Premature failure of the structure typically originates from such stress raisers. This is, in particular, a major concern regarding open-hole composite plates of finite width. Whereas the dimensionless stress concentration factor for an infinite isotropic plate weakened by a circular hole attains the well known value of three following Kirsch's solution (Kirsch, 1898), its value significantly depends on the layup and the finite width in case of fibre-reinforced

open-hole composite plates. Consequently, a detailed understanding of the underlying failure processes is crucial for a reliable and accurate assessment of such stress concentrations.

The problem of assessing the structural integrity of open-hole plates goes back to the 1970s. Waddoups et al. (1971) used concepts based on classical LEFM to predict the critical load at failure of $[0°/\pm 45°]_{2S}$ graphite-epoxy laminates under uniaxial tension containing circular holes of different size. More precisely, they presumed the existence of intense energy regions, which were modelled as through-thickness cracks of a certain length perpendicular to the load direction extending symmetrically from each side of the hole. Although the predictions are in agreement with experimental data showing a decreasing effective strength for an increasing hole radius, the assumed crack length turned out not to be a material constant and no physical interpretation was given to this quantity. Three years later, Whitney and Nuismer (1974) employed an averaged stress criterion to predict the critical load at failure of quasi-isotropic glass-epoxy laminates weakened by a circular hole. Their model captures the experimental results, however, stresses are averaged over an a-priori unknown length, which must be tuned according to experimental data. Nevertheless, this stress based approach has been adopted and continuously modified in the following years. In particular, Tan (1994) applied point-wise as well as averaged stress criteria to composite plates with circular holes, elliptical holes and different composite layups. Again, the involved length parameter must be fitted to experimental data. Very recently, Bleyer and Alessi (2018) studied crack formation at a circular hole in a composite plate employing a phase-field modelling approach. The authors compared their results against the asymptotic approach presented in this section, cf. (Felger et al., 2017b), and a very good agreement is observed. Although very flexible in terms of application, phase-field approaches are computationally expensive and a regularisation length parameter enters the model that must be chosen adequately. This drawback can be overcome using the coupled criterion avoiding the use of unknown length parameters. The coupled criterion has been applied to predict symmetric crack patterns in quasi-isotropic composite plates under uniaxial tensile loading (Camanho et al., 2012, Martin et al., 2012, Erçin et al., 2013, Romani et al., 2015) as well as crack patterns for combined tensile and bending loading (Rosendahl et al., 2017). Moreover, crack onset has been assessed at elliptical holes in infinite isotropic plates (Weißgraeber et al., 2016a). The work presented in this section on the one hand attempts to extend and validate the applicability of the coupled criterion to anisotropic plates of finite width and inclined crack configurations and on the other hand establishes an asymptotic framework for open-hole plates enabling an efficient evaluation of the criterion.

Let us consider a fibre-reinforced composite plate of thickness d and width w under uniaxial tensile loading σ_∞ as depicted in Fig. 5.1. The subsequent analysis is restricted to through-thickness cracks, thus a two-dimensional modelling is applied and the crack is characterised by its length Δa. The material behaviour is supposed to be linear elastic and the composite plate is modelled using classical laminate plate theory presuming a symmetric layup. In case of a symmetric configuration according to Fig. 5.1(a), the initiation of two horizontal cracks is presumed. This has been observed in experiments by Tan (1988a) serving as validation of the proposed failure model. In

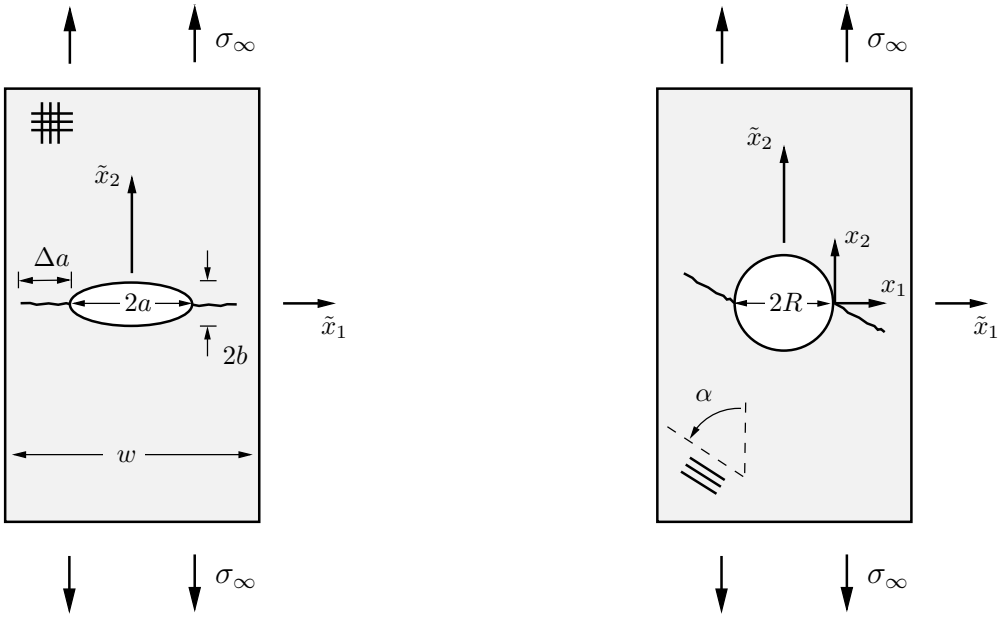

(a) Composite plate containing an elliptical hole with half-axis a and b and symmetric cracks.

(b) Unidirectional fibre-reinforced plate containing a circular hole and anti-symmetric cracks. The fibre orientation is characterised by α.

Figure 5.1: Open-hole fibre-reinforced composite plates loaded by uniaxial tension σ_∞. The geometry is characterised by the thickness d, width w and cracks of finite length Δa emanating from the hole.

addition, the case of a unidirectional layer with a fibre orientation characterised by the angle α is considered as shown in Fig. 5.1(b). This situation has been experimentally investigated by Modniks et al. (2014). Since no plane of symmetry exists, inclined cracks nucleate anti-symmetrically within the matrix material following the direction of the fibres.

5.2 Uncracked configuration: stress field in the vicinity of the hole

In order to evaluate the stress criterion, the stresses along potential crack paths in the uncracked configuration have to be determined. At the outset, the solution is sought on an infinite domain containing an elliptical hole. A powerful approach to solve such BVPs on complex domains within the theory of anisotropic elasticity is the method of complex potentials. More precisely, the problem of an infinite anisotropic plate containing an elliptical hole is tackled using the tool of conformal mapping. Here, the infinite domain with the elliptical hole is mapped on the exterior of the unit circle by means of an adequate mapping function. The resulting complex potentials can be found in the classical textbooks by Lekhnitskii (1963) or Savin (1961) and the stress field

ultimately reads:

$$\frac{\sigma_{11}^{\infty}}{\sigma_{\infty}} = 2\mathrm{Re}\left[\frac{a\mu_1^2\mu_2}{2\left(\mu_1-\mu_2\right)\left(a+\mathrm{i}b\mu_1\right)}\left(1-\frac{z_1}{\sqrt{z_1^2-\left(a^2+\mu_1^2b^2\right)}}\right)\right.$$
$$\left.-\frac{a\mu_1\mu_2^2}{2\left(\mu_1-\mu_2\right)\left(a+\mathrm{i}b\mu_2\right)}\left(1-\frac{z_2}{\sqrt{z_2^2-\left(a^2+\mu_2^2b^2\right)}}\right)\right], \tag{5.1}$$

$$\frac{\sigma_{22}^{\infty}}{\sigma_{\infty}} = 1+2\mathrm{Re}\left[\frac{a\mu_2}{2\left(\mu_1-\mu_2\right)\left(a+\mathrm{i}b\mu_1\right)}\left(1-\frac{z_1}{\sqrt{z_1^2-\left(a^2+\mu_1^2b^2\right)}}\right)\right.$$
$$\left.-\frac{a\mu_1}{2\left(\mu_1-\mu_2\right)\left(a+\mathrm{i}b\mu_2\right)}\left(1-\frac{z_2}{\sqrt{z_2^2-\left(a^2+\mu_2^2b^2\right)}}\right)\right], \tag{5.2}$$

$$\frac{\sigma_{12}^{\infty}}{\sigma_{\infty}} = -2\mathrm{Re}\left[\frac{a\mu_1\mu_2}{2\left(\mu_1-\mu_2\right)\left(a+\mathrm{i}b\mu_1\right)}\left(1-\frac{z_1}{\sqrt{z_1^2-\left(a^2+\mu_1^2b^2\right)}}\right)\right.$$
$$\left.-\frac{a\mu_2\mu_1}{2\left(\mu_1-\mu_2\right)\left(a+\mathrm{i}b\mu_2\right)}\left(1-\frac{z_2}{\sqrt{z_2^2-\left(a^2+\mu_2^2b^2\right)}}\right)\right]. \tag{5.3}$$

Here, $z_k = \tilde{x}_1 + \mu_k\tilde{x}_2$ holds for the generalised complex coordinates and the $\tilde{x}_1$-$\tilde{x}_2$ coordinate system is depicted in Fig. 5.1. The complex parameters μ_k represent the roots of the characteristic equation

$$S_{11}\mu^4 - 2S_{16}\mu^3 + (2S_{12}+S_{66})\mu^2 - 2S_{26} + S_{22} = 0, \tag{5.4}$$

with the compliances S_{ij}. The components S_{ij} are calculated according to classical laminate plate theory by inverting Eq. (2.22). Since stresses are to be evaluated along an inclined path, it is feasible to introduce a new x_1-x_2 coordinate system with its origin located at $\tilde{x}_1 = a$ and $\tilde{x}_2 = 0$, cf. Fig. 5.1(b). This x_1-x_2 coordinate system will also be used later on in the matched asymptotics framework.

To account for the influence of the plate's finite width w on the stress distribution, the idea of a finite-width correction (FWC) factor is adopted providing a simple and robust approximation. Following this approach, the closed-form notched infinite-plate solution is scaled with an appropriate FWC factor κ,

$$\sigma_{22} = \kappa\sigma_{22}^{\infty}, \tag{5.5}$$

in such a way that the following equilibrium condition holds:

$$\kappa\int_a^{w/2}\sigma_{22}^{\infty}(\tilde{x}_1,0)\mathrm{d}\tilde{x}_1 = \int_a^{w/2}\sigma_{22}(\tilde{x}_1,0)\mathrm{d}\tilde{x}_1 = \frac{\sigma_{\infty}w}{2}. \tag{5.6}$$

Based on this procedure, an improved FWC factor for anisotropic elliptically notched plates has been proposed by Tan (1988b) which is employed in the subsequent analysis. The improved FWC factor has been successfully applied in former studies (Camanho et al., 2012, Martin et al., 2012) and yields accurate results in comparison with numerical data for opening-to-width ratios $\omega = 2a/w < 0.5$ and for aspect ratios $\Lambda = b/a < 1/4$ of

the ellipse. The improved FWC factor can be written as

$$\kappa = \left(1-\omega M + \mathrm{Re}\left[\frac{1}{\mu_1-\mu_2}\left(\frac{\mu_2}{1+\mathrm{i}\mu_1\Lambda}\left(1-\omega M-\mathrm{i}\mu_1\Lambda\omega M-\sqrt{1-(1+\mu_1^2\Lambda^2)(\omega M)^2}\right)\right.\right.\right.$$
$$\left.\left.\left.-\frac{\mu_1}{1+\mathrm{i}\mu_2\Lambda}\left(1-\omega M-\mathrm{i}\mu_2\Lambda\omega M-\sqrt{1-(1+\mu_2^2\Lambda^2)(\omega M)^2}\right)\right)\right]\right)^{-1}, \tag{5.7}$$

with

$$M^2 = \frac{\sqrt{1-8\left(\frac{3(1-\omega)}{2+(1-\omega)^3}-1\right)}-1}{2\omega^2}. \tag{5.8}$$

5.3 Cracked configuration: asymptotic analysis

In addition to the stress field in the uncracked state, the coupled criterion requires the knowledge of the IERR $\bar{\mathcal{G}}$ due to crack formation. Since no closed-form solutions are available in literature for the situation of a finite-width open-hole composite plate with cracks emanating from the hole, numerical solution methods are needed. However, if the crack length Δa is small compared to any characteristic structural length, an asymptotic approach can be established leading to semi-analytical relations containing the crack length explicitly. As shown in Fig. 5.2, the idea of a shallow crack asymptote is adopted in the subsequent analysis, cf. Wormsen et al. (2006). Here, the situation of a crack emanating from a curved boundary is asymptotically described by means of an unnotched plate with an edge crack subjected to the local notch stress field. Consequently, the process of crack formation is investigated on the simplified domains Ω^0 and $\Omega^{\Delta a}$ as depicted in Fig. 5.2, asymptotically representing the uncracked and the cracked configuration, respectively.

5.3.1 Outer expansion

The outer expansion is formulated on the outer domain Ω^0 and provides an approximation of the perturbed solution $\underline{U}^{\Delta a}$ sufficiently far away from the perturbation:

$$\underline{U}^{\Delta a}(r,\varphi) = \underline{U}^0(r,\varphi) + f_1(\varepsilon)\underline{U}^1(r,\varphi) + f_2(\varepsilon)\underline{U}^2(r,\varphi) + o(f_2(\varepsilon)). \tag{5.9}$$

The leading-order term $\underline{U}^0(r,\varphi)$ represents the solution of the BVP visualised in Fig. 5.2(a), that is, the solution of an unnotched plate with far-field loading corresponding to the local notch stress field. The function $\underline{U}^0(r,\varphi)$ is determined by means of the complex potential method for anisotropic materials. The following ansatz for the complex

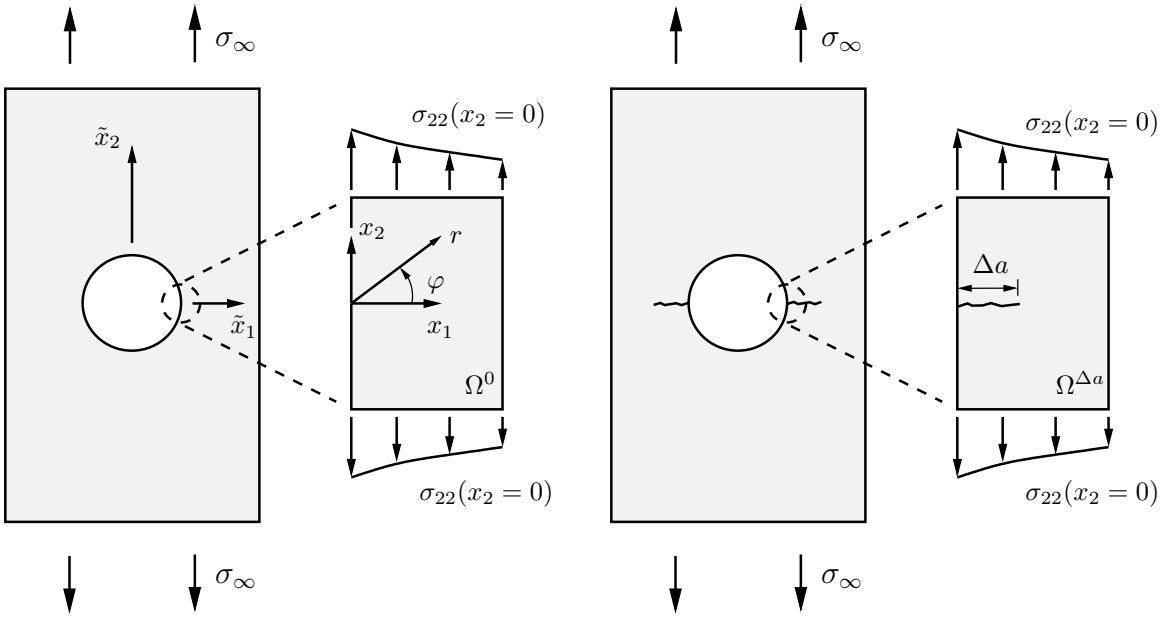

(a) Uncracked notched plate and unperturbed domain Ω^0.

(b) Cracked notched plate and perturbed domain $\Omega^{\Delta a}$.

Figure 5.2: Finite-width notched plates and the related local domains subjected to the local notch stress field.

functions $\Phi_1(z_1)$ and $\Phi_2(z_2)$ is employed, cf. Eq. (3.2):

$$\Phi_1(z_1) = \sum_i A_{1i} z_1^{\lambda_i}, \quad \Phi_2(z_2) = \sum_i A_{2i} z_2^{\lambda_i}, \quad \lambda_i \in \mathbb{R}, \quad A_{ki} \in \mathbb{C}. \tag{5.10}$$

The exponents λ_i are calculated requiring that the stress-free boundary conditions along the straight edge of Ω^0 are satisfied:

$$\sigma_{\varphi\varphi}(r,\varphi)\Big|_{\varphi=\pm\frac{\pi}{2}} = \tau_{r\varphi}(r,\varphi)\Big|_{\varphi=\pm\frac{\pi}{2}} = 0. \tag{5.11}$$

This leads to a homogeneous system $\mathbf{D}\underline{a}_i = 0$ of four linear equations which can be written in the form:

$$\mathbf{D} = \begin{pmatrix} \mathrm{Re}\left[\mu_1^{1+\lambda}\right] & -\mathrm{Im}\left[\mu_1^{1+\lambda}\right] & \mathrm{Re}\left[\mu_2^{1+\lambda}\right] & -\mathrm{Im}\left[\mu_2^{1+\lambda}\right] \\ \mathrm{Re}\left[-\mu_1^{1+\lambda}\right] & -\mathrm{Im}\left[-\mu_1^{1+\lambda}\right] & \mathrm{Re}\left[-\mu_2^{1+\lambda}\right] & -\mathrm{Im}\left[-\mu_2^{1+\lambda}\right] \\ \mathrm{Re}\left[\mu_1^{\lambda}\right] & -\mathrm{Im}\left[\mu_1^{\lambda}\right] & \mathrm{Re}\left[\mu_2^{\lambda}\right] & -\mathrm{Im}\left[\mu_2^{\lambda}\right] \\ -\mathrm{Re}\left[-\mu_1^{\lambda}\right] & \mathrm{Im}\left[-\mu_1^{\lambda}\right] & -\mathrm{Re}\left[-\mu_2^{\lambda}\right] & \mathrm{Im}\left[-\mu_2^{\lambda}\right] \end{pmatrix}, \tag{5.12}$$

$$\underline{a}_i = \Big(\mathrm{Re}\left[A_{1i}\right], \mathrm{Im}\left[A_{1i}\right], \mathrm{Re}\left[A_{2i}\right], \mathrm{Im}\left[A_{2i}\right]\Big)^T. \tag{5.13}$$

For non-trivial solutions to exist, the determinant of the coefficient matrix $\mathbf{D}$ must vanish leading to:

$$\lambda_1 = 1, \ \lambda_2 = 2, \ \lambda_3 = 3, \ldots \quad . \tag{5.14}$$

The quantities $\underline{a}_i$ can then be calculated as the kernel of the matrix $\mathbf{D}(\lambda_i)$. Each couple of complex coefficients $\{A_{1i}, A_{2i}\}$ is associated to a characteristic deformation mode and is defined up to a multiplicative constant K_i, that is the intensity factor. Finally, the leading-order term $\underline{U}^0(r,\varphi)$ in the outer expansion and the corresponding stresses can be written as:

$$\underline{U}^0 = K_1 r \underline{u}_1(\varphi) + K_2 r^2 \underline{u}_2(\varphi) + \mathcal{O}\left(r^2\right), \tag{5.15}$$

$$\boldsymbol{\sigma}\left(\underline{U}^0\right) = K_1 \boldsymbol{\sigma}_1(\varphi) + K_2 r \boldsymbol{\sigma}_2(\varphi) + \mathcal{O}\left(r\right). \tag{5.16}$$

The irrelevant terms in the expansions associated to rigid body motions are omitted. The components $\{u_{r,i}, u_{\varphi,i}\}$ of the displacement eigenfunctions $\underline{u}_i$ are given by

$$\begin{aligned} u_{r,i}(\varphi) &= 2\mathrm{Re}\left[\sum_{k=1}^{2} A_{ki}\left(p_k\cos(\varphi) + q_k\sin(\varphi)\right)\left(\cos(\varphi) + \mu_k\sin(\varphi)\right)^i\right], \\ u_{\varphi,i}(\varphi) &= 2\mathrm{Re}\left[\sum_{k=1}^{2} A_{ki}\left(q_k\cos(\varphi) - p_k\sin(\varphi)\right)\left(\cos(\varphi) + \mu_k\sin(\varphi)\right)^i\right]. \end{aligned} \tag{5.17}$$

The components $\{\sigma_{rr,i}, \sigma_{\varphi\varphi,i}, \tau_{r\varphi,i}\}$ of the stress eigenfunctions $\boldsymbol{\sigma}_i(\varphi)$ can be written as

$$\begin{aligned} \sigma_{\varphi\varphi,i}(\varphi) &= 2\mathrm{Re}\left[\sum_{k=1}^{2} A_{ki}\left(\cos(\varphi) + \mu_k\sin(\varphi)\right)^{i+1}\right], \\ \sigma_{rr,i}(\varphi) &= 2\mathrm{Re}\left[\sum_{k=1}^{2} A_{ki}\left(\sin(\varphi) - \mu_k\cos(\varphi)\right)^2\left(\cos(\varphi) + \mu_k\sin(\varphi)\right)^{i-1}\right], \\ \tau_{r\varphi,i}(\varphi) &= 2\mathrm{Re}\left[\sum_{k=1}^{2} A_{ki}\left(\sin(\varphi) - \mu_k\cos(\varphi)\right)\left(\cos(\varphi) + \mu_k\sin(\varphi)\right)^i\right]. \end{aligned} \tag{5.18}$$

The constants p_i and q_i are given by $(i = 1, 2)$

$$\begin{aligned} p_i &= S_{11}\mu_i^2 + S_{12} - S_{16}\mu_i, \\ q_i &= S_{12}\mu_i + \frac{S_{22}}{\mu_i} - S_{26}. \end{aligned} \tag{5.19}$$

To proceed with the asymptotic modelling, the next step is to calculate the intensity factors K_i involved in the expansion of $\underline{U}^0(r,\varphi)$. In the previous sections, this has been done by means of FEA and the Ψ-integral. In the present case, however, the intensity factors can be computed analytically. This is first demonstrated for the symmetric configuration where two horizontal cracks eventually initiate. Subsequently, the procedure is generalised to the anti-symmetric case.

Symmetric configuration

Consider the simplified domain Ω^0 as illustrated in Fig. 5.2(a). The applied loading at the outer boundary of Ω^0 is given by the local notch stress field. This local stress

field is known since we have the closed-form solution and the finite-width correction factor at hand. Therefore, the coefficients K_i can be obtained as follows: expanding the scaled solution $\kappa\sigma_{22}^{\infty}$ in Eq. (5.5) as a Taylor series with respect to the radial coordinate r along $\varphi = 0$ and subsequently comparing coefficients with $\sigma_{\varphi\varphi}$ in the expansion (5.16). It is convenient to normalise the dimensionless eigenfunctions $\boldsymbol{\sigma}_i(\varphi)$ in Eq. (5.16) such that

$$\sigma_{\varphi\varphi}(r, \varphi = 0) = K_1 + K_2 r + \dots \tag{5.20}$$

holds. Considering terms up to the second-order yields:

$$\frac{K_1}{\sigma_\infty} = \kappa \left(1 + 2\mathrm{Re} \left[\frac{\mu_2 \left(\frac{\sqrt{-\Lambda^2\mu_1^2}}{\Lambda^2\mu_1^2} + 1 \right)}{2(1 + \mathrm{i}\Lambda\mu_1)(\mu_1 - \mu_2)} + \frac{\mu_1 \left(-\frac{\sqrt{-\Lambda^2\mu_2^2}}{\Lambda^2\mu_2^2} - 1 \right)}{2(1 + \mathrm{i}\Lambda\mu_2)(\mu_1 - \mu_2)} \right] \right), \tag{5.21}$$

$$\frac{K_2}{\sigma_\infty} = 2\mathrm{Re} \left[\frac{\mu_2\sqrt{-\Lambda^2\mu_1^2}(1 - \mathrm{i}\Lambda\mu_1)}{2\Lambda^4\mu_1^4(\mu_1 - \mu_2)} + \frac{\mu_1\sqrt{-\Lambda^2\mu_2^2}(1 - \mathrm{i}\Lambda\mu_2)}{2\Lambda^4\mu_2^4(\mu_2 - \mu_1)} \right] \frac{\kappa}{a}. \tag{5.22}$$

It is observed from Eq. (5.21), that the coefficient K_1 is affected by the dimensionless geometry factor $\Lambda = b/a$. In contrast, K_2 depends also on the absolute value of the half-axis a and hence allows for capturing size effects. In the limiting case of a crack, that is $\Lambda \to 0$, infinite stresses arise showing the presence of a stress singularity right at the crack tip. For $\Lambda \to \infty$, the coefficient K_1 equals one and K_2 vanishes representing the case of a homogeneous stress state with a crack aligned in parallel to the loading direction.

Non-symmetric configuration

In the general case non-symmetric configurations as sketched in Fig. 5.1(b) the stress field associated to the leading-order term $\underline{U}^0$ of the outer expansion contains two linear terms with respect to r:

$$\boldsymbol{\sigma}\left(\underline{U}^0\right) = K_1\boldsymbol{\sigma}_1(\varphi) + K_2^{\mathrm{I}} r\boldsymbol{\sigma}_2^{\mathrm{I}}(\varphi) + K_2^{\mathrm{II}} r\boldsymbol{\sigma}_2^{\mathrm{II}}(\varphi) + o\left(r\right). \tag{5.23}$$

The term with superscript I corresponds to a symmetric deformation mode and the term with superscript II is related to an anti-symmetric mode. The existence of two terms associated to the same exponent $\lambda_2 = 2$ relies on the fact that the coefficient matrix $\mathbf{D}$ in Eq. (5.13) has rank 2:

$$\mathrm{rank}\left(\mathbf{D}(\lambda_2)\right) = 2. \tag{5.24}$$

In the present case, two linear independent eigenvectors $\underline{a}_i$ exist and have to be taken into account. In the special case of a purely symmetric deformation, the intensity factor related to the anti-symmetric case vanishes. Analogous to the symmetric case, the intensity factors in Eq. (5.23) are calculated analytically. First, the stress vector along the potential inclined crack path in the uncracked state according to Eqn. (5.1)-(5.3) as

well as (5.5) is expanded as a Taylor series with respect to r:

$$\begin{pmatrix}\sigma_{\varphi\varphi}(r,\varphi)\\ \tau_{r\varphi}(r,\varphi)\end{pmatrix}_{\varphi=\alpha} = \begin{pmatrix}c_1\\ k_1\end{pmatrix} + r\begin{pmatrix}c_2\\ k_2\end{pmatrix} + o(r). \tag{5.25}$$

The constants c_i and k_i are the coefficients of the Taylor series and α denotes the angle corresponding to the inclined crack path. Second, another representation of the stress vector is given by means of the expansion (5.23):

$$\begin{aligned}\begin{pmatrix}\sigma_{\varphi\varphi}(r,\varphi)\\ \tau_{r\varphi}(r,\varphi)\end{pmatrix}_{\varphi=\alpha} =& K_1\begin{pmatrix}\sigma_{\varphi\varphi,1}(\varphi)\\ \tau_{r\varphi,1}(\varphi)\end{pmatrix}_{\varphi=\alpha} + K_2^{\mathrm{I}}\, r\begin{pmatrix}\sigma^{\mathrm{I}}_{\varphi\varphi,2}(\varphi)\\ \tau^{\mathrm{I}}_{r\varphi,2}(\varphi)\end{pmatrix}_{\varphi=\alpha}\\ &+K_2^{\mathrm{II}}\, r\begin{pmatrix}\sigma^{\mathrm{II}}_{\varphi\varphi,2}(\varphi)\\ \tau^{\mathrm{II}}_{r\varphi,2}(\varphi)\end{pmatrix}_{\varphi=\alpha} + o(r).\end{aligned} \tag{5.26}$$

Comparing coefficients between Eq. (5.25) and (5.26) yields

$$K_1 = \frac{c_1}{\sigma_{\varphi\varphi,1}(\varphi)\big|_{\varphi=\alpha}} = \frac{k_1}{\tau_{r\varphi,1}(\varphi)\big|_{\varphi=\alpha}} \tag{5.27}$$

and

$$\begin{pmatrix}K_2^{\mathrm{I}}\\ K_2^{\mathrm{II}}\end{pmatrix} = \begin{pmatrix}\sigma^{\mathrm{I}}_{\varphi\varphi,2}(\varphi) & \sigma^{\mathrm{II}}_{\varphi\varphi,2}(\varphi)\\ \tau^{\mathrm{I}}_{r\varphi,2}(\varphi) & \tau^{\mathrm{II}}_{r\varphi,2}(\varphi)\end{pmatrix}^{-1}_{\varphi=\alpha}\begin{pmatrix}c_2\\ k_2\end{pmatrix}. \tag{5.28}$$

5.3.2 Inner expansion and matching

In order to capture the solution behaviour in the vicinity of the initiated crack, the stretched dimensionless variable $\rho = r/\Delta a$ is introduced providing a zoom-in view where the crack has unit length. The inner expansion reads ($\Delta a \to 0$):

$$\underline{U}^{\Delta a}(r,\varphi) = \underline{U}^{\Delta a}(\Delta a\rho,\varphi) = F_1(\Delta a)\underline{V}^1(\rho,\varphi) + F_2(\Delta a)\underline{V}^2(\rho,\varphi) + o(F_2(\Delta a)). \tag{5.29}$$

Carrying out the matching principle as outlined in Section 3 yields

$$F_1(\Delta a) = K_1\Delta a, \tag{5.30a}$$

$$\underline{V}^1(\rho,\varphi) \sim \rho\underline{u}_1(\varphi) \quad \text{as} \quad \rho\to\infty \tag{5.30b}$$

and

$$F_2(\Delta a) = K_2^{\mathrm{I}}\Delta a^2, \tag{5.31a}$$

$$\underline{V}^2(\rho,\varphi) \sim \rho^2\underline{u}_2^{\mathrm{I}}(\varphi) \quad \text{as} \quad \rho\to\infty \tag{5.31b}$$

and

$$F_3(\Delta a) = K_2^{\mathrm{II}} \Delta a^2, \tag{5.32a}$$

$$\underline{V}^3(\rho,\varphi) \sim \rho^2 \underline{u}_2^{\mathrm{II}}(\varphi) \quad \text{as} \quad \rho \to \infty. \tag{5.32b}$$

Since the relations in Eqn. (5.30)-(5.32) lead to ill-posed problems due to unbounded energy, the superposition principle according to

$$\underline{V}^1(\rho,\varphi) = \rho \underline{u}_1(\varphi) + \hat{\underline{V}}_1(\rho,\varphi), \tag{5.33}$$

$$\underline{V}^2(\rho,\varphi) = \rho^2 \underline{u}_2^{\mathrm{I}}(\varphi) + \hat{\underline{V}}_2(\rho,\varphi), \tag{5.34}$$

$$\underline{V}^3(\rho,\varphi) = \rho^2 \underline{u}_2^{\mathrm{II}}(\varphi) + \hat{\underline{V}}_3(\rho,\varphi) \tag{5.35}$$

is applied. The functions $\hat{\underline{V}}_i$ vanish at infinity and are solutions to well-posed problems. More precisely, $\hat{\underline{V}}_i$ satisfy the underlying field equations of linear elasticity subjected to the following boundary conditions on the crack faces $\partial\Omega_{\mathrm{C}}$:

$$\left.\begin{aligned} \boldsymbol{\sigma}(\hat{\underline{V}}_1)\cdot\underline{n} &= -\boldsymbol{\sigma}(\rho\,\underline{u}_1(\varphi))\cdot\underline{n} \\ \boldsymbol{\sigma}(\hat{\underline{V}}_2)\cdot\underline{n} &= -\boldsymbol{\sigma}(\rho^2\underline{u}_2^{\mathrm{I}}(\varphi))\cdot\underline{n} \\ \boldsymbol{\sigma}(\hat{\underline{V}}_3)\cdot\underline{n} &= -\boldsymbol{\sigma}(\rho^2\underline{u}_2^{\mathrm{II}}(\varphi))\cdot\underline{n} \end{aligned}\right\} \quad \text{on} \quad \partial\Omega_{\mathrm{C}}. \tag{5.36}$$

Note, that the functions $\hat{\underline{V}}_i$ are independent of the loading conditions and the global geometry of the structure such as the hole geometry and the plate's width w. Therefore, they can be calculated numerically once for all for a given laminate-layup and crack initiation angle α.

5.3.3 Padé approximation of the incremental energy release rate

The expansion of the unperturbed problem in Eq. (5.23) and the inner expansion in Eq. (5.29) are substituted into the path independent Ψ-integral in order to obtain an expansion for the change in potential energy. Accounting for the bi-linearity of the Ψ-integral and the symmetry property in Eq. (3.59), it follows:

$$\begin{aligned} \frac{\Delta\Pi}{d} = \Psi\left(\underline{U}^{\varepsilon},\underline{U}^{0}\right) &= K_1^2\Delta a^2\,\Psi\left(\rho\underline{u}_1(\varphi)+\hat{\underline{V}}_1(\rho,\varphi),\rho\underline{u}_1(\varphi)\right) \\ &+ 2K_1K_2^{\mathrm{I}}\Delta a^3\,\Psi\left(\rho^2\underline{u}_2^{\mathrm{I}}(\varphi)+\hat{\underline{V}}_2(\rho,\varphi),\rho\underline{u}_1(\varphi)\right) \\ &+ 2K_1K_2^{\mathrm{II}}\Delta a^3\,\Psi\left(\rho^2\underline{u}_2^{\mathrm{II}}(\varphi)+\hat{\underline{V}}_3(\rho,\varphi),\rho\underline{u}_1(\varphi)\right) \\ &+ 2K_2^{\mathrm{I}}K_2^{\mathrm{II}}\Delta a^4\,\Psi\left(\rho^2\underline{u}_2^{\mathrm{II}}(\varphi)+\hat{\underline{V}}_3(\rho,\varphi),\rho^2\underline{u}_2^{\mathrm{I}}(\varphi)\right) \\ &+ \left(K_2^{\mathrm{I}}\right)^2\Delta a^4\,\Psi\left(\rho^2\underline{u}_2^{\mathrm{I}}(\varphi)+\hat{\underline{V}}_2(\rho,\varphi),\rho^2\underline{u}_2^{\mathrm{I}}(\varphi)\right) \\ &+ \left(K_2^{\mathrm{II}}\right)^2\Delta a^4\,\Psi\left(\rho^2\underline{u}_2^{\mathrm{II}}(\varphi)+\hat{\underline{V}}_3(\rho,\varphi),\rho^2\underline{u}_2^{\mathrm{II}}(\varphi)\right). \end{aligned} \tag{5.37}$$

Exploiting the bi-orthogonality property in Eq. (2.61) Eq. (5.37) can be rewritten as

$$\begin{aligned}-\Psi\left(\underline{U}^{\varepsilon},\underline{U}^{0}\right) =& K_1^2\Psi_{11}\Delta a^2 + 2\left(K_1K_2^{\mathrm{I}}\Psi_{12} + K_1K_2^{\mathrm{II}}\Psi_{13}\right)\Delta a^3 \\ &+ \left(\left(K_2^{\mathrm{I}}\right)^2\Psi_{22} + K_2^{\mathrm{I}}K_2^{\mathrm{II}}\Psi_{23} + \left(K_2^{\mathrm{II}}\right)^2\Psi_{33}\right)\Delta a^4 + O(\Delta a^4)\end{aligned} \tag{5.38}$$

with the quantities

$$\begin{aligned}\Psi_{11} &= \Psi\left(\rho\underline{u}_1(\varphi),\hat{\underline{V}}_1(\rho,\varphi)\right), \quad \Psi_{12} = \Psi\left(\rho\underline{u}_1(\varphi),\hat{\underline{V}}_2(\rho,\varphi)\right), \\ \Psi_{13} &= \Psi\left(\rho\underline{u}_1(\varphi),\hat{\underline{V}}_3(\rho,\varphi)\right), \quad \Psi_{23} = \Psi\left(\rho^2\underline{u}_2^{\mathrm{I}}(\varphi),\hat{\underline{V}}_3(\rho,\varphi)\right), \\ \Psi_{22} &= \Psi\left(\rho^2\underline{u}_2^{\mathrm{I}}(\varphi),\hat{\underline{V}}_2(\rho,\varphi)\right), \quad \Psi_{33} = \Psi\left(\rho^2\underline{u}_2^{\mathrm{II}}(\varphi),\hat{\underline{V}}_3(\rho,\varphi)\right).\end{aligned} \tag{5.39}$$

The unknown functions $\hat{\underline{V}}_1, \hat{\underline{V}}_2$ and $\hat{\underline{V}}_3$ involved in the integrals in Eq. (5.39) are defined on the inner domain Ω^{∞} and are calculated numerically using the commercial finite element code Abaqus employing plane stress elements (CPS4). Carefully investigating the expansion (5.38), it turns out that the third term on the right hand side does not represent the complete monomial of fourth-order. As outlined in Section 3, the reason lies in the higher-order correction term $f_1(\varepsilon)\underline{U}^1(r,\varphi)$ within the outer expansion (5.9). Successively carrying out the matching procedure between inner and outer expansion, it follows that $f_1(\varepsilon) = \mathcal{O}\left(\Delta a^2\right)$, cf. Eq. (3.66). This ultimately leads to additional terms of $\mathcal{O}\left(\Delta a^3\right)$ in the expansion of the IERR, cf. Eq-(3.79), which must be properly incorporated. However, accounting for these interaction terms leads to additional BVPs and is not pursued in the subsequent analysis for reasons of efficiency. Hence, only terms up to $\mathcal{O}\left(\Delta a^3\right)$ are retained in Eq. (5.38). The desired expansion of the IERR then takes the form:

$$\bar{\mathcal{G}} = K_1^2\Psi_{11}\Delta a + 2\left(K_1K_2^{\mathrm{I}}\Psi_{12} + K_1K_2^{\mathrm{II}}\Psi_{13}\right)\Delta a^2 + \mathcal{O}(\Delta a^3). \tag{5.40}$$

Thus, three FEA on the inner domain Ω^{∞} have to be performed in order to obtain the scaling coefficient Ψ_{11}, Ψ_{12} and Ψ_{13}. In the absence of mixed-mode conditions where either K_2^{I} or K_2^{II} vanishes, only two FEA are required. Note that due to the anisotropic material the coefficients A_{ij} are not used in their dimensionless form in order to avoid cumbersome expressions. The expansion of the IERR is based on the assumption that the crack length is much smaller than a characteristic structural length, e.g. the notch radius in the present case. In addition to the leading-order term, higher-order terms are taken into account in order to extend the range of validity of the asymptotic solutions. A further improvement can be achieved employing the technique of Padé approximation (Felger et al., 2017a,b, Hinch, 1991). Here, a known power series $F(x) = \sum_{k=0}^{\infty} f_k x^k$ is re-expressed as a rational polynomial. According to Baker and Graves-Morris (1981, 1996), using Padé approximation can lead to an extended domain of convergence compared to a conventional power series expansion. The Padé approximant $R_{m,n}$ is defined as (Baker and Graves-Morris, 1981, 1996)

$$R_{m,n}(x) = \frac{\sum_{i=0}^{m}\xi_i x^i}{\sum_{j=0}^{n}\eta_j x^j}. \tag{5.41}$$

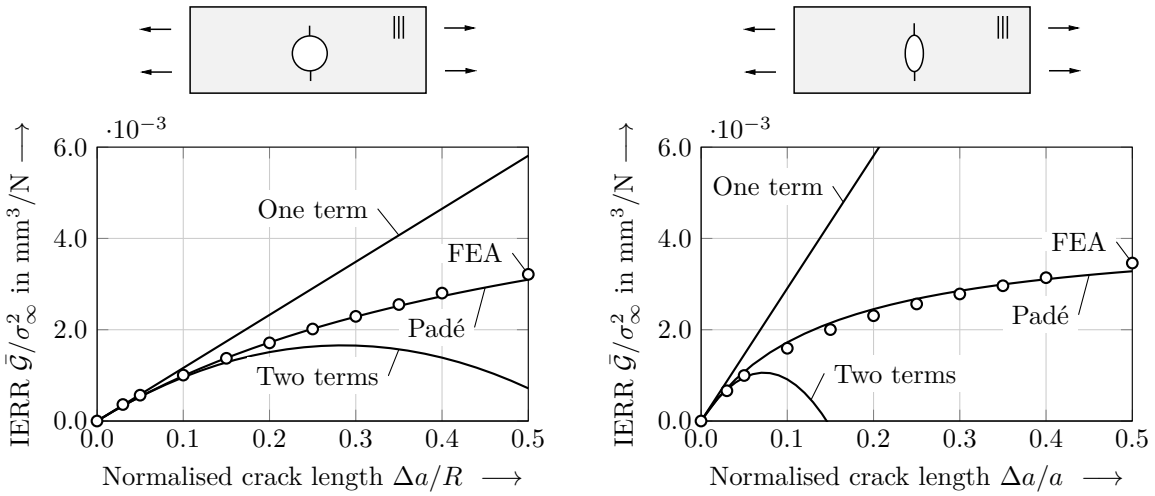

(a) Plate containing a circular hole with radius $R = 2.5$ mm.

(b) Plate containing an elliptical hole with semi-major axis $a = 2b = 2.5$ mm.

Figure 5.3: Incremental energy release rate $\bar{\mathcal{G}}$ of cracked unidirectional open-hole composite plates (90° fibre orientation) with respect to the normalised crack length: Comparison between FEA, power series expansion in Eq. (5.40) and the corresponding Padé approximation. Width $w = 18$ mm. $\Psi_{11} = 0.55 \times 10^{-3}$ mm^2/N, $2\Psi_{12} = 0.47 \times 10^{-3}$ mm^2/N. Material data according to Table A.2.

Without loss of generality B_0 is set equal to zero. The coefficients ξ_i and η_j in Eq. (5.41) can be uniquely determined requiring that

$$F(x) - R_{m,n}(x) = \mathcal{O}\left(x^{m+n+1}\right). \tag{5.42}$$

This yields a linear system of $m+n+1$ equations for the $m+n+1$ unknown coefficients. Let us apply this procedure to the expansion of the IERR in Eq. (5.40). Since the expansion is known up to the quadratic term, the associated $R_{1,1}$ Padé approximant reads:

$$\bar{\mathcal{G}}(\Delta a) \approx R_{1,1}(\Delta a) = \frac{K_1^2 \Psi_{11} \Delta a}{1 - \dfrac{K_1 K_2^{\mathrm{I}} \Psi_{12} + K_1 K_2^{\mathrm{II}} \Psi_{13}}{K_1^2 \Psi_{11}} \Delta a}. \tag{5.43}$$

According to Eq. (5.43), the $R_{1,1}$ Padé approximant is bounded for large crack lengths. This property fits better to the characteristics of the IERR than a power series representation which becomes unbounded for $\Delta a \to \infty$.

In order to assess the accuracy of the proposed asymptotic approach, the expansions (5.40) and (5.43) are compared to fully numerical data. Finite element analyses of the whole open-hole plate are carried out for different crack lengths. Employing a plate of unit-thickness in the numerical model, the IERR is computed numerically relating the change in potential energy $\Delta\Pi$ due to crack formation to the crack length Δa. Consider a 90° unidirectional fibre-reinforced finite-width composite plate containing a hole with

cracks perpendicular to the loading direction as depicted in Fig. 5.3. Since the problem is symmetric, the intensity factor K_2^{II} vanishes and a single quadratic term remains in Eq. (5.40). The IERR for two cracks emanating from a circular hole is plotted in Fig. 5.3(a) with respect to the dimensionless crack length $\Delta a/R$. It is observed, that the linear term of the power series representation correctly captures the slope of $\bar{\mathcal{G}}$ in the region $\Delta a \to 0$. However, the one term expansion is only a suitable approximation for very short cracks. Taking into account the quadratic second-order term on the one hand improves the accuracy of the asymptotic solution for short cracks but on the other hand leads to an unphysical non-monotonic behaviour. This automatically limits the validity range of the two-term expansion to crack lengths $\Delta a < \Delta a^*$ where Δa^* represents the point of maximum IERR ($\Delta a^*/R \approx 0.28$ in Fig. 5.3(a)). A significant improvement is achieved employing the Padé approximant as introduced in Eq. (5.43). This extends the region of validity beyond the bound Δa^* to intermediate crack lengths. The relative error between the numerical reference data and the Padé approximation is smaller than 4% for $\Delta a/R \leq 0.5$. Note that the present asymptotic approach requires only two FEA using the simplified numerical model of the inner domain in order to calculate both coefficients Ψ_{11} and Ψ_{12}. These scaling coefficients depend only on the local geometry of the crack and the material anisotropy. All information concerning the global geometry of the structure, such as the hole geometry, are contained in the asymptotic solution by means of the intensity factors K_i. Importantly, this means that the same coefficients Ψ_{11}, Ψ_{12} can be employed for a circular hole as well as for an elliptical hole. This is demonstrated in Fig. 5.3(b) showing the normalised IERR with respect to the normalised crack length for an aspect ratio $\lambda = b/a = 1/2$ of the ellipse. It is observed that the first two terms of the asymptotic solution adequately render the behaviour for short cracks $\Delta a \leq \Delta a^*$. Due to the stronger stress concentration compared to the circular hole, the slope of $\bar{\mathcal{G}}$ at $\Delta a/a = 0$ increases. In consequence, the error of the first term approximation rapidly increases for longer cracks. Moreover, the upper bound $\Delta a^*/a$ associated to the two-term expansion is shifted to smaller values of $\Delta a/a$. This is not surprising since the characteristic structural length is now the root radius of the ellipse, which affects the admissible length scale of cracks within the asymptotic analysis. However, employing the $R_{1,1}$ Padé approximant significantly extends the region of validity up to intermediate crack lengths with a maximum relative error of 10% compared to the numerical reference data. Not only that the hole's geometry does not affect the coefficients Ψ_{11}, Ψ_{12}, they also remain unchanged varying the opening-to-width ratio ω. This is depicted in Fig. 5.4 showing the IERR with respect to the dimensionless crack length for three different values of $\omega = 2R/w$. The asymptotic solutions are in a very good agreement with the reference data and the effect of the plate's width on the IERR is rendered correctly. A smaller opening-to-width ratio induces higher stresses at the potential crack path along the x_1-axis, thus the IERR increases for a decreasing plate's width. Since Ψ_{11} and Ψ_{12} are constant, the effect of the plate's finite width is captured solely by the intensity factors K_1 and K_2.

In order to examine the influence of material properties on the IERR and the asymptotic approximation, a 0° fibre-reinforced composite plate is considered as well. Figure 5.5 shows a comparison of the IERR between the numerical and the asymptotic results. Since the fibres are aligned parallel to the loading direction, the stress concentration

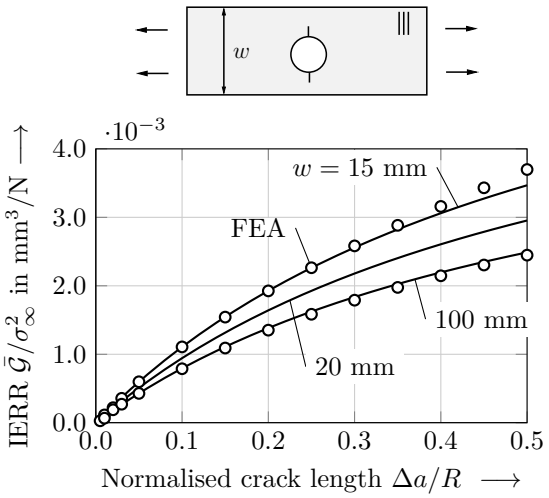

Figure 5.4: Impact of the plate's finite width on the accuracy of the Padé approximation for a 90° fibre orientation. Geometry: hole radius $R = 2.5$ mm, width $w = 15, 20, 100$ mm ($\omega = 1/3, 1/4, 1/20$).

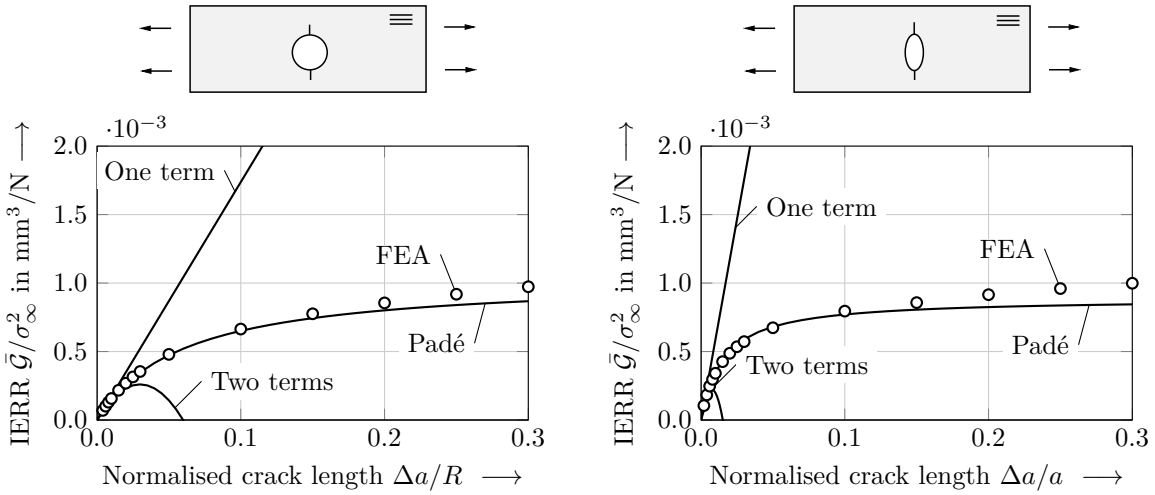

(a) Plate containing a circular hole with radius $R = 2.5$ mm.

(b) Plate containing an elliptical hole with semi-major axis $a = 2b = 2.5$ mm.

Figure 5.5: Incremental energy release rate $\bar{\mathcal{G}}$ of cracked unidirectional open-hole composite plates (0° fibre orientation) with respect to the normalised crack length: Comparison between finite element data, power series expansion in Eq. (5.40) and the corresponding Padé approximation. Width $w = 18$ mm. $\Psi_{11} = 0.18 \times 10^{-3}$ mm²/N, $2\Psi_{12} = 0.14 \times 10^{-3}$ mm²/N. Material data according to Table A.2.

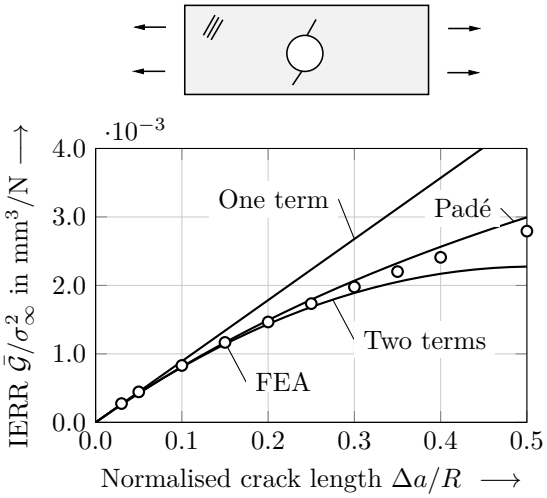

Figure 5.6: Comparison of the IERR of finite sized cracks in a composite plate with a 70° fibre orientation containing a circular hole. Geometry: hole radius $R = 2.5$ mm and width $w = 18$ mm. $\Psi_{11} = 0.60 \times 10^{-3}$ mm^2/N, $\Psi_{12} = 0.51 \times 10^{-3}$ mm^2/N, $\Psi_{13} = 0.44 \times 10^{-3}$ mm^2/N. Material data according to Table A.2.

at the hole becomes stronger compared to the previously discussed case of a 90° fibre orientation. Again, there is a good to fair agreement between the Padé approximation and the reference data with a maximum relative error of 10% in case of the circular hole, cf. Fig. 5.5(a), and 15% for the elliptical hole, Fig. 5.5(b). Note, that the validity range of the asymptotic solution is smaller compared to the 90° case although the geometry of the structure is unchanged. Consequently, the admissible crack length scale associated with the asymptotic approximation does not solely depend on a characteristic structural dimension but is also influenced by the elastic material properties.

Next, the influence of a potential inclination on the accuracy of the Padé approximation is discussed. Consider a unidirectional fibre-reinforced finite-width composite plate. The fibre orientation is 70° and the plate is loaded in off-axis tension which yields asymmetric cracks emanating from the hole according to Fig. 5.6. Since mixed-mode loading conditions prevail, both quadratic terms in the expansion of the IERR have to be considered. Therefore, three finite element calculations on the inner domain are performed to calculate the coefficients Ψ_{11}, Ψ_{12} and Ψ_{13}. As reference solution, FEA of the whole plate with inclined cracks are preformed for 10 different crack lengths. A comparison between the asymptotic approach and the numerical reference data is provided in Fig. 5.6 showing the IERR in dependence of the normalised crack length $\Delta a/R$. It is observed that the Padé approximation is in a good agreement with the numerical data and the effect of the crack's inclination is rendered correctly.

5.4 Prediction of symmetric crack nucleation

In this section, the proposed asymptotic approach is employed to predict the failure loads of laminated composite plates of finite width w containing circular and elliptical holes. The predictions are validated against experimental data by Tan (1988a). Let us consider a plate with a $[90°, 0_2°, 90°]_S$ layup which contains a circular hole with radius R. The ply thickness is 0.14 mm and the material data of the used Hercules graphite/epoxy AS4/3502 prepreg is given in Table A.3. Crack onset is assumed to occur perpendicular to the loading direction according to the material symmetry. Thus, no mixed-mode criterion neither in terms of stresses nor for the energy release is necessary. The elliptical stress criterion yields $\sigma_{\varphi\varphi} = \sigma_c$ and a mode I energy criterion $\bar{\mathcal{G}} = \mathcal{G}_{Ic}$ is used. The coupled criterion reads:

$$\frac{R_{1,1}(\Delta a)}{\sigma^2_{\varphi\varphi}(y = 0, x = \Delta a)} = \frac{\mathcal{G}_{Ic}}{\sigma_c^2}. \tag{5.44}$$

Here, the Padé approximant $R_{1,1}$ is used as representation of the IERR. The corresponding material strength σ_c and fracture toughness $\mathcal{G}_{Ic}$ of the laminate are given in Table A.3. Note, that the relation between the fracture toughness K_{Ic} and $\mathcal{G}_{Ic}$ writes

$$\mathcal{G}_c = -\frac{K_{Ic}^2}{2} S_{22} \operatorname{Im}\left[\frac{\mu_1 + \mu_2}{\mu_1 \mu_2}\right] \tag{5.45}$$

in case of anisotropic material. The relation (5.44) does not depend on the applied load σ_∞ and the resulting finite crack length Δa can be calculated directly. A subsequent evaluation of the stress criterion yields the associated failure stress σ_f. The critical stress at failure of the finite-width plate is shown in Fig. 5.7(a) in dependence of the hole radius R. In the experimental study by Tan (1988a), the plate's opening-to-width ratio $\omega = 2R/w$ was adjusted such that $\omega < 1/3$ holds and the FWC-factor is applicable. Furthermore, the opening-to-width ratio is kept approximately constant. Hence, the specimens are geometrically similar. The predictions are in a good agreement with the experiments except for the data point at $R = 7.75$ mm for which a different failure mode was observed experimentally, cf. Tan (1994). The results show that the normalised failure stress becomes smaller for a larger hole radius. Since the plates are geometrically similar, this effect is also referred to as size effect (Bažant, 1984, 2000). The MAPE between experimental data and the asymptotic approach equals 5.2% excluding the point at $R = 7.75$ mm. For the opening-to-width ratio is kept approximately constant and the specimens are geometrically similar, the failure behaviour exhibits a size effect, that is, a decreasing failure stress for an increasing hole size. The strength predictions based on the proposed asymptotic approach are in an excellent agreement with the fully numerical data for $R \geq 2$ mm with a relative error smaller than 4%. The maximum error occurs for the smallest considered hole size with a relative error of 7.5%. This can be explained by means of Fig. 5.7(b) showing the normalised crack length $\Delta a/R$ with respect to the hole size. It is observed that the normalised crack length increases progressively for a decreasing hole size. For $R \geq 2$ mm, the initiating cracks are smaller than half the plate's radius. This region can be covered by the asymptotic framework

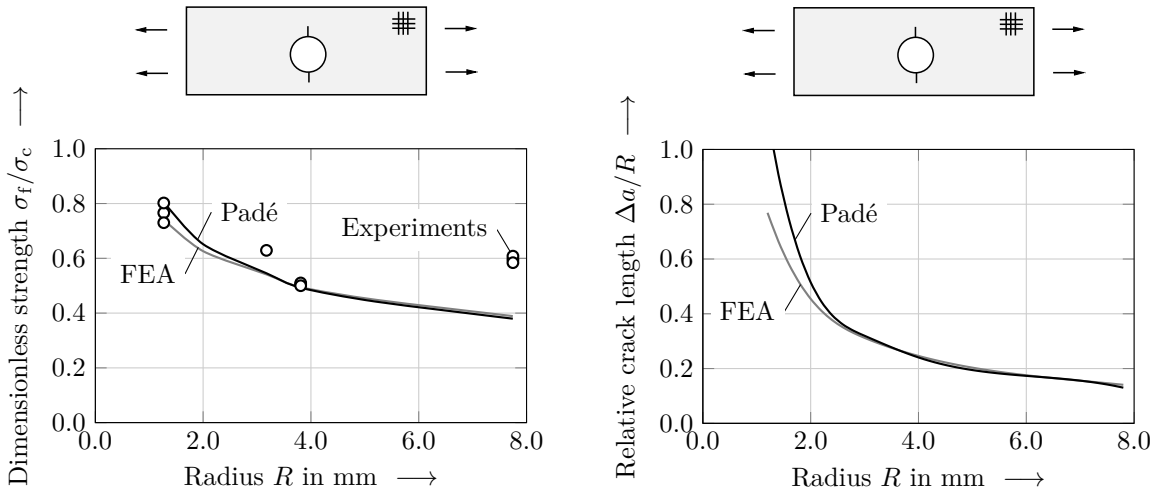

(a) Dimensionless failure stress σ_f/σ_c in dependence of the hole radius R.

(b) Dimensionless crack length $\Delta a/R$ in dependence of the hole radius R.

Figure 5.7: Hole-size effect of a finite-width $[90°, 0_2^\circ, 90°]_S$-composite plate containing a circular hole: Comparison between asymptotic strength predictions, fully numerical data and experimental results by Tan (1988a). Details on the specimens geometry can be found in Tan (1987). Material data according to Table A.3. $\Psi_{11} = 0.41 \times 10^{-4}$ mm^2/N, $2\Psi_{12} = 0.35 \times 10^{-4}$ mm^2/N.

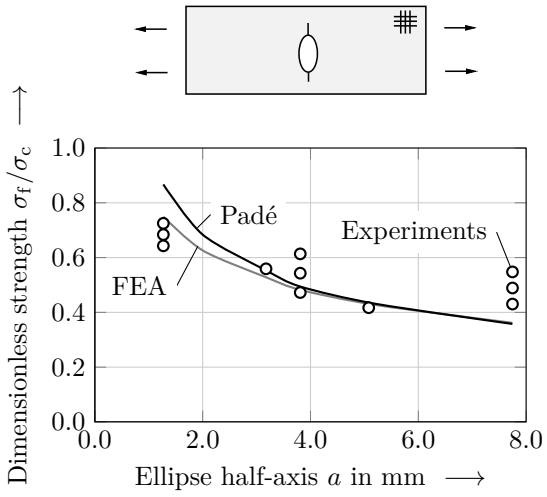

Figure 5.8: Hole-size effect of a finite-width $[90°, 0_2^\circ, 90°]_S$-composite plate containing an elliptical hole with major half-axis a: Comparison between asymptotic strength predictions, fully numerical data and experimental results by Tan (1988a). Details on the specimens geometry can be found in Tan (1987). Material data according to Table A.3. $\Psi_{11} = 0.41 \times 10^{-4}$ mm^2/N, $2\Psi_{12} = 0.35 \times 10^{-4}$ mm^2/N.

using the Padé approximation. If the radius is smaller than 2 mm the underlying shallow-crack asymptote assumption becomes inaccurate since the relative crack lengths are too large. Note, that the values of $\Delta a/R$ according to Fig. 5.7(b) clearly indicate that higher-order terms in combination with the Padé approximation must be taken into account in order to successfully apply the asymptotic methodology. Considering only the first-order term would lead to erroneous predictions.

Consider an elliptically notched laminated composite plate with a $[90°, 0_2^\circ, 90°]_\mathrm{S}$ layup which has been tested experimentally by Tan (1988a). The geometry of the elliptical hole is characterised by $\lambda = b/a = 1/2$ and the corresponding material data are given in Table A.3. The coefficients Ψ_{11} and Ψ_{12} are independent of the plate's geometry and do not have to be re-computed. The effect of the semi-axis a of the ellipse on the failure stress σ_f is shown in Fig. 5.8. The failure predictions based on asymptotics are in a fair agreement with the experimental data and a MAPE of 16.2% is obtained. The asymptotic solution agrees well with the numerical data for $a \geq 3.175\,\mathrm{mm}$ displaying a maximal relative error of 4%. For smaller values of a, the asymptotic approximation becomes less accurate and overestimates the failure load by about 15% for $a = 1.27\,\mathrm{mm}$. The decreasing accuracy with decreasing values of a is caused by the initiation of cracks exceeding the range of validity of the Padé approximation.

5.5 Prediction of anti-symmetric crack formation

In this section, unidirectional flax-fibres/epoxy composite plates under uniaxial tensile loading are considered as used in the work by Modniks et al. (2014). The corresponding material data are given in Table A.2. The plates contain a circular hole of radius $R = 2.5$ mm and have the width $w = 18$ mm and the thickness $d = 1$ mm. Modniks et al. (2014) experimentally investigated the effect of fibre orientation on the plate's effective strength. They observed that inter-fibre failure occurred, that is, the direction of crack initiation coincides with the fibre orientation. Moreover, it was observed that the origin of crack nucleation is located at the x_1-axis in a first-order approximation. This simplification is adopted in the subsequent analysis as depicted in Fig. 5.9. For a fibre orientation α in the range $0° < \alpha < 90°$ the plate is in off-axis tension yielding a mixed-mode fracture problem. To account for mixed-mode effects, the quadratic interaction law according to Eq. (2.66) is used as stress criterion where σ_c and τ_c represent intralaminar strengths in the present case. In addition, an energy criterion capturing effects of mixed-mode conditions on the material toughness and energy dissipation is used. The energy required for crack initiation is computed integrating $\mathcal{G}_c(\chi)$ along the crack path as stated in Eq. (2.74) where χ is the mixed-mode angle, cf. Eq. (2.71). Since the fracture toughness $\mathcal{G}_\mathrm{Ic}$ is larger than $\mathcal{G}_\mathrm{IIc}$ in the present case of UD flax prepreg, the phenomenological law of Hutchinson and Suo (1991) cannot be applied in its original form (García and Leguillon, 2012). Consequently, a modified version essentially representing a linear interaction law is employed:

$$\mathcal{G}_c = \mathcal{G}_\mathrm{Ic}\left(1 - \frac{2}{\pi}\chi\left(1 - \frac{\mathcal{G}_\mathrm{IIc}}{\mathcal{G}_\mathrm{Ic}}\right)\right). \tag{5.46}$$

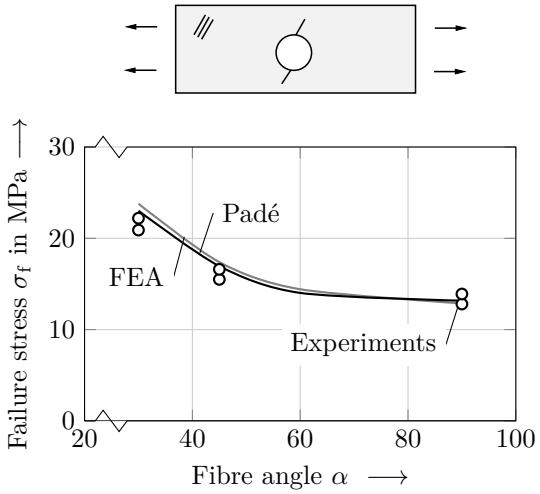

Figure 5.9: Effective strength σ_f with respect to the fibre orientation α of a finite-width UD layer in off-axis tension containing a circular hole of radius $R = 2.5$ mm. Comparison between predictions and experimental data of Modniks et al. (2014). Material data are given in Table A.2.

The criterion is formulated in such a way that pure mode I conditions ($\chi = 0$) correspond to $\mathcal{G}_c = \mathcal{G}_{Ic}$ and pure mode II conditions ($\chi \to \pi/2$) imply $\mathcal{G}_c = \mathcal{G}_{IIc}$.

The failure stress σ_f of the considered unidirectional flax-fibres/epoxy composite plates is plotted in Fig. 5.9 with respect to the fibre orientation α. It is observed that an increasing angle α leads to a decreasing failure stress. For $60° \leq \alpha \leq 90°$, the failure stress is only slightly sensitive to the fibre orientation whereas a stronger impact is observed for $\alpha < 45°$. Changing the fibre angle from 90° to 30° increases the effective strength by 70% under the given loading conditions. The measured failure stress is rendered accurately by the asymptotic approach with a MAPE of 7.3%. Moreover, the asymptotic solution agrees well with the numerical data. It is observed, that the asymptotic approximation becomes slightly less accurate the smaller the value of the fibre angle α. The smallest considered angle $\alpha = 30°$ yields the maximum relative error of 8.3%.

5.6 Remarks and outlook

Supposing brittle fracture, it has been shown that the framework composed of complex potential method, MAE and Padé approximation allows for efficiently predict crack onset in laminated plates even in the case of inclined cracks. Due to the particular structural situation, the point of crack initiation can be assumed to be located on the horizontal x_1-axis, cf. Fig. 5.1, and the crack angle is known a-prior. Dropping these assumptions, it is to emphasize that the present model provides an efficient framework in terms of assessing crack onset at arbitrary locations and inclination angles as well. In this case, a more general optimisation problem has to be solved: the initiation angle is discretised in the range of interest and multiple potential locations where the initial crack formation might take place are considered. Subsequently, solving

Eq. (5.44) yields a set of failure loads out of which the smallest failure load can be determined.

The present model is restricted to the formation of through-thickness cracks which enables a two-dimensional modelling. An extension of the present model to the three-dimensional case would serve as a basis for tackling delamination processes triggered by the laminate free-edge effect at the hole's contour. To this end, classical laminated plate theory and the complex potential method can be employed to approximate the interlaminar shear and normal stresses using a variational approach inspired by the work of Lin and Ko (1992). An additional implementation of a MAE framework seems suitable since the effect of the size of the delaminated area is captured explicitly. However, additional simplifying assumptions on the shape of the crack surface have to be made and it must be carefully checked if the small perturbation assumption still holds. A suitable extension of the present model to tackle delamination processes also offers the possibility to study more general situations such as compressive biaxial loading conditions (Soutis and Fleck, 1990, Williamson et al., 2004, Eriksson and Aronsson, 1990).

The present model also serves as a basis for studying the problem of net-tension failure of mechanically fastened joints in composite laminates (Catalanotti and Camanho, 2013). Based on a suitable stress solution of the uncracked laminate, the coefficients of the Padé approximation can be adapted allowing for a very efficient asymptotic representation of the cracked state and the IERR.

Further applications of the proposed model can be found for instance in geological problems such as fracture initiation in hydraulic fracturing (Bell, 1996, Ito and Hayashi, 1991).

Chapter 6

Summary

In this work, a method to efficiently model and assess brittle crack formation at holes in composite plates and bi-material junctions is provided. The presented methodology combines a complex potential approach to analytically determine the notch stress field and a two-scale matched asymptotic expansions framework to calculate the energy dissipation due to crack formation. This enables an evaluation of the coupled stress and energy criterion with minimal computational effort and finally serves as a basis for a physically sound and effective failure prediction.

Applying this framework to a bi-material butt joint has led to a scaling law of the effective joint strength in terms of the adhesive thickness. This semi-analytical nature of the asymptotic relations preserves valuable physical insights into the underlying fracture mechanics problem, e.g. the fact that the failure load scales sub-linearly with the material's fracture toughness which becomes relevant in terms of assessing uncertainties. A comparison with numerical reference data showed that a leading-order terms asymptotic analysis provides accurate results if the crack lengths are smaller than 10% of the adhesive thickness. A comparison to numerical cohesive zone models and experimental findings from literature proved the validity of the obtained scaling law. The failure behaviour of a T-shaped structure under uniaxial tensile loading has been examined accounting for multiple singular eigenmodes triggering fracture. The failure load and the angle of crack initiation are predicted in a very good agreement with experimental findings. Examining the failure of scarf joint specimens under four-point bending loading showed that two competing failure modes are present: a notch induced failure mode where crack onset is triggered by the stress singularity and a bending failure mode characterised by crack formation in a certain distance from the bi-material point. In terms of notch induced failure, is has been observed that higher-order oscillating eigenfunctions in the asymptotic expansions must be taken into account to obtain accurate predictions. In comparison with experimental data, the load at failure is predicted accurately with a relative error smaller than 9%. Further, the predicted angle of crack initiation as well as the location of crack onset are in close agreement with experiments.

The asymptotic approach is then transferred to the situation of an open-hole fibre-reinforced composite plate of finite width under uniaxial tensile loading. The stress field in the state prior to fracture is determined by means of the method of complex potentials in combination with a finite-width correction factor. In order to adequately capture the incremental energy release rate, higher-order terms are employed. The power-series representation of the rate of energy dissipation allows for using the concept of Padé approximation. In agreement with numerical reference data, this significantly

improves the convergence of the asymptotic series and crack lengths in the range of the hole radius can be captured correctly. In comparison with numerical reference data it is shown that the effect of the plate's finite width, the hole geometry, a potential crack inclination and the material anisotropy on the incremental energy release rate is captured correctly. The obtained semi-analytical relations for the stress and energy quantities are used to predict failure of open-hole composite plates. First, laminates with a $[90°, 0_2^\circ, 90°]_S$ layup containing a circular or elliptical hole are considered where two symmetric cracks nucleate at the hole perpendicular to the loading direction. For nearly geometrically similar structures, a larger hole dimension decreases the plate's effective strength. This size effect is rendered correctly by the asymptotic approach. Second, the effect of fibre orientation on the failure load is examined by employing a unidirectional fibre-reinforced layer. If the fibre orientation does not correspond to the load direction the plate is in off-axis tension inducing intralaminar cracking in the composite. The proposed semi-analytical approach allows for capturing the formation of inclined cracks emanating from the hole and enables a precise failure prediction. In agreement with experiments, the model has shown that the plate's effective strength can be increased by 70% adjusting the fibre orientation.

Comments and outlooks regarding an extension of the presented model as well as additional possible fields of application can be found at the end of each section.

Appendix A

Table A.1: Material properties of PMMA, epoxy adhesive, Rohacell 51, steel and aluminum.

	E in GPa	ν -	σ_c in MPa	τ_c in MPa	$\mathcal{G}_{Ic}$ in N/mm
PMMA (Dunn et al., 1997c)	2.3	0.36	69.8	40.3*	
PMMA (Seweryn et al., 1997)	3.3	0.35	102.8	59.4*	0.384
Epoxy (Reedy and Guess, 1993)	3.5	0.35	59	34.1*	0.015
Rohacell 51 (Burman, 1998)	0.085	0.42	1.6	0.8	0.069
Steel (Reedy and Guess, 1997)	207	0.3			
Aluminum (Reedy and Guess, 1997)	69	0.33			

$*$ estimate using von Mises hypotheses

Table A.2: Elastic ply properties and intra-laminar strength and toughness of a unidirectional flax-fibres/epoxy composite plate from Modniks et al. (2014).

E_1 in GPa	E_2 in GPa	G_{12} in GPa	ν_{12} -	$\sigma_{nn,c}$ in MPa	$\sigma_{nt,c}$ in MPa	$\mathcal{G}_{Ic}$ in N/mm	$\mathcal{G}_{IIc}$ in N/mm
26.5	2.6	1.3	0.35	20.25	17.28	0.622	0.472

Table A.3: Elastic ply properties of Hercules graphite/epoxy AS4/3502 lamina and fracture parameters for a $[90°, 0_2°, 90°]_S$ layup from Tan (1988a).

E_1 in GPa	E_2 in GPa	G_{12} in GPa	ν_{12} -	σ_c in MPa	K_{Ic} in MPa $\sqrt{m}$
143.89	11.86	6.69	0.326	974	49.6*

$*$ mean value

Bibliography

V. Acary and Y. Monerie. *Nonsmooth fracture dynamics using a cohesive zone approach*. PhD thesis, INRIA, 2005.

A. Akisanya and N. Fleck. Interfacial cracking from the free-edge of a long bi-material strip. *International Journal of Solids and Structures*, 34(13):1645–1665, 1997.

R. Alessi, S. Vidoli, and L. De Lorenzis. A phenomenological approach to fatigue with a variational phase-field model: The one-dimensional case. *Engineering Fracture Mechanics*, 190:53–73, 2018.

G. Anderson and K. DeVries. Predicting strength of adhesive joints from test results. *International Journal of Fracture*, 39(1-3):191–200, 1989.

ASTM D2095. *Standard Test Method for Tensile Strength of Adhesives by Means of Bar and Rod Specimens*. ASTM International, West Conshohocken, Philadelphia, USA, 2015.

ASTM D897. *Standard Test Method for Tensile Properties of Adhesive Bonds*. ASTM International, West Conshohocken, Philadelphia, USA, 2016.

M. Ayatollahi, A. Torabi, and A. Rahimi. Brittle fracture assessment of engineering components in the presence of notches: a review. *Fatigue & Fracture of Engineering Materials & Structures*, 39(3):267–291, 2016.

G. A. Baker and P. R. Graves-Morris. *Padé approximants. Part 1: Basic theory*, volume 1. Encyclopedia of Mathematics and its Applications, Reading, Mass.: Addison-Wesley, 1981.

G. A. Baker and P. R. Graves-Morris. *Padé approximants*, volume 59. Cambridge University Press, 1996.

L. Banks-Sills and A. Sherer. A conservative integral for determining stress intensity factors of a bimaterial notch. *International Journal of Fracture*, 115(1):1–25, 2002.

G. I. Barenblatt. The formation of equilibrium cracks during brittle fracture. general ideas and hypotheses. axially-symmetric cracks. *Journal of Applied Mathematics and Mechanics*, 23(3):622–636, 1959.

G. I. Barenblatt and B. G. Isaakovich. *Scaling, self-similarity, and intermediate asymptotics: dimensional analysis and intermediate asymptotics*, volume 14. Cambridge University Press, 1996.

Z. P. Bažant. Size effect in blunt fracture: concrete, rock, metal. *Journal of Engineering Mechanics*, 110(4):518–535, 1984.

Z. P. Bažant. Size effect. *International Journal of Solids and Structures*, 37(1-2):69–80, 2000.

W. Becker. Complex method for the elliptical hole in an unsymmetric laminate. *Archive of Applied Mechanics*, 63(3):159–169, 1993.

W. Becker and D. Gross. *Mechanik elastischer Körper und Strukturen*. Berlin - Heidelberg - New York: Springer Verlag, 2002.

J. Bell. In situ stresses in sedimentary rocks (part 1): measurement techniques. *Geoscience Canada*, 23(2), 1996.

J. Bleyer and R. Alessi. Phase-field modeling of anisotropic brittle fracture including several damage mechanisms. *Computer Methods in Applied Mechanics and Engineering*, 336:213–236, 2018.

K. B. Broberg. *Cracks and fracture*. Academic Press, 1999.

M. Burman. *Fatigue crack initiation and propagation in sandwich structures*. PhD thesis, KTH, Stockholm, 1998.

W. Burton and G. Sinclair. On the singularities in Reissner's theory for the bending of elastic plates. *Journal of Applied Mechanics*, 53(1):220–222, 1986.

P. Camanho, G. Erçin, G. Catalanotti, S. Mahdi, and P. Linde. A finite fracture mechanics model for the prediction of the open-hole strength of composite laminates. *Composites Part A: Applied Science and Manufacturing*, 43(8):1219–1225, 2012.

R. D. Campilho, M. De Moura, A. Barreto, J. Morais, and J. Domingues. Fracture behaviour of damaged wood beams repaired with an adhesively-bonded composite patch. *Composites Part A: Applied Science and Manufacturing*, 40(6-7):852–859, 2009.

R. D. Campilho, M. Banea, J. Neto, and L. Da Silva. Modelling of single-lap joints using cohesive zone models: effect of the cohesive parameters on the output of the simulations. *The Journal of Adhesion*, 88(4-6):513–533, 2012.

R. D. Campilho, M. Banea, J. Neto, and L. Da Silva. Modelling adhesive joints with cohesive zone models: effect of the cohesive law shape of the adhesive layer. *International Journal of Adhesion and Adhesives*, 44:48–56, 2013.

W. C. Carpenter. Calculation of fracture mechanics parameters for a general corner. *International Journal of Fracture*, 24(1):45–58, 1984a.

W. C. Carpenter. A collocation procedure for determining fracture mechanics parameters at a corner. *International Journal of Fracture*, 24(4):255–266, 1984b.

A. Carpinteri. Notch sensitivity in fracture testing of aggregative materials. *Engineering Fracture Mechanics*, 16(4):467–481, 1982.

A. Carpinteri. Stress-singularity and generalized fracture toughness at the vertex of re-entrant corners. *Engineering Fracture Mechanics*, 26(1):143–155, 1987.

A. Carpinteri, P. Cornetti, N. Pugno, A. Sapora, and D. Taylor. A finite fracture mechanics approach to structures with sharp V-notches. *Engineering Fracture Mechanics*, 75(7):1736–1752, 2008.

A. Carpinteri, P. Cornetti, and A. Sapora. Brittle failures at rounded V-notches: a finite fracture mechanics approach. *International Journal of Fracture*, 172(1):1–8, 2011.

N. Carrère, E. Martin, and D. Leguillon. Comparison between models based on a coupled criterion for the prediction of the failure of adhesively bonded joints. *Engineering Fracture Mechanics*, 138:185–201, 2015.

G. Catalanotti and P. Camanho. A semi-analytical method to predict net-tension failure of mechanically fastened joints in composite laminates. *Composites Science and Technology*, 76:69–76, 2013.

G. Cherepanov. *Mechanics of brittle fracture*. McGraw-Hill, New York, 1979.

P. Cornetti, D. Taylor, and A. Carpinteri. An asymptotic matching approach to shallow-notched structural elements. *Engineering Fracture Mechanics*, 77(2):348–358, 2010.

P. Cornetti, V. Mantič, and A. Carpinteri. Finite fracture mechanics at elastic interfaces. *International Journal of Solids and Structures*, 49(7):1022–1032, 2012.

L. F. M. da Silva and R. D. Campilho. *Advances in numerical modelling of adhesive joints*. Springer, 2012.

L. F. M. da Silva, T. Rodrigues, M. A. V. Figueiredo, M. F. S. F. de Moura, and J. A. G. Chousal. Effect of adhesive type and thickness on the lap shear strength. *The Journal of Adhesion*, 82(11):1091–1115, 2006.

C. Davila, P. Camanho, and M. de Moura. Mixed-mode decohesion elements for analysis of progressive delamination. 42nd AIAA. ASME/ASCE/AHS/ASC structures, Structural Dynamics and Materials Conference, 2001.

J. Dempsey and G. Sinclair. On the singular behavior at the vertex of a bi-material wedge. *Journal of Elasticity*, 11(3):317–327, 1981.

A. Doitrand and D. Leguillon. Comparison between 2d and 3d applications of the coupled criterion to crack initiation prediction in scarf adhesive joints. *International Journal of Adhesion and Adhesives*, 85:69–76, 2018.

S. Dölling, S. Hell, and W. Becker. Investigation of the laminate free-edge effect by means of the scaled boundary finite element method. *PAMM*, 18(1), 2018.

M. L. Dunn, W. Suwito, and S. Cunningham. Fracture initiation at sharp notches: correlation using critical stress intensities. *International Journal of Solids and Structures*, 34(29):3873–3883, 1997a.

M. L. Dunn, W. Suwito, and S. Cunningham. Stress intensities at notch singularities. *Engineering Fracture Mechanics*, 57(4):417–430, 1997b.

M. L. Dunn, W. Suwito, S. Cunningham, and C. W. May. Fracture initiation at sharp notches under mode I, mode II, and mild mixed mode loading. *International Journal of Fracture*, 84(4):367, 1997c.

M. Elices, G. Guinea, J. Gomez, and J. Planas. The cohesive zone model: advantages, limitations and challenges. *Engineering Fracture Mechanics*, 69(2):137–163, 2002.

G. Erçin, P. Camanho, J. Xavier, G. Catalanotti, S. Mahdi, and P. Linde. Size effects on the tensile and compressive failure of notched composite laminates. *Composite Structures*, 96:736–744, 2013.

I. Eriksson and C. G. Aronsson. Strength of tensile loaded graphite/epoxy laminates containing cracks, open and filled holes. *Journal of Composite Materials*, 24(5): 456–482, 1990.

J. Eshelby, W. Read, and W. Shockley. Anisotropic elasticity with applications to dislocation theory. *Acta metallurgica*, 1(3):251–259, 1953.

M. L. Falk, A. Needleman, and J. R. Rice. A critical evaluation of cohesive zone models of dynamic fractur. *Le Journal de Physique IV*, 11(5):5–43, 2001.

J. Felger and W. Becker. Asymptotic analysis of notch induced crack nucleation. *PAMM*, 17(1):239–240, 2017a.

J. Felger and W. Becker. A complex potential method for the asymptotic solution of wedge problems using first-order shear deformation plate theory. *European Journal of Mechanics-A/Solids*, 61:383–392, 2017b.

J. Felger, N. Stein, and W. Becker. Asymptotic finite fracture mechanics solution for crack onset at elliptical holes in composite plates of finite-width. *Engineering Fracture Mechanics*, 182:621–634, 2017a.

J. Felger, N. Stein, and W. Becker. Mixed-mode fracture in open-hole composite plates of finite-width: an asymptotic coupled stress and energy approach. *International Journal of Solids and Structures*, 122-123:14–24, 2017b.

J. Felger, P. L. Rosendahl, D. Leguillon, and W. Becker. Predicting crack patterns at bi-material junctions: A coupled stress and energy approach. *International Journal of Solids and Structures*, 164:191–201, 2019a.

J. Felger, N. Stein, C. Frey, and W. Becker. Scaling laws for the adhesive composite butt joint strength derived by finite fracture mechanics. *Composite Structures*, 208: 546–556, 2019b.

S. Filippi, P. Lazzarin, and R. Tovo. Developments of some explicit formulas useful to describe elastic stress fields ahead of notches in plates. *International Journal of Solids and Structures*, 39(17):4543–4565, 2002.

G. A. Francfort and J.-J. Marigo. Revisiting brittle fracture as an energy minimization problem. *Journal of the Mechanics and Physics of Solids*, 46(8):1319–1342, 1998.

I. García and D. Leguillon. Mixed-mode crack initiation at a V-notch in presence of an adhesive joint. *International Journal of Solids and Structures*, 49(15):2138–2149, 2012.

F. Gómez and M. Elices. A fracture criterion for sharp V-notched samples. *International Journal of Fracture*, 123(3-4):163–175, 2003a.

F. Gómez and M. Elices. Fracture of components with V-shaped notches. *Engineering Fracture Mechanics*, 70(14):1913–1927, 2003b.

F. Gómez, M. Elices, F. Berto, and P. Lazzarin. Fracture of V-notched specimens under mixed mode (I+ II) loading in brittle materials. *International Journal of Fracture*, 159(2):121, 2009.

J. Gonçalves, M. De Moura, P. De Castro, and A. Marques. Interface element including point-to-surface constraints for three-dimensional problems with damage propagation. *Engineering Computations*, 17(1):28–47, 2000.

A. A. Griffith. The phenomena of rupture and flow in solids. *Philosophical Transactions of the Royal Society of London. Series A, containing papers of a mathematical or physical character*, 221(582-593):163–198, 1921.

D. Gross and T. Seelig. *Fracture mechanics: with an introduction to micromechanics*. Springer, 2017.

H. Groth. Stress singularities and fracture at interface corners in bonded joints. *International Journal of Adhesion and Adhesives*, 8(2):107–113, 1988.

P. A. Gustafson and A. M. Waas. The influence of adhesive constitutive parameters in cohesive zone finite element models of adhesively bonded joints. *International Journal of Solids and Structures*, 46(10):2201–2215, 2009.

Z. Hashin. Finite thermoelastic fracture criterion with application to laminate cracking analysis. *Journal of the Mechanics and Physics of Solids*, 44(7):1129–1145, 1996.

J. Hebel, R. Dieringer, and W. Becker. Modelling brittle crack formation at geometrical and material discontinuities using a finite fracture mechanics approach. *Engineering Fracture Mechanics*, 77(18):3558–3572, 2010.

S. Hell and W. Becker. The scaled boundary finite element method for the analysis of 3d crack interaction. *Journal of Computational Science*, 9:76–81, 2015.

S. Hell, P. Weißgraeber, J. Felger, and W. Becker. A coupled stress and energy criterion for the assessment of crack initiation in single lap joints: a numerical approach. *Engineering Fracture Mechanics*, 117:112–126, 2014.

C. Henninger, D. Leguillon, and E. Martin. Crack initiation at a V-notch—comparison between a brittle fracture criterion and the Dugdale cohesive model. *Comptes Rendus Mécanique*, 335(7):388–393, 2007.

E. J. Hinch. *Perturbation methods*. Cambridge University Press, 1991.

M. Hofacker and C. Miehe. Continuum phase field modeling of dynamic fracture: variational principles and staggered FE implementation. *International Journal of Fracture*, 178(1-2):113–129, 2012.

M. Hrstka, T. Profant, and M. Kotoul. Electro-mechanical singularities of piezoelectric bi-material notches and cracks. *Engineering Fracture Mechanics*, 216:1–23, 2019.

J. W. Hutchinson and Z. Suo. Mixed mode cracking in layered materials. *Advances in Applied Mechanics*, 29:63–191, 1991.

G. R. Irwin. Analysis of stresses and strains near the end of a crack traversing a plate. *Journal of Applied Mechanics*, 1957.

T. Ito and K. Hayashi. Physical background to the breakdown pressure in hydraulic fracturing tectonic stress measurements. In *International Journal of Rock Mechanics and Mining Sciences & Geomechanics Abstracts*, volume 28, pages 285–293. Elsevier, 1991.

M. F. Kanninen and C. H. Popelar. *Advanced fracture mechanics*. Number 15. Oxford University Press, 1985.

S. Kaplun. The role of coordinate systems in boundary-layer theory. *Zeitschrift für angewandte Mathematik und Physik ZAMP*, 5(2):111–135, 1954.

A. Kazberuk, M. P. Savruk, and A. B. Chornenkyi. Stress distribution at sharp and rounded V-notches in quasi-orthotropic plane. *International Journal of Solids and Structures*, 85:134–143, 2016.

G. Kirsch. *Die Theorie der Elastizität und die Bedürfnisse der Festigkeitslehre*. Springer, 1898.

G. Kolosov. On an application of complex function theory to a plane problem of the mathematical theory of elasticity. *Yuriev, Russia*, 1909.

P. E. Labossiere and M. L. Dunn. Prediction of fracture initiation at three-dimensional bimaterial interface corners: Application to butt-joints loaded in bending. In *ICF10, Honolulu (USA) 2001*, 2001.

P. Lagerstrom and J. Cole. Examples illustrating expansion procedures for the Navier-Stokes equations. *Journal of Rational Mechanics and Analysis*, 4:817–882, 1955.

P. Lazzarin and F. Berto. Some expressions for the strain energy in a finite volume surrounding the root of blunt V-notches. *International Journal of Fracture*, 135(1-4): 161–185, 2005.

P. Lazzarin and R. Tovo. A unified approach to the evaluation of linear elastic stress fields in the neighborhood of cracks and notches. *International Journal of Fracture*, 78(1):3–19, 1996.

P. Lazzarin and R. Zambardi. A finite-volume-energy based approach to predict the static and fatigue behavior of components with sharp V-shaped notches. *International Journal of Fracture*, 112(3):275–298, 2001.

P. Lazzarin, M. Zappalorto, and F. Berto. Generalised stress intensity factors for rounded notches in plates under in-plane shear loading. *International Journal of Fracture*, 170(2):123, 2011.

J.-L. Le, Z. P. Bažant, and Q. Yu. Scaling of strength of metal-composite joints—Part II: Interface fracture analysis. *Journal of Applied Mechanics*, 77(1):1–7, 2010.

J. Le Pavic, G. Stamoulis, T. Bonnemains, D. Da Silva, and D. Thévenet. Determination of the failure load of adhesive bonding by using a coupled criterion. In *23ème Congrès français de mécanique-CFM*, 2017.

D. Leguillon. Asymptotic and numerical analysis of a crack branching in non-isotropic materials. *European Journal of Mechanics. A. Solids*, 12(1):33–51, 1993.

D. Leguillon. Asymptotic analysis of a spontaneous crack growth. application to a blunt crack. In *IUTAM Symposium on Non-linear Singularities in Deformation and Flow*, pages 169–180. Springer, 1999.

D. Leguillon. Strength or toughness? A criterion for crack onset at a notch. *European Journal of Mechanics-A/Solids*, 21(1):61–72, 2002.

D. Leguillon. An attempt to extend the 2d coupled criterion for crack nucleation in brittle materials to the 3d case. *Theoretical and Applied Fracture Mechanics*, 74:7–17, 2014.

D. Leguillon and E. Sanchez-Palencia. *Computation of singular solutions in elliptic problems and elasticity*. John Wiley & Sons, Inc., 1987.

D. Leguillon and Z. Yosibash. Crack onset at a V-notch. Influence of the notch tip radius. *International Journal of Fracture*, 122(1-2):1–21, 2003.

D. Leguillon and Z. Yosibash. Failure initiation at V-notch tips in quasi-brittle materials. *International Journal of Solids and Structures*, 122:1–13, 2017.

D. Leguillon, C. Lacroix, and E. Martin. Interface debonding ahead of a primary crack. *Journal of the Mechanics and Physics of Solids*, 48(10):2137–2161, 2000a.

D. Leguillon, C. Lacroix, and É. Martin. Matrix crack deflection at an interface between a stiff matrix and a soft inclusion. *Comptes Rendus de l'Académie des Sciences-Series IIB-Mechanics-Physics-Astronomy*, 328(1):19–24, 2000b.

D. Leguillon, C. Lacroix, and E. Martin. Crack deflection by an interface–asymptotics of the residual thermal stresses. *International Journal of Solids and Structures*, 38 (42-43):7423–7445, 2001.

D. Leguillon, J. Laurencin, and M. Dupeux. Failure initiation in an epoxy joint between two steel plates. *European Journal of Mechanics-A/Solids*, 22(4):509–524, 2003.

D. Leguillon, E. Martin, O. Sevecek, and R. Bermejo. What is the tensile strength of a ceramic to be used in numerical models for predicting crack initiation? *International Journal of Fracture*, 212(1):89–103, 2018.

S. Lekhnitskii. *Theory of elasticity of an anisotropic elastic body*. Holden-Day, Inc.: San Francisco, 1963.

T. Li, J.-J. Marigo, D. Guilbaud, and S. Potapov. Gradient damage modeling of brittle fracture in an explicit dynamics context. *International Journal for Numerical Methods in Engineering*, 108(11):1381–1405, 2016.

C.-C. Lin and C.-C. Ko. Method for calculating the interlaminar stresses in symmetric laminates containing a circular hole. *AIAA journal*, 30(1):197–204, 1992.

K. Lin and P. Tong. Singular finite elements for the fracture analysis of V-notched plate. *International Journal for Numerical Methods in Engineering*, 15(9):1343–1354, 1980.

C. Luangarpa and H. Koguchi. Analysis of singular stresses at a vertex and along a singular line in three-dimensional bonded joints using a conservative integral. *European Journal of Mechanics-A/Solids*, 60:208–216, 2016.

G. Maier, M. Bocciarelli, G. Bolzon, and R. Fedele. Inverse analyses in fracture mechanics. *International Journal of Fracture*, 138(1-4):47–73, 2006.

V. Mantič. Interface crack onset at a circular cylindrical inclusion under a remote transverse tension. Application of a coupled stress and energy criterion. *International Journal of Solids and Structures*, 46(6):1287–1304, 2009.

G. Marsh. Airbus A350 xwb update. *Reinforced plastics*, 54(6):20–24, 2010.

E. Martin, D. Leguillon, and N. Carrère. A twofold strength and toughness criterion for the onset of free-edge shear delamination in angle-ply laminates. *International Journal of Solids and Structures*, 47(9):1297–1305, 2010.

E. Martin, D. Leguillon, and N. Carrère. A coupled strength and toughness criterion for the prediction of the open hole tensile strength of a composite plate. *International Journal of Solids and Structures*, 49(26):3915–3922, 2012.

E. Martin, T. Vandellos, D. Leguillon, and N. Carrère. Initiation of edge debonding: coupled criterion versus cohesive zone model. *International Journal of Fracture*, 199 (2):157–168, 2016.

C. Miehe and S. Mauthe. Phase field modeling of fracture in multi-physics problems. part iii. crack driving forces in hydro-poro-elasticity and hydraulic fracturing of fluid-saturated porous media. *Computer Methods in Applied Mechanics and Engineering*, 304:619–655, 2016.

H. Ming-Yuan and J. W. Hutchinson. Crack deflection at an interface between dissimilar elastic materials. *International Journal of Solids and Structures*, 25(9):1053–1067, 1989.

C. Mittelstedt and W. Becker. Asymptotic analysis of stress singularities in composite laminates by the boundary finite element method. *Composite Structures*, 71(2): 210–219, 2005.

C. Mittelstedt and W. Becker. Efficient computation of order and mode of three-dimensional stress singularities in linear elasticity by the boundary finite element method. *International Journal of Solids and Structures*, 43(10):2868–2903, 2006.

C. Mittelstedt and W. Becker. *Strukturmechanik ebener Laminate*. Studienbereich Mechanik, Technische Universität Darmstadt, 2016.

J. Modniks, E. Spārniņš, J. Andersons, and W. Becker. Analysis of the effect of a stress raiser on the strength of a UD flax/epoxy composite in off-axis tension. *Journal of Composite Materials*, 49(9):1071–1080, 2014.

A. Müller, J. Wenck, S. Goswami, J. Lindemann, J. Hohe, and W. Becker. The boundary finite element method for predicting directions of cracks emerging from notches at bimaterial junctions. *Engineering Fracture Mechanics*, 72(3):373–386, 2005.

M. Muñoz-Reja, L. Távara, V. Mantič, and P. Cornetti. Crack onset and propagation at fibre–matrix elastic interfaces under biaxial loading using finite fracture mechanics. *Composites Part A: Applied Science and Manufacturing*, 82:267–278, 2016.

G. Murakami. A stress singularity parameter approach for evaluating the interfacial reliability of plastic encapsulated LSI devices. *Journal of Electronic Packaging*, 111: 243, 1989.

S. Murer and D. Leguillon. Static and fatigue failure of quasi-brittle materials at a V-notch using a Dugdale model. *European Journal of Mechanics-A/Solids*, 29(2): 109–118, 2010.

N. Muskhelishvili. *Some basic problems of the mathematical theory of elasticity*, volume 1. Noordhoff, Groningen, 1963.

H. Neuber. Zur Theorie der Kerbwirkung bei Biegung und Schub. *Archive of Applied Mechanics*, 5(3):238–244, 1934.

H. Neuber. *Kerbspannungslehre, Grundlagen für genaue Festigkeitsrechnung, 2. Aufl. Berlin, Göttingen*. Heidelberg: Springer-Verlag, 1958.

V. Novozhilov. On a necessary and sufficient criterion for brittle strength. *Journal of Applied Mathematics and Mechanics*, 33(2):201–210, 1969.

D. Quesada, D. Leguillon, and C. Putot. Multiple failures in or around a stiff inclusion embedded in a soft matrix under a compressive loading. *European Journal of Mechanics-A/Solids*, 28(4):668–679, 2009.

J. N. Reddy. *Mechanics of Laminated Composite Plates and Shells: Theory and Analysis*. Boca Raton: CRC press, 2004.

E. Reedy . Asymptotic interface corner solutions for butt tensile joints. *International Journal of Solids and Structures*, 30:767–777, 1993.

E. Reedy. Strength of butt and sharp-cornered joints. In *The Mechanics of Adhesion*, pages 145–192. Elsevier New York, NY, 2002.

E. Reedy and T. Guess. Comparison of butt tensile strength data with interface corner stress intensity factor prediction. *International Journal of Solids and Structures*, 30 (21):2929–2936, 1993.

E. Reedy and T. Guess. Butt joint tensile strength: interface corner stress intensity factor prediction. *Journal of Adhesion Science and Technology*, 9(2):237–251, 1995.

E. Reedy and T. Guess. Interface corner failure analysis of joint strength: effect of adherend stiffness. *International Journal of Fracture*, 88(4):305–314, 1997.

S. Ribeiro-Ayeh and S. Hallström. Strength prediction of beams with bi-material butt-joints. *Engineering Fracture Mechanics*, 70(12):1491–1507, 2003.

J. R. Rice. Mathematical analysis in the mechanics of fracture. *Fracture: an advanced treatise*, 2:191–311, 1968.

J. R. Rice and G. C. Sih. Plane problems of cracks in dissimilar media. *Journal of Applied Mechanics*, 32(2):418–423, 1965.

R. Romani, M. Bornert, D. Leguillon, R. Le Roy, and K. Sab. Detection of crack onset in double cleavage drilled specimens of plaster under compression by digital image correlation–theoretical predictions based on a coupled criterion. *European Journal of Mechanics-A/Solids*, 51:172–182, 2015.

P. L. Rosendahl, P. Weißgraeber, N. Stein, and W. Becker. Asymmetric crack onset at open-holes under tensile and in-plane bending loading. *International Journal of Solids and Structures*, 113:10–23, 2017.

P. L. Rosendahl, M. Drass, J. Felger, J. Schneider, and W. Becker. Equivalent strain failure criterion for multiaxially loaded incompressible hyperelastic elastomers. *International Journal of Solids and Structures*, 166:32–46, 2019a.

P. L. Rosendahl, V. A. Kolupaev, and H. Altenbach. Extreme yield figures for universal strength criteria. In *State of the Art and Future Trends in Material Modeling*, pages 259–324. Springer, 2019b.

P. L. Rosendahl, Y. Staudt, C. Odenbreit, J. Schneider, and W. Becker. Measuring mode I fracture properties of thick-layered structural silicone sealants. *International Journal of Adhesion and Adhesives*, 91:64–71, 2019c.

P. L. Rosendahl, Y. Staudt, A. Schneider, J. Schneider, and W. Becker. Nonlinear elastic finite fracture mechanics: Modeling mixed-mode crack nucleation in structural glazing silicone sealants. *Materials & Design*, 182:108057, 2019d.

M. H. Sadd. *Elasticity: theory, applications, and numerics*. Burlington - Oxford: Academic Press, 2009.

A. Sapora, P. Cornetti, and A. Carpinteri. A finite fracture mechanics approach to V-notched elements subjected to mixed-mode loading. *Engineering Fracture Mechanics*, 97:216–226, 2013.

C. Sator. *Asymptotische Nahfeldanalysen ebener Multi-Materialverbindungsstellen mit der Methode komplexer Potentiale*, volume 21. Technische Universität Darmstadt, Studienbereich Mechanik, 2010.

G. Savin. *Stress concentration around holes*, volume 1. Pergamon Press, 1961.

A. Seweryn. Brittle fracture criterion for structures with sharp notches. *Engineering Fracture Mechanics*, 47(5):673–681, 1994.

A. Seweryn, S. Poskrobko, and Z. Mróz. Brittle fracture in plane elements with sharp notches under mixed-mode loading. *Journal of Engineering Mechanics*, 123(6): 535–543, 1997.

G. C. Sih. *Methods of analysis and solutions of crack problems*, volume 1. Springer Science & Business Media, 1973.

G. Sinclair. Stress singularities in classical elasticity—I: Removal, interpretation, and analysis. *Applied Mechanics Reviews*, 57(4):251–298, 2004a.

G. Sinclair. Stress singularities in classical elasticity—II: Asymptotic identification. *Applied Mechanics Reviews*, 57(5):385–439, 2004b.

G. Sinclair and D. Mullan. A simple yet accurate finite element procedure for computing stress intensity factors. *International Journal for Numerical Methods in Engineering*, 18(11):1587–1600, 1982.

C. Song and J. P. Wolf. Semi-analytical representation of stress singularities as occurring in cracks in anisotropic multi-materials with the scaled boundary finite-element method. *Computers & Structures*, 80(2):183–197, 2002.

B. Sørensen. Materials and structures for wind turbine rotor blades—an overview. In *Proceedings of the 17th International Conference on Composite Materials, Edinburgh, UK*, pages 27–31, 2009.

H. Sosa. Plane problems in piezoelectric media with defects. *International Journal of Solids and Structures*, 28(4):491–505, 1991.

C. Soutis and N. Fleck. Static compression failure of carbon fibre T800/924C composite plate with a single hole. *Journal of Composite Materials*, 24(5):536–558, 1990.

N. Stein, P. Weißgraeber, and W. Becker. A model for brittle failure in adhesive lap joints of arbitrary joint configuration. *Composite Structures*, 133:707–718, 2015.

N. Stein, S. Dölling, K. Chalkiadaki, W. Becker, and P. Weißgraeber. Enhanced xfem for crack deflection in multi-material joints. *International Journal of Fracture*, 207 (2):193–210, 2017.

M. Stern, E. Becker, and R. Dunham. A contour integral computation of mixed-mode stress intensity factors. *International Journal of Fracture*, 12(3):359–368, 1976.

A. Stroh. Dislocations and cracks in anisotropic elasticity. *Philosophical magazine*, 3 (30):625–646, 1958.

Z. Suo. Singularities, interfaces and cracks in dissimilar anisotropic media. *Proceedings of the Royal Society of London. A. Mathematical and Physical Sciences*, 427(1873): 331–358, 1990.

H. Tada, P. C. Paris, and G. R. Irwin. *The stress analysis of cracks handbook*, volume 3. New York: ASME Press, 2000.

S. C. Tan. Laminated composites containing an elliptical opening. II. Experiment and model modification. *Journal of Composite Materials*, 21(10):949–968, 1987.

S. C. Tan. Effective stress fracture models for unnotched and notched multidirectional laminates. *Journal of Composite Materials*, 22(4):322–340, 1988a.

S. C. Tan. Finite-width correction factors for anisotropic plate containing a central opening. *Journal of Composite Materials*, 22(11):1080–1097, 1988b.

S. C. Tan. *Stress concentrations in laminated composites*. CRC Press, 1994.

E. Tanné, T. Li, B. Bourdin, J.-J. Marigo, and C. Maurini. Crack nucleation in variational phase-field models of brittle fracture. *Journal of the Mechanics and Physics of Solids*, 110:80–99, 2018.

D. Taylor. *The theory of critical distances: A new perspective in fracture mechanics*. Elsevier Science, 2007.

P. Theocaris. The order of singularity at a multi-wedge corner of a composite plate. *International Journal of Engineering Science*, 12(2):107–120, 1974.

T. Ting. *Anisotropic elasticity: theory and applications*. Number 45. Oxford University Press on Demand, 1996.

P. Tong, T. Pian, and S. J. Lasry. A hybrid-element approach to crack problems in plane elasticity. *International Journal for Numerical Methods in Engineering*, 7(3): 297–308, 1973.

A. Turon, C. G. Davila, P. P. Camanho, and J. Costa. An engineering solution for mesh size effects in the simulation of delamination using cohesive zone models. *Engineering Fracture Mechanics*, 74(10):1665–1682, 2007.

N. Valoroso and R. Fedele. Characterization of a cohesive-zone model describing damage and de-cohesion at bonded interfaces. Sensitivity analysis and mode-I parameter identification. *International Journal of Solids and Structures*, 47(13):1666–1677, 2010.

N. Valoroso, S. Sessa, M. Lepore, and G. Cricrì. Identification of mode-I cohesive parameters for bonded interfaces based on DCB test. *Engineering Fracture Mechanics*, 104:56–79, 2013.

M. Van Dyke. *Perturbation methods in fluid mechanics*, volume 136. Academic press New York, 1964.

T. Vandellos, E. Martin, and D. Leguillon. Comparison between cohesive zone models and a coupled criterion for prediction of edge debonding. In *16th European Conference on Composite Materials*, 2014.

M. E. Waddoups, J. R. Eisenmann, and B. E. Kaminski. Macroscopic fracture mechanics of advanced composite materials. *Journal of Composite Materials*, 5(4):446–454, 1971.

S. Wang. An analytical singular element for interface V-shaped notches in bi-material Kirchhoff plate bending. *Engineering Fracture Mechanics*, 180:282–295, 2017.

P. Weißgraeber and W. Becker. Predicting effective strengths of bonded lap joints with a finite fracture mechanics criterion. In *Proceedings of the 32nd Risø International Symposium in Materials Science Composite Materials for Structural Performance: Towards Higher Limits. Technical University of Denmark*, pages 479–486, 2011.

P. Weißgraeber and W. Becker. Finite fracture mechanics model for mixed mode fracture in adhesive joints. *International Journal of Solids and Structures*, 50(14–15): 2383–2394, 2013.

P. Weißgraeber, N. Stein, and W. Becker. A general sandwich-type model for adhesive joints with composite adherends. *International Journal of Adhesion and Adhesives*, 55:56–63, 2014.

P. Weißgraeber, J. Felger, D. Geipel, and W. Becker. Cracks at elliptical holes: stress intensity factor and finite fracture mechanics solution. *European Journal of Mechanics-A/Solids*, 55:192–198, 2016a.

P. Weißgraeber, D. Leguillon, and W. Becker. A review of Finite Fracture Mechanics: crack initiation at singular and non-singular stress raisers. *Archive of Applied Mechanics*, 86(1):375–401, 2016b.

J. M. Whitney and R. Nuismer. Stress fracture criteria for laminated composites containing stress concentrations. *Journal of Composite Materials*, 8(3):253–265, 1974.

M. Williams. Stress singularities resulting from various boundary conditions in angular corners of plates in extension. *Journal of Applied Mechanics*, 19(4):526–528, 1952.

M. Williams. The stresses around a fault or crack in dissimilar media. *Bulletin of the Seismological Society of America*, 49(2):199–204, 1959.

C. Williamson, J. Cook, and A. Clarke. Investigation into the failure of open and filled holes in CFRP laminates under biaxial loading conditions. In *Proc. ECCM*, volume 11, 2004.

A. Wormsen, A. Fjeldstad, and G. Härkegård. The application of asymptotic solutions to a semi-elliptical crack at the root of a notch. *Engineering Fracture Mechanics*, 73 (13):1899–1912, 2006.

Z. Yosibash. *Singularities in elliptic boundary value problems and elasticity and their connection with failure initiation*, volume 37. Springer Science & Business Media, 2011.

Z. Yosibash, E. Priel, and D. Leguillon. A failure criterion for brittle elastic materials under mixed-mode loading. *International Journal of Fracture*, 141(1-2):291–312, 2006.

A. Zak and M. L. Williams. Crack point stress singularities at a bi-material interface. *Journal of Applied Mechanics*, 30(1):142–143, 1963.

M. Zappalorto and P. Lazzarin. In-plane and out-of-plane stress field solutions for V-notches with end holes. *International Journal of Fracture*, 168(2):167–180, 2011.

M. Zappalorto, P. Lazzarin, and J. Yates. Elastic stress distributions for hyperbolic and parabolic notches in round shafts under torsion and uniform antiplane shear loadings. *International Journal of Solids and Structures*, 45(18-19):4879–4901, 2008.

J. Zhang, Y. Dong, C. Ju, and W. Lin. A new singular element for evaluating stress intensity factors of V-shaped notches under mixed-mode load. *Engineering Analysis with Boundary Elements*, 93:161–166, 2018.

H. Ziegler. *An introduction to thermomechanics*, volume 2. North Holland, 1983.

In total 197 references.